

| | |
|-------------|--|
| Title | Study on Edge Fluctuation of Supersonic Molecular-Beam Fueled Plasmas Using Langmuir probes and Fast Cameras in Heliotron J(Dissertation_全文) |
| Author(s) | Zang, Linge |
| Citation | Kyoto University (京都大学) |
| Issue Date | 2014-03-24 |
| URL | http://dx.doi.org/10.14989/doctor.k18385 |
| Right | |
| Type | Thesis or Dissertation |
| Textversion | ETD |

**Study on Edge Fluctuation of
Supersonic Molecular-Beam Fueled Plasmas
Using Langmuir probes and Fast Cameras
in Heliotron J**

ZANG Linge

Abstract

Improvement of energy confinement is always the first task for a fusion device. Using the novel fueling technique - supersonic molecular-beam injection (SMBI), the confinement has been significantly improved in a heliotron fusion device – Heliotron J. One motivation of this study is to experimentally investigate the effect of SMBI to edge fluctuation, to understand the improved confinement from the view angle of plasma edge turbulence. In addition, it is important to develop the advanced diagnostic hardware and analysis techniques for further study of edge turbulence. Two diagnostics tools are adopted for the edge turbulence study, the conventional Langmuir probe and the newly developed high-speed video camera (fast camera).

A perpendicular-view fast video camera has been installed in Heliotron J to observe the behavior of filamentary structures of edge plasma turbulence across the last closed flux surface (LCFS). SMBI can greatly increase the edge H_α emission; hence, we used the high imaging rate and shutter speed of the camera to capture the behavior of the fast propagating filamentary structures. A high-pass fast Fourier transform filter on the time dimension was adopted to extract the fluctuation component from the raw data for each pixel. The motion of the filamentary structures was clearly visible when we applied an amplitude threshold to identify the intense structures. In addition, a time-resolved 2D cross-correlation technique was adopted to estimate the poloidal phase velocity of turbulence. The motion direction was found to be reversed dramatically just after an SMBI pulse.

The fluctuation and fluctuation induced particle transport near the last closed flux surface (LCFS) in Heliotron J is studied in a supersonic molecular-beam injection (SMBI) fuelled NBI plasma. A Langmuir probe array is installed to measure the fluctuations of both ion saturation current (I_s) and poloidal electric field (E_θ). Two different fluctuation characteristics are observed after SMBI. First, just after SMBI for a short period, I_s fluctuation level is increased in the low frequency range, and the fluctuation state changed from a coherent-mode-dominated and nearly Gaussian to an intermittent and non-Gaussian one. The sharp increase of fluctuation induced particle flux is considered to be one of the reasons of degradation of plasma stored energy (W_p). Second, the fluctuation induced particle transport was reduced long after SMBI, suggesting better particle confinement in W_p climbing phase. We expect the short effect period of gas injection to the edge fluctuation might be an advantage of this novel fueling technique.

A new way has been developed to measure the radial structure of edge turbulence in Heliotron J, with the combination of a Langmuir probe array and a vertical viewed fast camera. High cross-correlation was found between the fluctuation components of the camera pixel signal nearby the probe tips and the ion saturation current, demonstrating the fluctuation information from the intensity of plasma-surface interaction mainly reflects the local density fluctuation. According to the interaction intensity between probe and plasma, the radial span

of the 20-30 kHz mode has been identified to be inside of $\Delta\rho=20\text{mm}$ ($\Delta\rho=\rho-a$). From the band-passed camera images, large-sized (14.4cm) poloidal structure was found. The results suggest the combination of camera and probe is a powerful tool for edge fluctuation diagnostic.

Two conclusions are reached in this study. First, SMBI have modified the edge fluctuation characteristics to benefit the plasma confinement, although this also might be only the reflection of better confinement in the core. Second, the Langmuir probe and the fast camera show their different advantages in edge turbulence diagnostics, while their combination makes a more powerful tool for further research.

Contents

| | |
|--|----|
| Chapter 1. Introduction | 3 |
| 1.1 Fusion..... | 3 |
| 1.1.1 Demand of Energy and call for Controlled Fusion | 3 |
| 1.1.2 Research of Magnetic Confined Fusion Plasma..... | 4 |
| 1.2 Edge Plasma and turbulence | 5 |
| 1.2.1 Edge Plasma..... | 5 |
| 1.2.2 Edge plasma turbulence | 7 |
| 1.3 SMBI..... | 8 |
| 1.4 Motivations | 9 |
| 1.5 Outline..... | 9 |
| Chapter 2. Measurements of plasma edge turbulence..... | 16 |
| 2.1 History of plasma edge turbulence measurements | 16 |
| 2.2 Diagnostic Equipments | 17 |
| 2.2.1 Langmuir Probe..... | 17 |
| 2.2.2 High-speed Video Camera (fast camera)..... | 17 |
| 2.3 Data processing techniques | 19 |
| 2.3.1 Fluctuation induced particle flux Γ | 19 |
| 2.3.2 Wavenumber-frequency spectra $S(k,\omega)$ | 20 |
| 2.3.3 Bicoherence..... | 23 |
| 2.3.4 Time delay estimation (TDE)..... | 23 |
| 2.3.5 Video data processing..... | 23 |
| Chapter 3. Heliotron J..... | 34 |
| 3.1 Introduction..... | 34 |
| 3.2 Characteristics of Magnetic Field Configurations of Heliotron J | 34 |
| 3.2.1 Helical-axis Heliotron Configuration..... | 34 |
| 3.2.2 Edge Magnetic Field | 35 |
| 3.3 Heating Devices | 36 |
| 3.4 Fueling Devices..... | 37 |
| 3.5 Diagnostics..... | 37 |
| 3.5.1 Edge turbulence diagnostics..... | 37 |
| 3.5.2 Other diagnostics..... | 38 |
| Chapter 4. Effect of SMBI on edge fluctuation and particle transport in Heliotron J..... | 48 |
| 4.1 Introduction..... | 48 |
| 4.2 Experimental set-up | 49 |
| 4.3 Analysis Approach | 49 |
| 4.4 Experiment result and analysis..... | 50 |
| 4.5 Discussion | 52 |
| 4.6 Summary | 52 |
| Chapter 5. Observation of edge filamentary structure motion during supersonic molecular-beam injection using a fast camera in Heliotron J..... | 64 |

| | |
|--|-----|
| 5.1 Introduction..... | 64 |
| 5.2 Equipment Setup..... | 65 |
| 5.3 Data Analysis and Results..... | 66 |
| 5.3.1 Extraction of filamentary structures..... | 66 |
| 5.3.2 Poloidal velocity estimation..... | 67 |
| 5.4 Discussion..... | 68 |
| 5.5 Summary..... | 68 |
| Chapter 6. Investigation of the edge fluctuation structures with the combination of a camera and a Langmuir probe cluster in Heliotron J..... | 78 |
| 6.1 Introduction..... | 78 |
| 6.2 Experimental set-up..... | 79 |
| 6.3 Result analysis and discussion..... | 80 |
| 6.3.1 Dynamics of the fluctuation structures in camera image..... | 80 |
| 6.3.2 Identification of the radial span of the turbulence structure in camera image..... | 80 |
| 6.4 Summary..... | 81 |
| Appendix. Plasma-surface interaction effect on camera image..... | 81 |
| Chapter 7. Summary..... | 98 |
| Acknowledgements..... | 99 |
| Lists of Publications and Presentations..... | 101 |

Chapter 1. Introduction

1.1 Fusion

1.1.1 Demand of Energy and call for Controlled Fusion

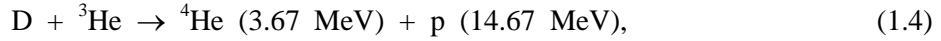
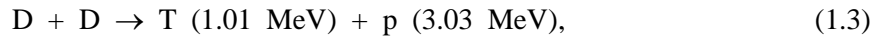
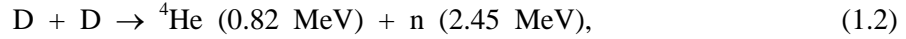
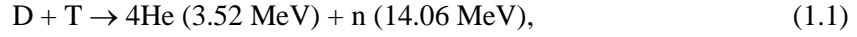
We human beings need a lot of electricity for our living and industry. The electricity demand has rapidly risen during dozens of decades. Figure 1.1 shows the amount of electricity consumption from 1975 to 2008 in the world. During two decades, it has increased 1-6 % for every year in the world [1]. In the present days, the sustainable, dependable and safe source for the supplement of base-load electricity is one of important issues in the world. Figure 1.2 shows the electricity production by sources. We depend on the fossil fuels, such as oil, coal and Liquid Natural Gas (LNG), to generate the electricity with accounting for the total electricity production of approximately 70 %. However, the fossil fuels have two major disadvantages: one is the depletion of reserves and the other is the emission of Green House Gas (GHG), which is represented by carbon dioxide (CO₂). Figure 1.3 shows the life cycle CO₂ emission by electricity production technologies. Amounts of CO₂ emission for power plants using fossil fuels are 10-90 times larger than those for nuclear power plant and renewable energy sources, such as wind, solar cell and geothermal power plant. For these reasons, the fossil fuels have to be replaced by another energy resources.

Several countries have supported the development of nuclear power plants. Strictly speaking, the nuclear reaction involves both fission and fusion; usually the nuclear energy indicates the fission energy, however, we should distinguish the fission energy from the fusion energy. Those countries have a high percentage of electricity production from the fission energy: France (75%), Belgium (54%), Ukraine (47%), Sweden (42%), South Korea (36%), and Japan (25%) [3]. The fission energy is the sustainable and dependable source of base-load electricity that does not emit GHGs during the electricity production (see figure 1.3). However, the fission energy has two well-known disadvantages: danger of accidents and storage of long-lived radioactive wastes. There were two huge accidents at Chernobyl (Ukraine) in 1986 and Fukushima (Japan) in 2011. In the case of Chernobyl, the reactor was destroyed in the accident and ¹³¹I of 1200-1800 PBq (10¹⁵ Bq) and ¹³⁷Cs of 74-86 PBq are released to the environment by the accident [4]. Among residents of Belarus, the Russian Federation and Ukraine, there had been up to the year 2005 more than 6,000 cases of thyroid cancer reported in children and adolescents who were exposed at the time of the accident [4]. In the case of Fukushima, 15 meters tsunami disabled the power supply for cooling systems of Fukushima Daiichi reactors. The hydrogen explosion occurs and the radioactive releases to air. Iodine-131 of 160 PBq and Cesium-137 of 15 PBq are released to the environment by the accident [5]. During the next decades, health hazards due to the radiation can be expected.

CHAPTER 1. Introduction

Many governments have also provided subsidies for the development of renewable energy sources: wind, solar cell and geothermal energies. A lot of renewable energy sources do not emit GHGs during the electricity production and do not have critical danger of accidents. However, renewable energy sources have disadvantages about the dependable electricity production, because they depend on the climates.

It is necessary to develop the sustainable, dependable and safe source of base-load electricity, which does not emit GHGs during the electricity production. The fusion energy will be one of answers. The fusion reaction is that light ions combine to form heavier ions. In that time, large energy, which corresponds to $E = \Delta mc^2$, is released. Realizable fusion reactions for fusion reactors are following as:



where D, T, He, n and p denote the deuterium, the tritium, the helium, the neutron and the proton, respectively. The main fuels for the fusion energy are D and T. The deuterium exists naturally in heavy water; there is one part of D_2O for every 6,400 parts of H_2O . The deuterium is easy to separate it out. However, the tritium does not exist naturally. It is also radioactive and its decay time is 12.3 years. It has to be bred from ${}^6\text{Li}$ or ${}^7\text{Li}$ in a fusion reactor as follow:



The lithium also exists naturally in water. Therefore, the fuels for the fusion energy are regarded as one of inexhaustible energy sources. The GHGs are not emitted due to the fusion reactions (see equations (1.1)-(1.4)). For the case of D-T reaction, the amount of long-lived radioactive waste is about 1,000 times smaller than that for the fission reactors [6]. The other advanced reactions, such as D-D and D- ${}^3\text{He}$ reactions, have fewer radioactivity or none at all. The fusion energy does not depend on the climate and can be the core energy source. For these reasons, the fusion energy will be a candidate of alternate energies.

1.1.2 Research of Magnetic Confined Fusion Plasma

To achieve the fusion energy, a method of magnetic confinement for plasmas has been developed. It is to confine high temperature and dense plasmas using magnetic field, because charged particles moves along a magnetic field line due to the Lorentz force. The torus magnetic field was invented to create closed magnetic field and it has been to be a dominant concept for the magnetic confinement. However, in a simple torus magnetic field, which has only a toroidal magnetic field, charge particles polarize downwards and upwards of a torus due to $\nabla\mathbf{B}$ drift. This polarization creates a vertical electric field, and then all charge particles are driven out toward the vacuum wall due to $\mathbf{E}\times\mathbf{B}$ drift. Therefore, it is impossible to confine plasma with a simple torus magnetic field. To solve this problem, the magnetic field line

CHAPTER 1. Introduction

should be twisted: the helical structure of magnetic field. There are two concepts of magnetic field to make the helical structure of magnetic field: tokamak and stellarator/heliotron configurations. The difference between two concepts is the way to generate poloidal magnetic field for the helical structure of magnetic field. In a tokamak device, a large current in plasma generates the poloidal magnetic field. On the other hand, in a stellarator/heliotron device, external coils generate the helical structure of magnetic field, and plasma current is not necessary to generate poloidal magnetic field.

Tokamak comes from the Russian words “*toroidalnaya kamera magnitnaya katushka*” that means “toroidal chamber magnetic coils” [6]. In 1968, it is reported that the electron temperature over 1 keV and plasma confinement time, which exceeds Bohm confinement time, are observed in T-3 tokamak [7,8]. From this time, tokamak device became a dominant concept of fusion research. Many tokamak devices have been performed in the world: Japan Torus-60 Upgrade (JT-60U, Japan) [9], Joint European Torus (JET, European Union) [10], Tokamak Fusion Test Reactor (TFTR, the United States) [11], DIII-D (the United States) [12], and ASDEX-U (Germany) [13] and so on. To demonstrate the plasma energy breakeven, International Thermonuclear Experimental Reactor (ITER) [14] project was started with seven member entities (European Union, Japan, the United States, Korea, Russia, China and India) and it is under construction in Cadarache, France.

A stellarator/heliotron device is one of earliest devices for the fusion research. The first stellarator device is invented by Lyman Spitzer in 1950 and its name is figure-8. Stellarator/heliotron devices are less subject to effects such as disruptions, which is connected with the large plasma current. Furthermore, stellarator/heliotron devices are more suitable for steady state and continuous operation. The fusion research with stellarator/heliotron device has been carried out in Heliotron E [15], Compact Helical System (CHS) [16], Large Helical Device (LHD, Japan) [17] and Wendelstein7-AS (W7-AS, Germany) [18]. In stellarator/heliotron plasmas, the increase of neoclassical (NC) transport due to the ripple transport in the $1/\nu$ regime, usually we call the NC ripple transport, is a critical issue, thus to reduce this transport is one of important issues in stellarator/heliotron devices. In Heliotron E, it is confirmed that the energy confinement time is improved by 30 % with the inward shift of the magnetic axis in electron cyclotron heating (ECH) or neutral beam injection (NBI) heating plasma [19]. However, since Heliotron E has a wide magnetic hill region, the MagnetoHydroDynamic (MHD) instability was observed with the increase of beta value. To enhance MHD stability by a magnetic well region in high beta plasma, the experiment with the outward shift of the magnetic axis was carried out. In that experiment, however, the bad particle transport was observed [19]. A wide magnetic well region for the stellarator/heliotron plasmas is necessary to obtain MHD stability with good particle transport. Heliotron J tries to solve this difficulty by the introduction of a helical-axis heliotron configuration [20,21].

1.2 Edge Plasma and turbulence

1.2.1 Edge Plasma

- **Diverted plasmas**

A magnetic confined fusion torus device usually consists of purely a toroidal and poloidal magnetic field. In order to prevent the plasma from hitting the walls of the vessel, the

CHAPTER 1. Introduction

magnetic field is shaped using poloidal field (PF) coils to produce a region of closed flux surfaces (plasma core) surrounded by field lines which intersect targets designed to withstand the large heat loads. This is called a divertor since the plasma leaving the core is diverted away from the walls which could otherwise be damaged by high heat loads.

The magnetic geometry of a divertor configuration is illustrated in **Figure 1.4**, which shows a slice through a tokamak at a fixed toroidal angle. The toroidal field is directed into the board (indicated in green). A current runs through the plasma core as indicated in red, producing the poloidal field shown as a black loop. A second current is then run through a coil (lower red) in the same direction as the plasma current. The sum of these two poloidal fields produces the X structure shown. The x-point itself (indicated) is a line along which the poloidal field due to the currents in the plasma and the coil cancel and the field is purely toroidal. Intersecting with the x-point is a surface called the “separatrix” (blue arrows) which separates the closed field-lines of the plasma core from open field-lines which intersect divertor target plates. The surface just inside the core is known as the last closed flux-surface (LCFS) and will sometimes be referred to as the plasma edge. The region of open field-lines surrounding the core outside the separatrix is known as the scrape-off-layer (SOL), whilst the area below the separatrix between the divertor plates is called the private-flux region. In a Stellarator /Heliotron device, since the plasma current is small, the divertor configuration is basically formed by the current in external coil.

- **The scrape-off layer**

The scrape-off layer (SOL) region of open field-lines shown in **Figure 1.4** outside the separatrix is a boundary between the hot plasma core and the material surfaces of the vacuum vessel [22]. The properties of this region determine how and where the particles and energy lost from the plasma are deposited and hence impacts on the operating lifetime of vessel components. Conversely, properties of the SOL also determine how impurities released from the vessel by evaporation, sputtering or other effects are transported into the plasma core. The dynamics of this region depend on processes at the edge of the plasma, the interaction of hot plasma with neutral gas, impurities and the interaction of plasma with material surfaces such as divertor targets.

As shown in **Fig. 1.5**, the simplest view of the SOL is as a quiescent, steady state structure in which plasma diffuses across field lines outwards from the core, this flux being balanced by flows of plasma along field-lines to the divertors at the ion sound speed c_s . These flows are shown in a one dimensional model in **Fig. 1.6**. The diffusion for both particles and energy across the field is generally unstable. In steady state, supposing there are no other sources or sinks (such as ionization) in the SOL, the loss along the perpendicular field is balanced by the horizontal flow across the field. We can write,

$$\frac{d}{dr} \left[D_{\perp} \frac{dn}{dr} \right] = \frac{n C_s}{L_C} \quad (1.7)$$

Where D_{\perp} is the cross field diffusion coefficient and L_C is the connection length.

Assuming that C_s and D_{\perp} are independent of radius, Eqn 1.7 is integrated to obtain

$$n(r) = n(a) \exp\{-(r-a) / \lambda_n\} \quad (1.8)$$

CHAPTER 1. Introduction

Where n is the density of SOL, a is the minor radius at LCFS or the Divertor, and

$$\lambda_n = \left[\frac{D_{\perp} L_C}{C_S} \right]^{\frac{1}{2}} \quad (1.9)$$

Eqn 1.9 gives the e-folding lengths in SOL in terms of the cross-field diffusion parameters. In fact, D_{\perp} is deduced by the measured values of λ_n . Measurements of the e-folding length for n_e can be made with probes. Typical values are ~ 10 mm. D_{\perp} is typically $\sim 1 \text{ m}^2 \text{ s}^{-1}$. However, the calculation of diffusion coefficients would be much more complex if either particle or energy sources are present in SOL.

1.2.2 Edge plasma turbulence

In reality however, the SOL has been found to be more complicated than this simple diffusive picture. Plasma in the SOL is subject to instabilities, drifts, currents and interactions with material surfaces. In addition, the magnitude of diffusive processes is found to be too small to account for the observed transport: The observed radial “diffusion” of plasma is predominantly due to turbulent (anomalous) - rather than diffusive - processes.

The studies of edge plasma fluctuation are very complex and although they have been under intense experimental and theoretical studies for about a half a century, they are not well understood yet. The study of turbulence in the edge plasma, which bridges the hot core and material wall, is the beginning of detailed experimental researches of the fundamental properties of fusion plasma turbulence. The main reason why we initially paid attention to edge turbulence was the relatively simple diagnostics.

Initial experimental studies of edge plasmas had already revealed rather large-amplitude turbulence available in the edge region and an intermittent feature of the turbulence. Moreover, the earliest applications of fast cameras for diagnostics of edge plasma identified the existence of coherent filamentary structures. Some time later, such structures were also found with probe and with imaging diagnostics, such as the gas-puff imaging (GPI) systems.

These coherent filamentary structures extended along the magnetic field lines, always called ‘blobs’, were believed to be responsible for a strong intermittency of edge turbulence observed with probes. Further studies demonstrated that blobs are common phenomena in the edge plasmas of both tokamaks and stellarators, supporting earlier conclusions on the similarities of edge turbulence in different toroidal magnetic devices¹. The plasma filaments moving in a vacuum are not confined at edge plasma and quickly spread all the way to the wall. It was realized that the dynamics of plasma filaments generated by ELMs is very similar to blob dynamics.

A first qualitative theory[23, 24] assumes that due to some turbulent processes in the vicinity of LCFS, a filament with high density at the outer side of the torus is peeled off the bulk plasma. Then, plasma polarization (i.e. charge separation) caused by effective gravity drifts (curvature and ∇B drifts) at the outer side of the torus, results in a radial $E \times B$ convection of the plasma blob toward the first wall. The magnitude of the electric field and, therefore, the convection speed are determined from the balance of polarization and parallel

CHAPTER 1. Introduction

currents. From experimental data, we can find that blob can propagate as a coherent structure with a speed of the order of a few hundred meters per second. Since then, the theory of blob dynamics, although still having an effective gravity as a driving mechanism, was significantly extended for additional physics. Also, both 2D and 3D numerical simulations were useful in either analytic results or a better understanding of blob dynamics.

This structure illustrated in **Fig 1.7** is localized in the plane perpendicular to the magnetic field B but is extended parallel to B . The outwards toroidal curvature force induces (1) an $F \times B$ particle drift, (2) a vertical charge polarization, (3) a vertical electric field and (4) an outwards $E \times B$ drift. Any species-summed force leads to the same effects, so this is a universal transport mechanism at the edge of confined plasma. The blobs can originate from the nonlinear evolution of either turbulence or macroscopic MHD instabilities.

Turbulence related structures - intermittent events such as blobs, blob-like structures or filaments, are significant sources for cross-field transport in SOL region of fusion devices. The convective transport in the SOL can increase particle recycling, and make divertor efficiency be reduced, and as the result lead to high level erosion of first walls [25, 26]. Theoretically, it has been predicted that blobs move towards first walls on lower field side due to $E \times B$ drift, where charge separation in the blobs is driven by gradient and curvature of the magnetic field [27-30]. This prediction has been identified by two experimental observations in TORPEX [31, 32] and TJ-K [33] devices. Radial profile of statistical characteristics of blobs has been investigated by multi-pin Langmuir probes in DIII-D [34], Alcator C-Mod [35], T-10 [36], TEXTOR [37] and CASTOR [38], those data universally show pronounced non-Gaussian features in time-series probability distribution functions (PDFs) and radial blob propagation velocities of about 1 km/s. The TCV result shows good agreement between the blob characteristics measured using reciprocating probes and simulation results of 2D interchange turbulence [39]. A comparison between turbulent statistical characteristics in low and high field sides was carried out in JT-60U [40], it is found that positive bursty events associated with blob-related plasma transport appear frequently at the LFS midplane. Further, the PDF at the LFS midplane is strongly positively skewed, while the PDF at the HFS SOL is close to a Gaussian distribution. The National Spherical Torus Experiment (NSTX) reports the statistical and the spectral properties of edge turbulence with gas puff imaging diagnostics [41]. The difference between the L-mode and the high confinement mode (H-mode) is studied. Only in the L-mode the energy flows toward the small wavenumber feeding the bigger blobs.

Detail of the diagnostic tools and the data analysis techniques will be described in CH.2.

1.3 SMBI

Fueling and recycling control is one of the key issues to obtain high density and high performance plasma in magnetic confinement devices from two aspects: (1) profile control of the plasma density and (2) reduction of neutrals in the peripheral region.

Core fueling by ice pellets is well known as a technique to realize favorable fueling from these aspects. The pellet system is, however, complicated and it is not easy to make pellets small enough for density control in medium or small size devices. A supersonic molecular-beam injection (SMBI) technique, which has been developed by L. Yao [42], on the other hand, is considered to be an effective fueling method for deeper penetration of neutral particles into the core plasma compared to conventional gas-puffing (GP). SMBI is

CHAPTER 1. Introduction

applied not only for core density control but also as an effective edge modification technique in fusion devices [43–45].

A fueling method with SMBI technique has been successfully applied to Heliotron J plasma [46]. It is considered that local fueling with a short pulse intense molecular beam can increase the core plasma density, while avoiding confinement degradation due to the edge cooling caused by excess neutrals in the peripheral region, which is often observed in the case of conventional GP control. SMBI has successfully extended the operation region of line-averaged electron density (\bar{n}_e) versus plasma stored energy (W_p).[47-49]

1.4 Motivations

Motivation of this research include two aspects:

- (i) Improvement of energy confinement is always the first task for a fusion device. As mentioned above, SMBI have significantly improved the confinement in a heliotron fusion device – Heliotron J. The purpose of this study is to experimentally investigate the effect of SMBI to edge fluctuation, to understand the improved confinement from the view angle of plasma edge turbulence.
- (ii) It is important to develop the advanced diagnostic hardware and analysis techniques for further study of edge turbulence.

1.5 Outline

The thesis is structured as follows:

- Chapter 2 describes the basic diagnostic equipments and analysis techniques for edge turbulence experimental study.
- Chapter 3 is devoted to a helical-axis heliotron device Heliotron J.
- Chapter 4 discusses the SMBI effects on the edge fluctuation induced particle transport, and its relation to energy confinement. The data is from Langmuir probe array.
- Chapter 5 introduces the fast camera diagnostics and data processing approach in Heliotron J. A preliminary observation of edge turbulence dynamics during SMBI is discussed.
- Chapter 6 describes a new way to measure the radial structure of edge turbulence, with the combination of a Langmuir probe array and a vertical viewed fast camera. Results during a SMBI fuelled discharge are discussed.

References

- [1] Energy report in 2010, *Agency for Natural Resources and Energy* (in Japanese)
“<http://www.enecho.meti.go.jp/topics/hakusho/2011/index.htm>”.
- [2] E. Imamura and K. Nagano, Reports of Socio-economic Research Center, Y09027
(in Japanese, 2010) “<http://criepi.denken.or.jp/jp/kenkikaku/report/detail/Y09027.html>”.
- [3] Country Nuclear Power Profiles, *International Atomic Energy Agency*,
“http://www-pub.iaea.org/MTCD/Publications/PDF/CNPP2011_CD/pages/countryprofiles.htm”.
- [4] Accident Report of Nuclear Power Plant in Chernobly, *United Nations Scientific Committee on the Effects of Atomic Radiation*,
“<http://www.unscear.org/unscear/en/chernobyl.html>”.
- [5] Accident Report of Nuclear Power Plant in Fukushima, *Ministry of Economy, Trade and Industry*, “<http://www.meti.go.jp/earthquake/nuclear/backdrop/20110911.html>”.
- [6] Francis F. Chen, *An Indispensable Truth* (published in Springer, 2011).
- [7] L.A. Artsimovich *et al.*, *Proceedings of Plasma Physics and Controlled Nuclear Fusion Research*, **1** (1968) 17.
- [8] N.J Peacock *et al.*, *Nature*, **224** (1969) 488.
- [9] M. Yoshikawa, *Nuclear Fusion*, **25** (1985) 1081.
- [10] P.H. Rebut *et al.*, *Nuclear Fusion*, **25** (1985) 1011.
- [11] D.J. Grove and D.M. Meade, *Nuclear Fusion*, **25** (1985) 1167.
- [12] J.L. Luxon, *Nuclear Fusion*, **42** (2002) 614.
- [13] G. Grieger *et al*, *Nuclear Fusion*, **25** (1985) 1231.
- [14] R. Aymar, *IEEE Transaction of Plasma Science*, **25** (1997) 1187.
- [15] K. Uo *et al.*, *Proceedings of the workshop, Varenna*, (1977) 369.
- [16] K. Nishimura *et al.*, *Fusion Technology*, **17** (1990) 86.
- [17] A. Iiyoshi *et al.*, *Fusion Technology*, **17** (1990) 169.
- [18] J. Sapper and H. Renner, *Fusion Technology*, **17** (1990) 62.
- [19] M. Wakatani and S. Sudo, *Plasma Physics and Controlled Fusion*, **38** (1996) 937.
- [20] M. Wakatani *et al.*, *Nuclear Fusion*, **40** (2000) 569.
- [21] M. Yokoyama *et al.*, *Nuclear Fusion*, **40** (2000) 261.
- [22] P C Stangeby. The Plasma Boundary of Magnetic Fusion Devices. IoP, 2000.
- [23] Krasheninnikov, S. I. 2001 *Phys. Lett. A* **283**, 368.
- [24] D’Ippolito, D. A., Myra, J. R. and Krasheninnikov, S. I. 2002 *Phys. Plasmas* **9**, 222.
- [25] Antar G Y *et al* 2001 *Phys. Rev. Lett.* **87** 065001.
- [26] Labombard B *et al* 2000 *Nucl. Fusion* **40** 2041.
- [27] D’Ippolito D A *et al* 2002 *Phys. Plasmas* **9** 222.
- [28] Krasheninnikov S I *et al* 2001 *Phys. Lett. A* **283** 368.
- [29] Aydemir A Y 2005 *Phys. Plasmas* **12** 062503.
- [30] Garcia O E *et al* 2004 *Phys. Rev. Lett.* **92** 165003.
- [31] Furno I *et al* 2008 *Phys. Rev. Lett.* **100** 055004.
- [32] Muller S H *et al* 2009 *Plasma Phys. Control. Fusion* **51** 055020.
- [33] Happel T *et al* 2009 *Phys. Rev. Lett.* **102** 255001.
- [34] Boedo J A *et al* 2003 *Phys. Plasmas* **10** 1670.

CHAPTER 1. Introduction

- [35] Carreras B A *et al* 2001 *Phys. Plasmas* **8** 3702.
- [36] Kirnev G S *et al* 2004 *Plasma Phys. Control. Fusion* **46** 621.
- [37] Xu Y *et al* 2005 *Plasma Phys. Control. Fusion* **47** 1841.
- [38] Devynck P *et al* 2006 *Phys. Plasmas* **13** 102505.
- [39] Garcia O E *et al* 2006 *Plasma Phys. Control. Fusion* **48** L1.
- [40] Tanaka H *et al* 2009 *Nucl. Fusion* **49** 065017.
- [41] Agostini M *et al* 2007 *Phys. Plasmas* **14** 102305.
- [42] L. Yao, in: *New Developments in Nuclear Fusion Research*, Nova Sci. Publ., 2006, pp. 61–87.
- [43] G. Giruzzi *et al.*, *Nucl. Fusion* 49 (2009) 104010.
- [44] H. Takenaga *et al.*, *Nucl. Fusion* 49 (2009) 075012.
- [45] A. Murakami *et al.*, *Plasma Fusion Res.* 6 (2011) 1402135.
- [46] T. Mizuuchi *et al.*, *J. Nucl. Mater.* 415 (2011) S443–S446.
- [47] T. Mizuuchi *et al.*, *Contrib. Plasma Phys.* **50**, 639 (2010)
- [48] T. Mizuuchi *et al.*, *Journal of Nuclear Materials*, **415**, S443-S446 (2011).
- [49] K. Mukai *et al.*, *Plasma and Fusion Research*, **6**, 1402111 (2011).

CHAPTER 1. Introduction

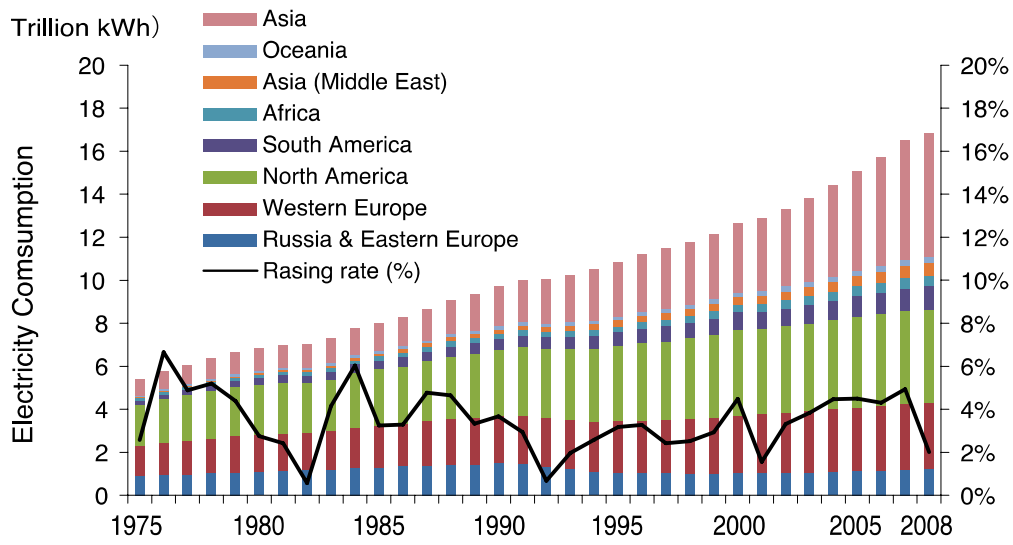


Figure 1.1 Amount of electricity consumption from 1975 to 2008 in the world [1].

Electricity Production (20.2 Trillion kWh, 2008)

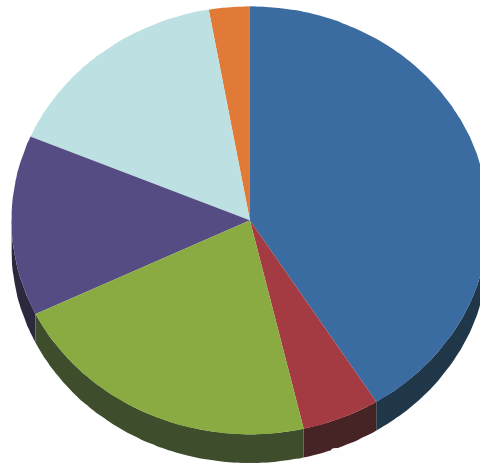


Figure 1.2 Electricity productions by sources [1].

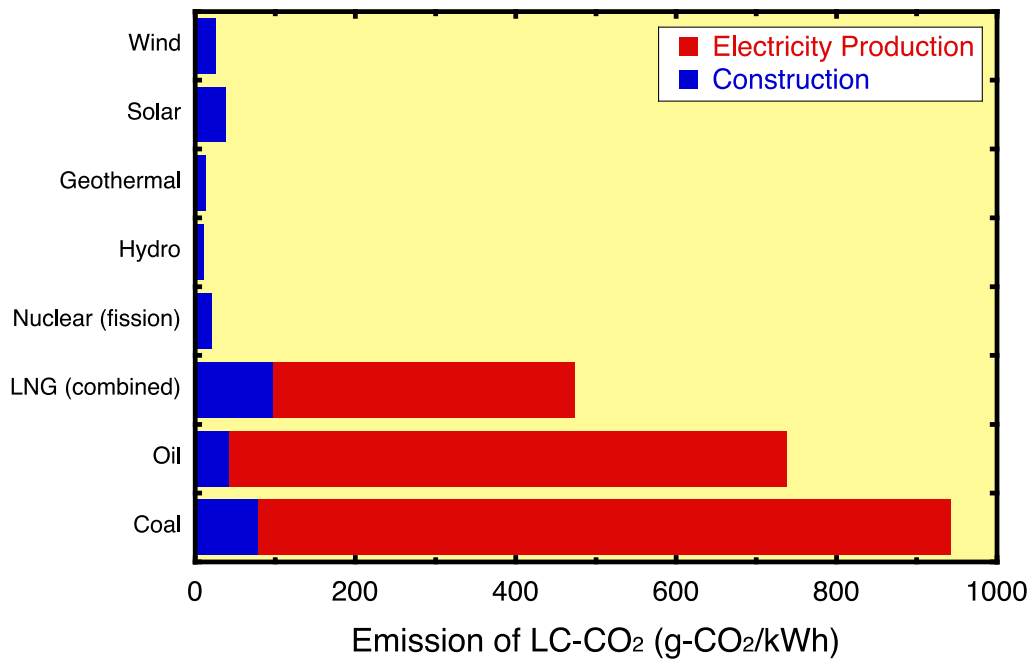


Figure 1.3 Life cycle CO₂ emissions by electricity production technologies [2].

| Concept | Device |
|-------------------------------------|-------------------|
| Quasi-helical | HSX |
| Quasi-torodial | NCSX |
| Quasi-poloidal | QPS |
| Quasi-ominigenous/Quasi-isodyanamic | W7-X, Heliotron J |

Table 1.1 Concepts of advanced stellarator/heliotron devices.

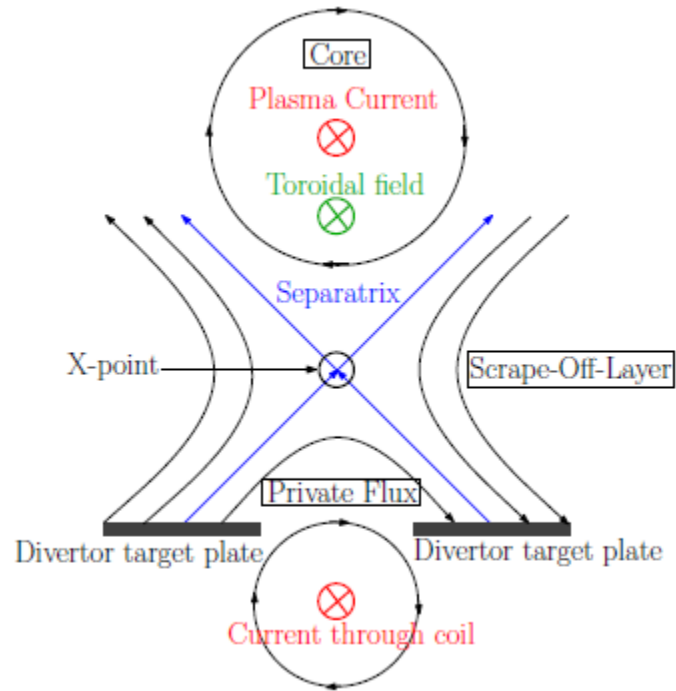


Figure 1.4 X-point and divertor configuration showing toroidal magnetic field (green), currents (red), poloidal magnetic field (black) and separatrix (blue).

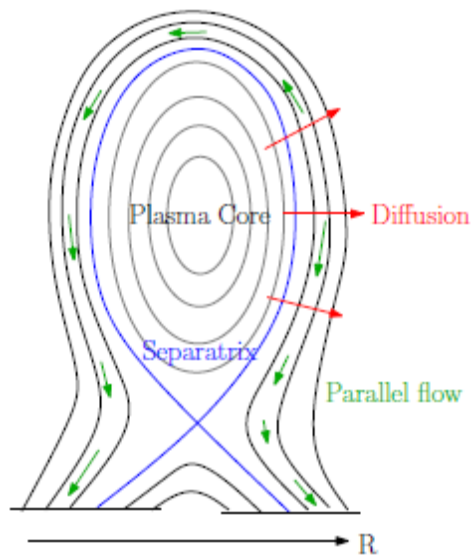


Figure 1.5: Schematic of plasma flows in the SOL. Cross-field diffusion shown as red arrows, parallel flows as green arrows

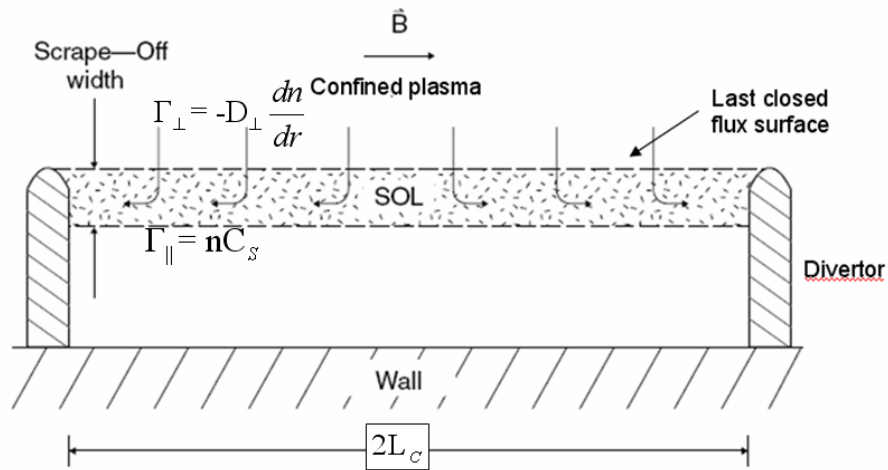


Figure 1.6 Particles and energy flow from the confined plasma into the SOL by cross-field diffusion, followed by parallel to B along the SOL.

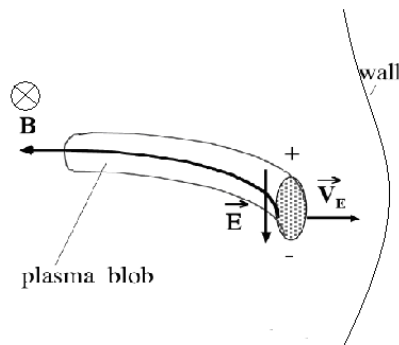


Figure 1.7 Sketch of a plasma 'blob' (2D) or 'filament' (3D)

Chapter 2. Measurements of plasma edge turbulence

To measure the turbulent properties of plasma, special diagnostics tools and data analysis techniques are required. In the first part of this section we introduce the brief history of plasma edge turbulence. The second part describes the diagnostic hardware, with emphasis on Langmuir probe and Gas puff imaging. In the second part, the basic data processing techniques are interpreted.

2.1 History of plasma edge turbulence measurements

One of the earliest studies of magnetized plasma turbulence was done on the ‘calutron’ isotope separation process during the Manhattan Project [1]. In addition to presenting the famous Bohm diffusion formula, Bohm described plasma ‘hash’, or broadband density fluctuations in the frequency range of 1 kHz–1MHz, as observed with Langmuir probes in these arc plasmas ($n \sim 3 \times 10^{13} \text{ cm}^{-3}$, $T_e \sim 5\text{--}10 \text{ eV}$, $B \leq 12 \text{ kG}$). Bohm et al clearly understood the role of turbulent electric fields in cross-field transport, but did not establish a quantitative connection between the turbulence and the transport. Plasma turbulence was measured in many early magnetic fusion devices. According to Nedospasov [2], edge turbulence was measured on the first tokamak TMP at Kurchatov in 1956. Chen [3] noted the apparent universality of the turbulence frequency spectrum and tried to explain the power law fall-off on the basis of drift wave theory. Detailed probe studies of large-scale coherent edge density fluctuations were done on the C-Stellarator at Princeton, including a direct measurement of the fluctuation-induced radial $E \times B$ transport [4]. The 3D structure of both edge density and magnetic field turbulence was measured on the Zeta RFP device at Culham [5], and was described as ‘a system of convective rolls aligned along the magnetic field’. These early measurements are at least qualitatively similar to those in present devices, although they were made using analog techniques. Digital signal processing for turbulence and $E \times B$ transport analysis was introduced by Powers in the mid-1970s [6].

Since the late-1970s there has been a sustained effort to measure and understand plasma turbulence in edge region of toroidal fusion devices. A lot of advanced diagnostic tools including the hardware and data processing approaches have been developed. The main motivation for turbulence measurement is to clarify the cross-field plasma transport mechanism which affects confinement and plasma–wall interactions. A second motivation is to understand the physics of plasma turbulence, e.g. the origin of the H-mode and so on.

The distinction between core and edge is sometimes unclear, generally, the edge is the region outside $r/a \sim 0.9$ where $T_e \sim 10\text{--}100 \text{ eV}$, including the whole region from the last

CHAPTER 2. Measurements of Plasma Edge Turbulence

closed flux surface to the first wall, i.e. the ‘SOL’, but not including (for the purposes of this chapter) the H-mode pedestal, which can reach $T_e \leq 1$ keV.

2.2 Diagnostic Equipments

2.2.1 Langmuir Probe

The most widely used method for diagnosing edge plasmas (and relatively cool industrial plasmas) is the Langmuir probe (LP). This is a set of electrodes inserted into the plasma and whose I-V characteristics are used to measure electron temperature and density. In a high temperature device they can only be used at the very edge of the plasma because the high power loadings in the core damage the probes and release impurities into the plasma which can lead to a disruption. The operation of Langmuir probes is based on the theory of plasma sheaths, describing the interaction of a plasma with a material surface [7, 8]. LPs could measure plasma parameters such as density, electron temperature, and plasma potential and have been used extensively in the study of turbulence and fluctuation-induced transport [9-11].

Some commonly used quantities and their equations are list as follows:

Ion saturation current

$$I_s = \exp(-1/2) \times en_e c_s A^{(+)} \quad (2.1)$$

Here n_e is the electron density, $c_s = \sqrt{(zT_e + T_i)/M_i}$ is the ion sound speed, and $A^{(+)}$ is the effective area for collecting ion current. At the edge plasma region, usually $T_e \sim T_i$, then we have,

$$I_s \propto n_e \sqrt{T_e} \quad (2.2)$$

For the edge plasma usually we have $\frac{\tilde{T}_e}{T_e} \approx 0.4 \sim 0.6 \frac{\tilde{n}_e}{n_e}$. Here the top “~” mark indicate the

fluctuation component of a quantity. Using mathematics we could deduce that for

$$\frac{\tilde{I}_s}{I_s} \approx \frac{\tilde{n}_e}{n_e} \quad (2.3)$$

the error is no more than 20% [12].

Floating Potential

$$V_f = V_s - 3T_e/e \quad (2.4)$$

Here V_s is the plasma potential. If \tilde{T}_e is small compared to \tilde{V}_s , we could get

$$\tilde{V}_f \sim \tilde{V}_s \quad (2.5)$$

2.2.2 High-speed Video Camera (fast camera)

Langmuir probe measurements are a useful diagnostic for edge plasma physics, but they can

CHAPTER 2. Measurements of Plasma Edge Turbulence

only record a relatively small region of the plasma and there is always the danger that the presence of the probe is disturbing the plasma being measured. Video cameras are entirely non-invasive diagnostics which can collect data from a large region of the plasma at high resolution. Because of the speed at which magnetic confined fusion plasmas evolve, cameras capable of at least several thousand frames per second are needed. A fast camera can provide 2D images of turbulence structures by measuring mainly the $H\alpha/D\alpha$ emission. The intensity S_α of the $H\alpha/D\alpha$ line emission is proportional to the neutral gas density n_0 and also depends on the electron temperature T_e and the electron density n_e [13, 14],

$$S_\alpha = n_0 f_3(n_e, T_e) A_{32} \quad (2.6)$$

where $f_3(n_e, T_e)$ is the ratio of the population density of $n=3$ to the ground state, which is a nonlinear function of n_e and T_e . A_{32} is the radiative decay time rate of the $n=3$ to $n=2$ transition. Here, n is the principal quantum number. With the help of gas injection, S_α is greatly enhanced due to the increase of n_0 , therefore the signal to noise ratio of camera image can be high enough and one could use much higher imaging rate and shutter speed, so called “gas puff imaging (GPI)” technique [15]. The neutral density n_0 provided by the gas puff does not change significantly during the short fluctuation time scale ($\sim 10\mu\text{s}$), hence the fluctuations of S_α are due to the local evolution of plasma or propagating plasmoids whose electrons can excite neutral atoms immediately. From the simulation of DEGAS2 code and experimental result of Alcator C-Mod, in an edge plasmas with $10^{13}\text{cm}^{-3} < n_e < 10^{14}\text{cm}^{-3}$, $D\alpha$ emission mainly located in a region with $10\text{eV} < T_e < 50\text{eV}$ [15]. In this temperature range, both the n_e and T_e perturbation can cause the fluctuation of S_α [14]. The interpretation is somewhat simplified if the electron density and temperature fluctuations are in phase, as expected theoretically and approximately verified using Langmuir probes in DIII-D [16] and TEXT [17]. Although there is still no way to determine whether profile changes during GPI are due to density or temperature changes (or both), turbulence properties such as the coherent structure sizes and velocities are independent of the nonlinearities in the $f_3(n_e, T_e)$ and can be evaluated directly from the GPI data [18].

Imaging diagnostics is ongoing on several tokamaks including TFTR [19], ASDEX-Upgrade [20], Alcator C-Mod [13, 21, 22], DIII-D [23] and NSTX [24-26]. All except for DIII-D have used fast visible cameras, usually combined with a gas puff to image edge turbulence; the system on DIII-D is not a camera, but a 32-chord beam-emission spectrometer.

The GPI diagnostic in NSTX is illustrated in **Fig. 2.1(a)** [15, 27]. It views the edge plasma turbulence in the radial vs poloidal plane near the outer midplane edge of the device (**Fig. 2.1(b)**). A gas manifold is mounted on the outerwall behind the RF limiter shadow and oriented to produce a cloud of gas extending along the local poloidal direction at the plasma edge. Note that the edge magnetic field lines in NSTX and other spherical tori are inclined at $\approx 35\text{--}55^\circ$ with respect to the toroidal direction at the outer midplane. The gas puff that leaves this manifold is viewed from a direction nearly along an edge magnetic field line through a re-entrant port about 70 cm away. This view was chosen since edge turbulence is highly correlated along a magnetic field line in NSTX [24] and other machines [28-31], so that the gas puff can localize the light emission to obtain a cross-section of the turbulence in the radial vs poloidal plane. For these experiments the image of the gas cloud is transferred to a Princeton Scientific Instruments Inc. PSI-4 camera using a lens and mirror inside the

CHAPTER 2. Measurements of Plasma Edge Turbulence

re-entrant port. **Fig. 2.2** shows a single image of the He I (587.6 nm) light emission in NSTX as viewed by the PSI camera with an exposure time of 10 μ s, oriented so that the local radially outward direction is towards the right. The 160 \times 80 pixel PSI camera frame indicated by the white rectangle covers an area \approx 32 cm \times 16 cm in the poloidal vs radial plane. The magnetic separatrix (as calculated by EFIT) is shown by the dashed white line.

Due to the closeness of the vessel wall to the plasma edge in all machines, views are restricted to a small section of the plasma edge. In MAST, a fish-eye lens was installed, allowing views of the entire plasma to be taken (**Fig. 2.3**).

2.3 Data processing techniques

Due to the stochastic nature of the turbulent medium, people's knowledge of turbulence is based on the statistical description. Usually it is difficult to get any conclusion from the raw data of turbulence. Processing using different statistical techniques may lead to interested conclusion. This section will introduce the commonly used data processing techniques. 3.3.1-4 describe the techniques for point data, e. g., LP, or BES. 3.3.5 describes the approach for video data from cameras.

2.3.1 Fluctuation induced particle flux Γ

The time averaged fluctuation induced particle flux Γ is calculated using the follow equation [2.7].

$$\Gamma_{\delta\omega} = \langle \tilde{n}\tilde{v} \rangle_{\delta\omega} = \frac{2}{B} \text{Re}[P_{nE}(\omega)] \quad (2.7)$$

Here, $\delta\omega$ is the small spectral band width, $\text{Re}()$ means the real part of a complex, P_{nE} is the cross-amplitude spectrum between density and electric field. For the Langmuir probe array in Fig. 2(b), we take Is1 as the proxy of n_e , and (Vf5-Vf2)/4mm as the proxy of poloidal electric field E_θ . Eq.(1) is then rewritten to be the following equation.

$$\Gamma_{\delta\omega} \sim \frac{2}{B} \text{Re}[P_{I_s-E_\theta}(\omega)] = \frac{2}{B} |\gamma_{I_s-E_\theta}(\omega)| \cos \alpha_{I_s-E_\theta}(\omega) P_{I_s}(\omega)^{1/2} P_{E_\theta}(\omega)^{1/2} \quad (2.8)$$

Here, $P_{I_s-E_\theta}(\omega)$ is the cross-amplitude spectrum, $|\gamma_{I_s-E_\theta}(\omega)|$ is the coherence spectrum, and $\alpha_{I_s-E_\theta}(\omega)$ is the phase spectrum between Is1 and E_θ ; $P_{I_s}(\omega)$ is the auto-power spectrum of Is1, and $P_{E_\theta}(\omega)$ is the auto-power spectrum of E_θ . The total flux in the interested frequency range is then written to be:

$$\Gamma_{total} \sim \frac{2}{B} \sum_{\omega} |\gamma_{I_s-E_\theta}(\omega)| \cos \alpha_{I_s-E_\theta}(\omega) P_{I_s}(\omega)^{1/2} P_{E_\theta}(\omega)^{1/2} \quad (2.9)$$

CHAPTER 2. Measurements of Plasma Edge Turbulence

In our experiment, $|\gamma_{I_s-E_\theta}(\omega)|$ and $\alpha_{I_s-E_\theta}(\omega)$ nearly stay constant. To understand what roles do I_s and E_θ play respectively, we calculate the I_s fluctuation amplitude and E_θ fluctuation amplitude in the interested frequency range in the following way:

$$\tilde{I}_s = [\sum_{\omega} P_{I_s}(\omega)]^{1/2} \quad (2.10)$$

$$\tilde{E}_\theta = [\sum_{\omega} P_{E_\theta}(\omega)]^{1/2} \quad (2.11)$$

2.3.2 Wavenumber-frequency spectra $S(\mathbf{k},\omega)$

An identification of a dispersion relation, which is often useful for characterizing the space/time nature of a wave or a linear instability, is no longer possible in a turbulent medium since a deterministic relation between frequency and wavenumber does not exist. A useful statistical description of turbulence is provided by the wavenumber-frequency spectrum $S(\mathbf{k},\omega)$, which describes the associated fluctuation power resolved as function of wavenumber and frequency. The $S(\mathbf{k},\omega)$ spectra obtained from scattering experiments show the turbulence in the plasma to have a broad frequency spectrum for fixed poloidal and radial wavenumbers and lead to the conclusion that the turbulence evolves into a strongly non-linear state [33-35].

The concept of local wavenumber-frequency spectra density $S_l(\mathbf{k},\omega)$ and its estimation approach using fixed probe pairs were introduced in ref. [36]. An understandable application example is in ref. [37]. In this section, for simplicity, we will use $S(\mathbf{k},\omega)$ to stand for $S_l(\mathbf{k},\omega)$.

Estimation approach of $S(\mathbf{k},\omega)$

The raw data from two fixed probes is broken into many contiguous intervals, say, many realizations. Let's consider the case of the j th realization. From either of the two probe signals we compute the auto-power spectrum $P^{(j)}(\omega)$, which provides a measure of the power in the frequency interval ω to $\omega+d\omega$. From the phase of the cross-power spectrum $\theta^{(j)}(\omega)$ between the two signals, we determine the local wavenumber,

$$k^{(j)}(\omega) = \theta^{(j)}(\omega) / \Delta x$$

where Δx is the separation between the two probes. Then in the ω - k plane, at the coordinate point $(\omega, k^{(j)})$, the amount of auto-power $P^{(j)}(\omega)$ is recorded.

Because of the stochastic nature of the turbulent medium, examination of the next interval of data from the two probes will yield different estimates of power $P^{(j+1)}(\omega)$ and wavenumber $k^{(j+1)}(\omega)$, for the frequency interval ω to $\omega+d\omega$. This new $P^{(j+1)}(\omega)$ is then recorded at a new coordinate $(\omega, k^{(j+1)})$, in the ω - k plane. This process is carried out for all frequencies and repeated for all data intervals.

The average power (taken over all the realizations) associated with a given (\mathbf{k}, ω) is defined to be the local wavenumber-frequency spectra density $S(\mathbf{k},\omega)$,

$$S(\mathbf{k},\omega) = \langle S^{(j)}(\mathbf{k},\omega) \rangle$$

where averaging is performed over the total m realizations, i.e.

CHAPTER 2. Measurements of Plasma Edge Turbulence

$$\langle \rangle \equiv \frac{1}{m} \sum_{j=1}^m$$

and

$$S^{(j)}(\mathbf{k}, \omega) = P^{(j)}(\omega) I_{\delta \mathbf{k}}(\mathbf{k} - \mathbf{k}^{(j)})$$

$I_{\delta \mathbf{k}}$ is the indicator function for a histogram cell size of $\delta \mathbf{k}$, i.e.

$$I_{\delta \mathbf{k}}(\xi) \equiv \begin{cases} 1, & -\delta \mathbf{k} / 2 \leq \xi < \delta \mathbf{k} / 2 \\ 0, & \text{elsewhere} \end{cases}$$

An example of $S(\mathbf{k}, \omega)$ from ref. [37] was shown in Fig. 2.4. $\tilde{\phi}$ and \tilde{n} stand for the space potential fluctuation and density fluctuation, respectively. k_y is the wavenumber in poloidal direction and k_z is the wavenumber in toroidal direction.

Joint spectrum function

Considering an analogy between the wavenumber-frequency spectrum $S(\mathbf{k}, \omega)$ and a joint probability density function, the joint spectrum function $s(\mathbf{k}, \omega)$ is defined by normalizing $S(\mathbf{k}, \omega)$:

$$s(\mathbf{k}, \omega) = \frac{S(\mathbf{k}, \omega)}{\sum_{\mathbf{k}, \omega} S(\mathbf{k}, \omega)}$$

$s(\mathbf{k}, \omega)$ possesses all of the mathematical properties of a probability function, i.e. $s(\mathbf{k}, \omega) \geq 0$ for all \mathbf{k}, ω and

$$\sum_{\mathbf{k}, \omega} s(\mathbf{k}, \omega) = 1$$

Further, conditional spectra are defined as, the normalized power spectrum of ω for fixed \mathbf{k}

$$s(\omega | \mathbf{k}) = \frac{s(\mathbf{k}, \omega)}{\sum_{\omega} s(\mathbf{k}, \omega)}$$

and the normalized power spectrum of \mathbf{k} for fixed ω

$$s(\mathbf{k} | \omega) = \frac{s(\mathbf{k}, \omega)}{\sum_{\mathbf{k}} s(\mathbf{k}, \omega)}$$

An example of $s(\mathbf{k} | \omega)$ contour from ref. [37] was shown in Fig. 2.5. k_y is the wavenumber in poloidal direction and k_z is the wavenumber in toroidal direction.

Statistical dispersion relation $\bar{k}(\omega)$ and its spectral width $\sigma_k(\omega)$

It is natural to define a statistical dispersion relation $\bar{k}(\omega)$ and its spectral broadening width $\sigma_k(\omega)$ from moments of the conditional spectra:

CHAPTER 2. Measurements of Plasma Edge Turbulence

$$\bar{k}(\omega) = \sum_{\mathbf{k}} \mathbf{k} s(\mathbf{k} | \omega)$$

$$\sigma_{\mathbf{k}}(\omega) = \left[\sum_{\mathbf{k}} \mathbf{k}^2 s(\mathbf{k} | \omega) - \bar{k}^2(\omega) \right]^{1/2}$$

We interpret $\bar{k}(\omega)$ as describing the average dispersive behavior of the fluctuations and $\sigma_{\mathbf{k}}(\omega)$ as describing the broadening as a result of the turbulent nature of the fluctuations.

Analogous quantities may also be represented in terms of wavenumber:

$$\bar{\omega}(\mathbf{k}) = \sum_{\omega} \omega s(\omega | \mathbf{k})$$

$$\sigma_{\omega}(\mathbf{k}) = \left[\sum_{\omega} \omega^2 s(\omega | \mathbf{k}) - \bar{\omega}^2(\mathbf{k}) \right]^{1/2}$$

An example of $\bar{k}(\omega)$ and $\sigma_{\mathbf{k}}(\omega)$ from ref. [37] was shown in Fig. 2.6.

Mean phase velocity

Since a deterministic relation between ω and \mathbf{k} does not exist, it is not possible to uniquely define a phase velocity for a single frequency component. In order to estimate the apparent propagation velocity for the bulk of the turbulence, we have chosen to define a mean phase velocity by weighting ω/\mathbf{k} with the joint spectral density function:

$$\bar{v} = \sum_{\mathbf{k}, \omega} (\omega/\mathbf{k}) s(\mathbf{k}, \omega)$$

Note that \bar{v} defined in this manner emphasizes components with greater fluctuation power. An example of mean phase velocity result based on $s(\mathbf{k}, \omega)$ is shown in Fig. 2.7. The data is from two neighboring ion saturation signals aligned in the poloidal direction. Note that an Alfvén Eigenmode-like MHD activity was detected by the magnetic probe at ~20kHz, so the dispersion relation is also modified by the much higher phase velocity of Alfvén Eigenmode near 20kHz. To avoid this effect, the weights are calculated in the frequency range of (50-200)kHz. In this range, the dispersion is nearly linear.

Fringe Jump

When we determine the local wavenumber,

$$k^{(j)}(\omega) = \theta^{(j)}(\omega) / \Delta x$$

if the phase of the cross-power spectrum $\theta^{(j)}(\omega)$ is over π or less than $-\pi$, fringe jump will happen. As a result $\theta^{(j)}(\omega)$ is displaced by -2π or 2π , respectively.

An example was illustrated in Fig. 2.8. The distance between the two probe is 0.4cm, so when

$$k^{(j)}(\omega) = \theta^{(j)}(\omega) / \Delta x = \pm \pi / 0.4 \text{cm} = \pm 8 \text{rad} \cdot \text{cm}^{-1}$$

fringe jump will happen. In this figure, over 100kHz, wavenumber is over 8 rad·cm⁻¹, and negative wavenumber is observed, which is inconsistent with the trend of dispersion relation

CHAPTER 2. Measurements of Plasma Edge Turbulence

under 100kHz. Thus the negative wavenumber is considered to be caused by fringe jump. To avoid this, the estimation of mean phase velocity only includes the data under 100kHz. Besides, the power weight in the low frequency part is much higher and could determine more parts the mean phase velocity. Fringe jump usually happened in the high frequency part, where the cross-phase is larger. Also, in a low-phase-velocity turbulent flow, fringe jump happened more easily with the same reason. Until now, no efforts have been made to modify the fringe jump.

2.3.3 Bicoherence

Bicoherence spectrum is used to measure the phase coherence between three different frequency components [38]. Assuming M sets of data records of the same length, $x(i)$, $i=1,2,\dots,M$, the fourier transform of data set $x(i)$ at frequency f is $X(i)f$. Then the bispectrum is estimated by:

$$B(f_1, f_2) = \frac{1}{M} \sum_{i=1}^M X_{f_1}^{(i)} X_{f_2}^{(i)} X_f^{(i)}$$

where f_1, f_2 and f are three frequencies, and $f_1 + f_2 = f$. The bicoherence is estimated by:

$$b^2(f_1, f_2) = \frac{B^2(f_1, f_2)}{\frac{1}{M} \sum_{i=1}^M |X_{f_1}^{(i)} X_{f_2}^{(i)}|^2 \frac{1}{M} \sum_{i=1}^M |X_f^{(i)}|^2}$$

$b^2(f_1, f_2)$ is bounded between 0 and 1. When $b^2(f_1, f_2) = 1$, the phases of f_1, f_2 and f are completely coupled. For conveniently describing the phase coupling between a specified frequency with the other frequencies, we define the summed bicoherence by analogy to ref. [39] as:

$$b^2(f) = \frac{1}{S(f)} \sum_{f=f_1+f_2} b^2(f_1, f_2)$$

where the sum is taken over all f_1 and f_2 meeting the summation rule $f_1 + f_2 = f$ and $s(f)$ is the term number in the summation of each f .

2.3.4 Time delay estimation (TDE)

Velocity field was of great interest when scientists were finding the evidence for the existence of geodesic acoustic modes (GAMs). TDE method was then proposed as way of inferring the turbulent velocity at locations near LCFS [40-42].

Recent study has confirms that the results of TDE typically overestimate the velocities of plasma mass flow and are sensitive to the underlying turbulence modes [43].

2.3.5 Video data processing

A video contains a series of consecutive images. A gray scale image data is a two-dimensional (2D) array. So the video data is a three dimensional array, including the 2D spatial dimension and 1D time dimension. The processing could be performed in either the spatial or the time dimension.

CHAPTER 2. Measurements of Plasma Edge Turbulence

- **Spatial processing**

Processing in spatial dimension is the same will common image processing. A recommended guide book is [44]. For plasma edge turbulence image, a median filter are particularly effective in the presence of impulse noise, also called salt-and-pepper noise, because the high ISO noise appears as white and black dots superimposed on an image.

An example of median filter application is in **Fig. 2.9(a)** is the raw image, and **Fig. 2.9(b)** is the image processed with a 3×3 median filter.

- **Temporal processing**

Time dimension processing is based on the time-trace data of a single pixel (**Fig. 2.10**). All the time-domain data processing technique could be applied on the pixel data, including the basic smoothing, filtering, and the ones that described in 2.3.1-4. This processing action is duplicated for all the pixels on the image to get a processed video.

A commonly used approach is to get the fluctuation part of the video by removing slowly-varying background light from the images, leaving only the fast transient features. Usually this could be realized by applying Moving Average (MA) or high-pass filter for all the pixels. A sample result of this is shown in Figure 3.3: The image on the left is the original image which has been amplified and gamma-corrected, the central image is the background light calculated by a pixel-wise minimum over 21 images and the right-hand image is the result of subtracting this background from the original. Filamentary structures can be seen faintly against the bright plasma in the original (left) image, but are much clearer in the processed image. In CH.4, we also apply this method to get the fluctuation video in Heliotron J.

References

- [1] Bohm D *et al* 1949 *The Characteristics of Electrical Discharges in Magnetic Fields* ed A Guthrie and R K Wakerling (New York: McGraw-Hill).
- [2] Nedospasov A V 1992 *J. Nucl. Mater.* **196–198** 90.
- [3] Chen F F 1965 *Phys. Rev. Lett.* **15** 381.
- [4] Young K M 1967 *Phys. Fluids* **10** 213.
- [5] Robinson D C and Rusbridge M G 1971 *Phys. Fluids* **14** 2499.
- [6] Powers E 1974 *Nucl. Fusion* **14** 749.
- [7] J A Wesson, editor. Tokamaks. Clarendon Press, 2 edition, 1997.;
- [8] P C Stangeby. The Plasma Boundary of Magnetic Fusion Devices. IoP, 2000.
- [9] Levinson S J *et al* 1984 *Nucl. Fusion* **24** 527.
- [10] Tsui H Y W *et al* 1991 *Nucl. Fusion* **31** 2371.
- [11] Stangeby P C *et al* 1990 *Nucl. Fusion* **30** 1225.
- [12] Jun Cheng, PhD thesis, 2010, in Chinese.
- [13] S. J. Zweben and D. P. Stotler *et al.*, *Phys. Plasmas* **9**, 1981-1987 (2002).;
- [14] D. P. Stotler *et al.*, *Journal of Nuclear Materials* **313-316**, 1066-1070 (2003).
- [15] S. J. Zweben *et al.*, *Nucl Fusion* **44**, 134 (2004).
- [16] D. L. Rudakov *et al.*, *Plasma Phys. Control. Fusion* **44**, 717 (2002).
- [17] M. A. Meier *et al.*, *Phys. Rev. Lett.* **87**, 500 (2001).
- [18] S. J. Zweben *et al.*, *Phys. Plasmas* **17**, 102502 (2010).
- [19] R J Maqueda and G A Wurden. Fast imaging of visible phenomena in TFTR. *Nuclear Fusion*, **39**:629–636, 1999.
- [20] G Kocsis *et al.* A fast framing camera system for observation of acceleration and ablation of cryogenic hydrogen pellet in ASDEX Upgrade plasmas. *Rev.Sci. Inst.*, **75**(11):4754–4762, November 2004.
- [21] J L Terry *et al.*, Transport phenomena in the edge of Alcator C-Mod plasmas. *Nuclear Fusion*, **45**:1321–1327, 2005.
- [22] O Grulke, J L Terry, B LaBombard, and S J Zweben. Radially propagating fluctuation structures in the scrape-off layer of Alcator C-Mod. *Physics of Plasmas*, **13**, 2006.
- [23] G McKee *et al.*, The beam emission spectroscopy diagnostic on the DIII-D tokamak. *Review of Scientific Instruments*, **70**(1):913–916, 1999.
- [24] R J Maqueda *et al.*, Edge turbulence measurements in NSTX by gas puff imaging. *Review of Scientific Instruments*, **72**:931–934, 2001.
- [25] D P Stotler *et al.*, Three-dimensional neutral transport simulations of gas puff imaging experiments. *Contrib. Plasma Phys.*, **44**:294–300, 2004.
- [26] J R Myra *et al.*, Blob birth and transport in the tokamak edge plasma: analysis of imaging data. Submitted to POP, June 2006.
- [27] Maqueda R.J. *et al* 2003 *Rev. Sci. Instrum.* **74** 2020;
- [28] Zweben S.J. and Medley S.S. 1989 *Phys. Fluids B* **1** 2058;
- [29] Endler M. *et al* 1995 *Nucl. Fusion* **35** 1307
- [30] Thomsen H. *et al* 2002 *Phys. Plasmas* **9** 1233
- [31] Boedo J. *et al* 2001 *Phys. Plasmas* **8** 4826

CHAPTER 2. Measurements of Plasma Edge Turbulence

- [32] B. D. Dudson, Phd thesis, University of Oxford, 2007
- [33] Surko, C.M., Slusher, R.E., Phys. Rev. Lett. 37 (1976) 1747.
- [34] Mazzucato, M., Phys. Rev. Lett. 48 (1982) 1828.
- [35] Semet, A., et al, Phys. Rev. Lett. 45 (1980) 445.
- [36] J. M. Beall, Y. C. Kim, and E. J. Powers, J. Appl. Phys. 53(6), 1982.
- [37] S. J. Levinson, et al, Nuclear Fusion, 24(1984), No.5, 527
- [38] Young C. Kim and Edward J. Powers, IEEE Tran. Plasma Sci., PS-7(2), (1979) 120
- [39] B.Ph. van Milligen, et al, Phys. Plasmas 2 (8), 3017 (1995).
- [40] M. Jakubowski, R. J. Fonck, and G. R. McKee, Phys. Rev. Lett. 89, 265003-1/4 (2002).
- [41] G.R. McKee, et al., Phys. Plasmas 10, 1712 (2003).
- [42] C. Holland, et al., Rev. Sci. Ins., 75, 4278 (2004).
- [43] S.Chakraborty Thakur, et al., Rev. Sci. Ins., 83, 10D708 (2012).
- [44] R. C. Gonzalez and R. E. Woods, Digital Image Processing (Pearson Education, New Jersey, 2008)

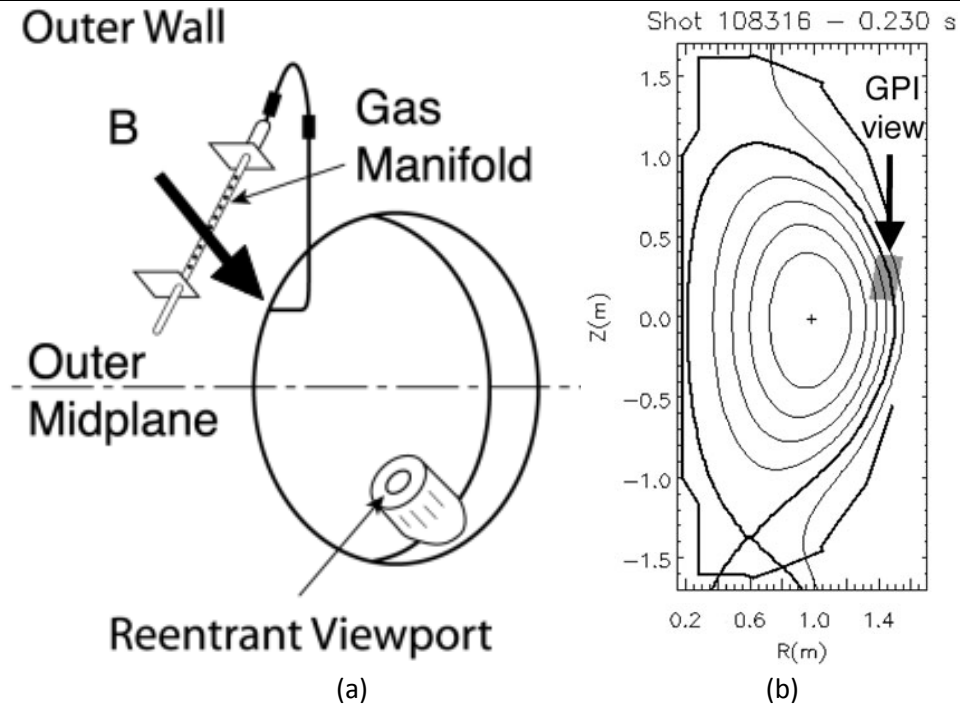


Fig. 2.1 GPI diagnostic geometry in NSTX. In (a) is a sketch of the vessel outer wall (as seen from the plasma) showing there-entrant viewport, the manifold from which the gas puff emerges and the approximate angle of the local magnetic field. In (b) is the area of the GPI view indicated by the rectangle just above the outer midplane near the separatrix.[15]

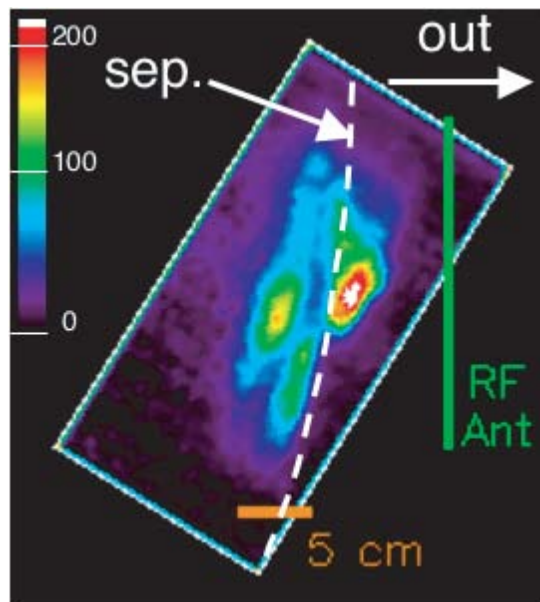


Fig. 2.2 Single image of the He I (587.6 nm) light emission in NSTX as viewed by the PSI camera with an exposure time of 10 μ s. [15]

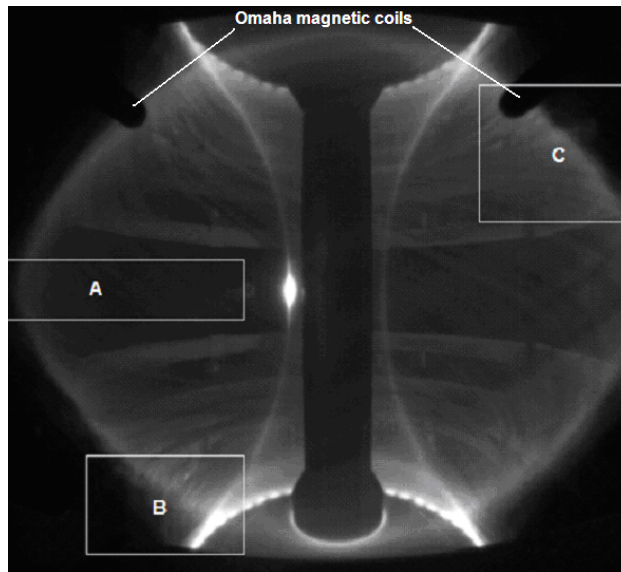


Figure 2.3: Full view of MAST from photron fast camera [32]

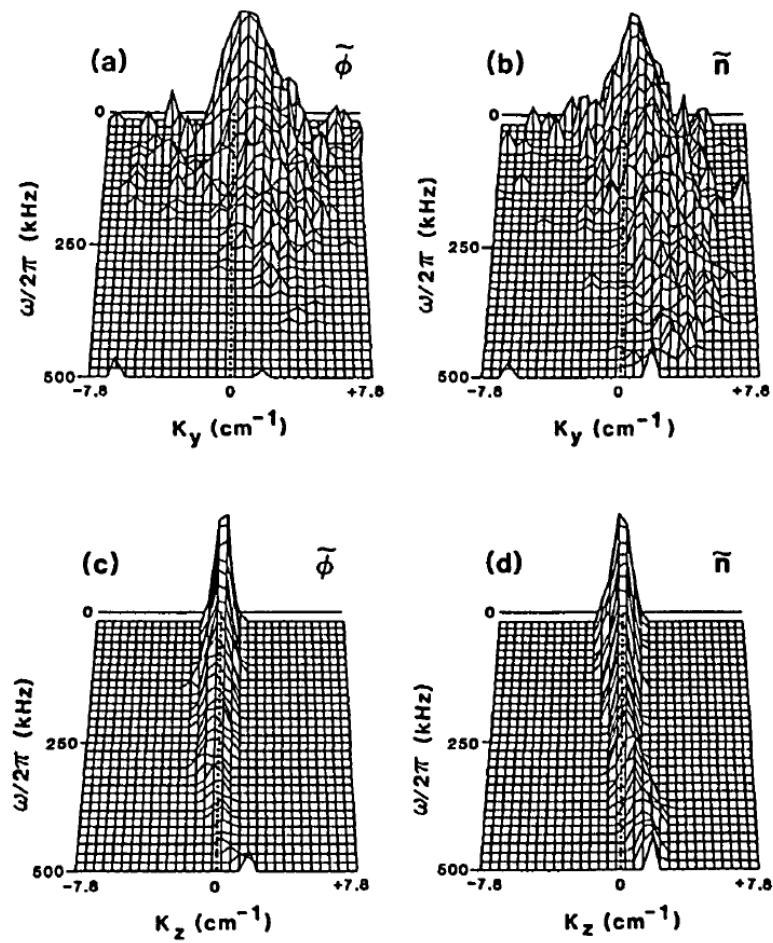


Fig. 2.4 $S(k, \omega)$ spectra. [37]

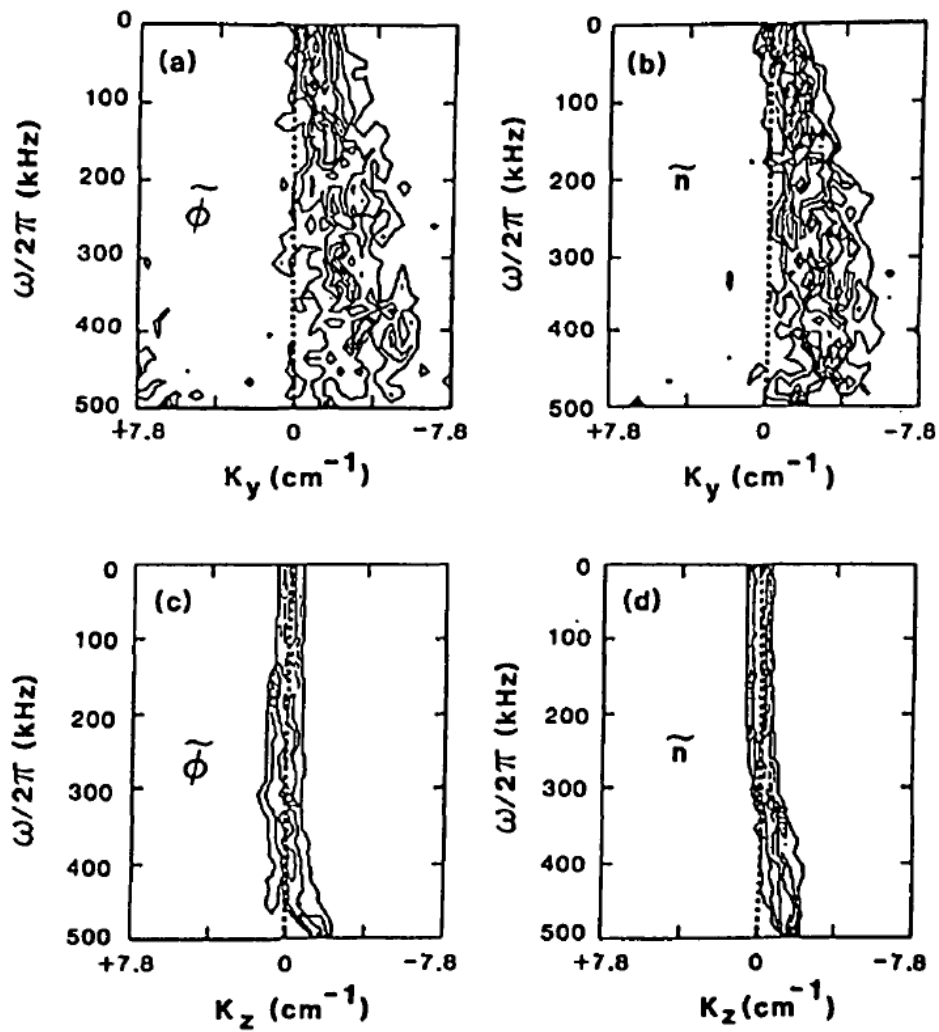


Fig. 2.5 Contour plots of the conditional spectra, $s(k|\omega)$, obtained for the data of Fig., emphasizing the different dispersive properties of the plasma. Each contour represents a 4% change from neighbouring contours. [37]

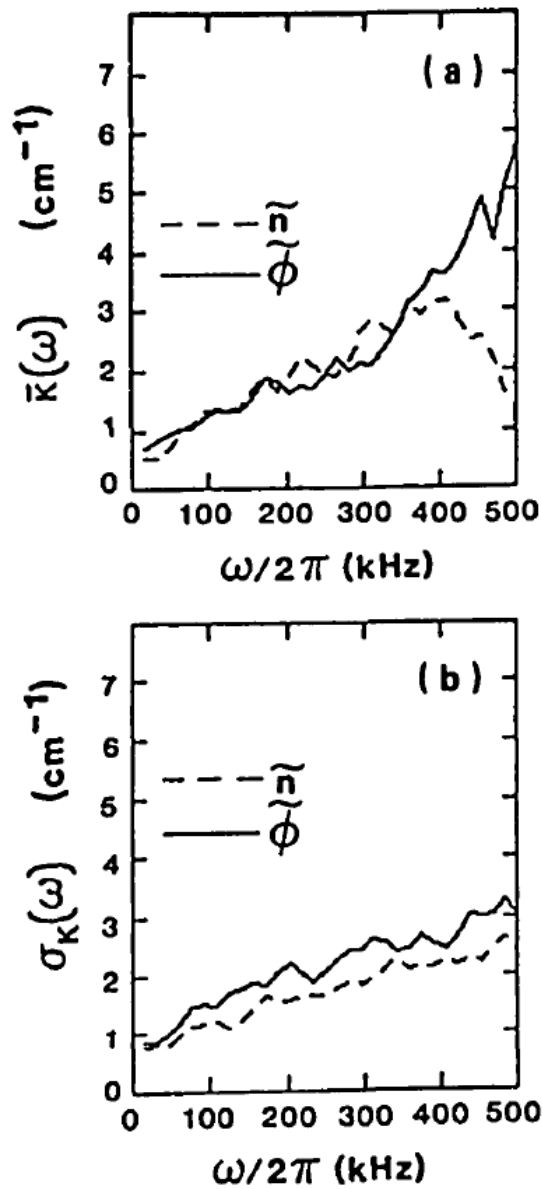


Fig. 2.6 First and second moments of $S(k_y|\omega)$ (from fig.), yielding the statistical dispersion relation $\bar{k}(\omega)$ in (a), and the root-mean-square broadening characterized by the spectral width $\sigma_k(\omega)$ in (b). These are shown for both $\tilde{\phi}$ and \tilde{n} . [37]

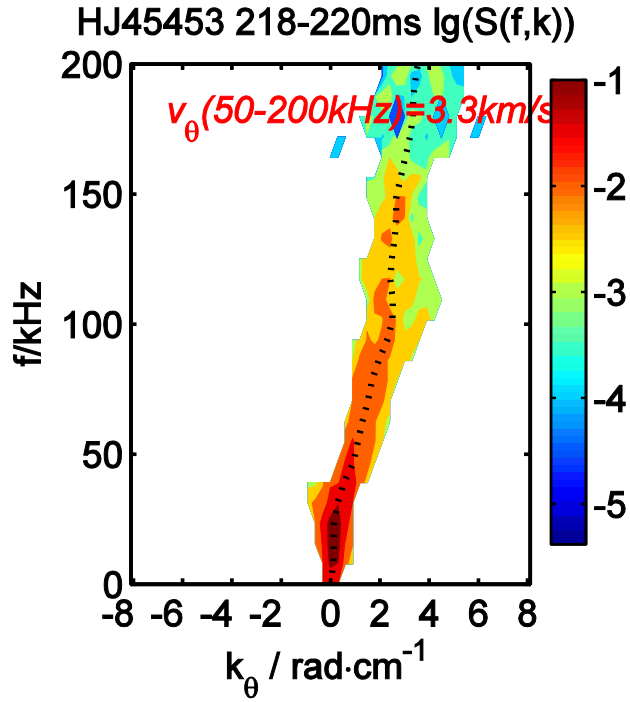


Fig. 2.7 $S(k, \omega)$ spectra using a Langmuir probe pair in Heliotron J. The position is 4mm inside of LCFS. To avoid the effect of MHD near 20kHz, the calculation only take frequency range of (50-200kHz).

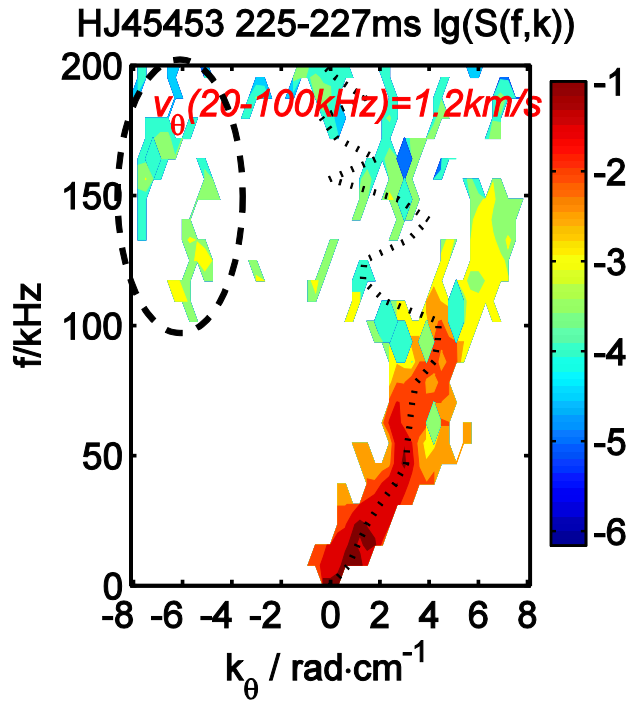


Fig. 2.8 $S(k, \omega)$ spectra using a Langmuir probe pair in Heliotron J. Fringe jump was produced over 100kHz, circled by the dashed line.

CHAPTER 2. Measurements of Plasma Edge Turbulence

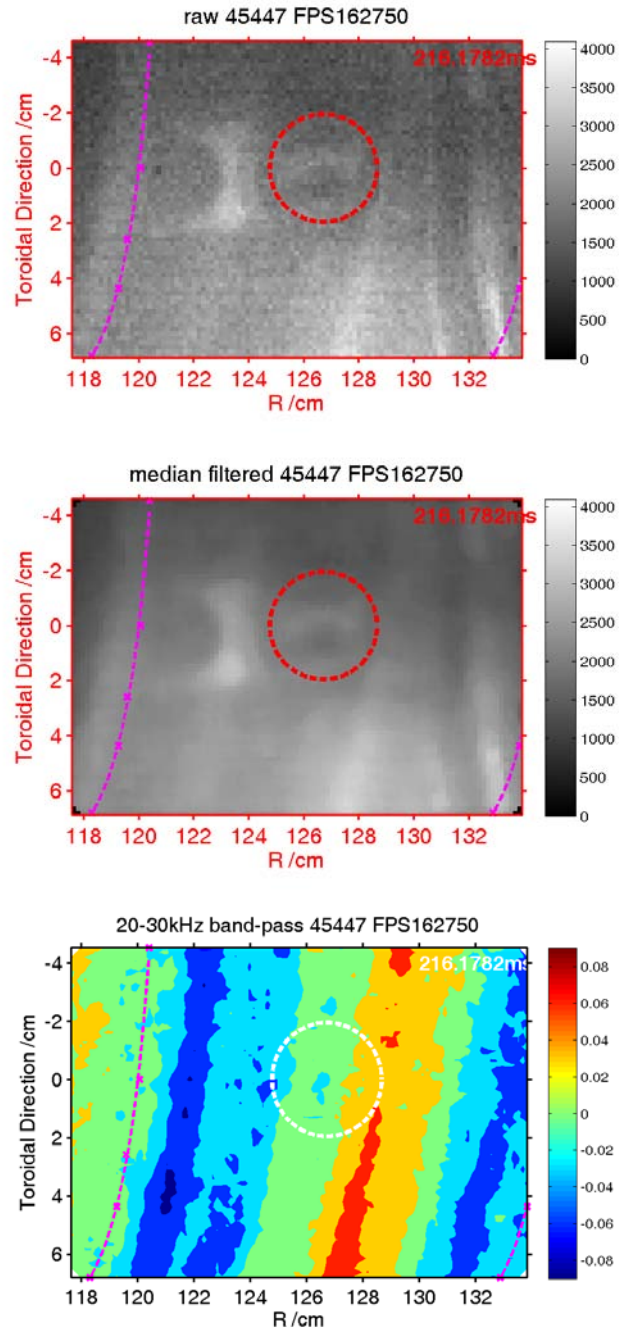


Fig. 2.9 (a) A raw image, and Fig. (b) An image processed with a 3×3 median filter. (c) A normalized 20-30kHz band-passed image.

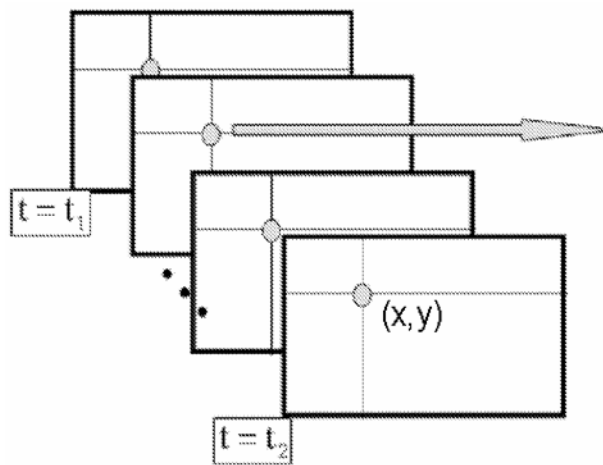


Fig. 2.10 Pixel data of a video

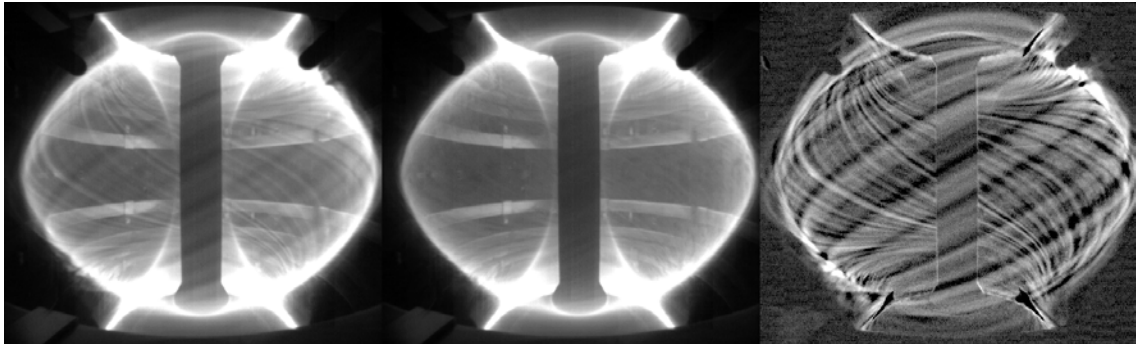


Figure 2.11 Fast camera images in MAST: Left is original, centre is background, and right is difference highlighting transient features [32]

Chapter 3. Heliotron J

3.1 Introduction

Heliotron J [1-3] is an advanced heliotron device [4] in Institute of Advanced Energy (IAE) of Kyoto University. The first plasma was generated in 2000, and the high-temperature plasma experiments have been being performed. **Figure 3.1** is a sided top view of Heliotron J. With the external coils, Heliotron J could extensively modify the vacuum magnetic field configuration flexibly. In stellarator/heliotron plasmas, the increase of NC ripple transport in the $1/\nu$ regime is a critical problem, thus to reduce this transport is one of the most important issues in advanced stellarator/heliotron devices. In Heliotron E, it is confirmed that the energy confinement time is improved by 30 % with the inward shift of the magnetic axis in ECH or NBI heating plasma. Since Heliotron E has a wide magnetic hill region, MHD instability is often observed with the increase of beta value. To enhance MHD stability by a magnetic well region in high beta plasma, the experiment with the outward shift of the magnetic axis was carried out. In that experiment, the bad particle transport was observed [5]. It is necessary to obtain good particle transport and MHD stability with a wide magnetic well region for stellarator/heliotron devices. In Heliotron J, this difficulty is attacked by the introduction of a helical-axis heliotron configuration [6,7]. The detailed goals of Heliotron J are: [1]

- (1) To optimize the helical-axis heliotron configuration.
- (2) To enhance MHD stability with good particle confinement.
- (3) A controllable particle and power-handling scheme (divertor).

In this chapter, the magnetic field configuration, the heating systems, the fueling systems, and the diagnostics of Heliotron J are described.

3.2 Characteristics of Magnetic Field Configurations of Heliotron J

3.2.1 Helical-axis Heliotron Configuration

Figures 3.2 (a)-(d) show the Poincaré plots of magnetic surfaces in the standard configuration of Heliotron J: (a) corner section $\phi = 0^\circ$, (b) $\phi = 22.5^\circ$, (c) central straight section $\phi = 45^\circ$, and (d) $\phi = 67.5^\circ$. A local quasi-isodynamic configuration can be constituted in the straight section. At the central straight section ($\phi = 45^\circ$), the magnetic field strength in the direction of major radius is almost constant where the magnetic field lines are nearly straight [1]; therefore the $\nabla\mathbf{B}$ drift and curvature drift can be reduced. The magnetic field strength at the corner section is larger than that at the straight section, thus the mirror-like

CHAPTER 3. HELIOTRON J

magnetic field can be generated. The trapped particles are confined at the straight section [1]. In a helical-axis heliotron configuration, a magnetic field configuration is mainly controlled by the toroidal, helical and bumpy components. **Figures 3.3(a)** and (b) show the rotational transform and the magnetic well depth, respectively, in the standard configuration. The rotational transform at the plasma edge is approximately 0.56 in the standard configuration and its variation over the entire plasma is small. The magnetic field configuration of Heliotron J is a low magnetic shear configuration. A wide magnetic well region can be realized over the entire plasma region. The well depth at the plasma edge is approximately 1.5 % in the standard configuration.

In a conventional planar-axis heliotron configuration, an inward magnetic axis shift is necessary for the improvement of trapped particle confinement. In contrast, a helical-axis heliotron configuration has more flexibility to control the mod B_{\min} structure by controlling the bumpy component externally [7]. This property is preferable to obtain the compatibility between MHD stability and good particle confinement.

Figure 3.4 shows a schematic view of Heliotron J. Heliotron J consists of a continuous helical coil (HF coil, $L = 1$, $M = 4$), a couple of toroidal coils (TA and TB) and three types of vertical coils (MV, AV and IV). In the figure, MV coil is not described. The continuous helical coil is wound on the torus with the winding law [9,10] as follow:

$$\theta = \theta_0 + \frac{M}{L}\phi - \alpha \sin\left(\frac{M}{L}\phi\right) \quad (3.1)$$

where θ is the poloidal angle and ϕ is the toroidal angle; $\theta_0 (= \pi)$ is the initial constant of the poloidal angle; $\alpha (= -0.4)$ is the pitch modulation of a coil. To ensure both the good particle confinement and the magnetic well, a negative pitch modulation is selected. TA and TB are installed at the straight and the corner sections, respectively. The bumpy component can be controlled by changing the coil current ratio between TA and TB. The maximum current, current and the number of turn for each coil are shown in **Table 3.1**. Each coil has an independent power supply system, thus the magnetic field configurations can be controlled flexibly by changing each coil current. Typical parameters of Heliotron J are shown in **table 3.2**. The major radius is 1.2 m and the averaged minor radius is 0.15-0.17 m. The magnetic field strength on the magnetic axis is 1.2-1.4 T and the rotational transform ($t/2\pi$) is about 0.56.

3.2.2 Edge Magnetic Field

Characteristics of edge magnetic field of Heliotron J are numerically investigated in [11]. Owing to the flexibility of field configuration control, helical or island divertor configurations can be realized in the same device. The island divertor field was numerically investigated in [12], and the asymmetric divertor plasma distribution for the helical divertor configuration was experimentally observed in [13].

STD configuration of Heliotron J has a helical divertor configuration. **Fig.3.5** shows Poincaré plots of vacuum field lines on a poloidal cross-section for STD configuration. For the edge region, the field lines on virtual magnetic surfaces outside the outermost magnetic surface (OMS) are traced within a region of $0.7 \text{ m} \leq R \leq 1.7 \text{ m}$ and $-0.5 \text{ m} \leq Z \leq 0.5 \text{ m}$. The divertor footprints on the wall are localized in some discrete regions in a torus.

In order to discuss edge plasma behavior diffusing from the confinement region, it is enough to trace field lines from the core edge region to the wall surface of the vacuum vessel. Under this condition, the structure becomes simple since the field lines starting the core edge region cross the wall before the so-called "fold and stretch" effect becomes noticeable.

Fig. 3.6(a) shows a Poincaré plot at $\varphi = 67.5^\circ$, where the edge field lines cross the wall. In this figure, the results of tracing field lines starting from the virtual flux surface (5.0 mm outside the OMS) are plotted. As shown in this figure, only one "divertor leg" reaches to the wall at this toroidal position. The divertor footprints are plotted in **Fig. 2.6(b)**. As in **Fig. 2.6(b)**, the divertor footprints are localized not only in poloidal direction but also in toroidal direction. This stands in contrast to the helical divertor in Heliotron E [14], where the divertor trace continuously runs along the torus helically. The different color in **Fig. 2.6(b)** denotes the difference in the direction of the field trace. It is expected that the diffused plasma from the core region go to the wall divided into parallel and anti-parallel flows to the field line. This is convenient to investigate divertor plasma physics such as plasma flow and/or SOL current and also to study divertor biasing effects, etc.

3.3 Heating Devices

Fig. 3.7 is the schematic view of heating systems, fuelling systems and some diagnostics in Heliotron J. Three types of heating system are installed: ECH, NBI heating and ion cyclotron resonance heating (ICH). In this section, we describe three heating systems in Heliotron J.

- **Neutral Beam Injection Heating**

Neutral beam injection heating is a method to heat plasmas by injection of accelerated neutral particles into plasmas. The production of neutral beam involves several processes. In order to accelerate particles, ions are produced in the ion source. The ions are extracted from the ion source and accelerated. This ion beam should be neutralized to produce a neutral beam. The neutralization is achieved by passing this ion beam through a gas in the neutralizer. In result, a beam of energetic neutral atoms is produced. Injected neutral particles become ionized through collision or charge exchange process. Those ionized neutral particles transfer energy to electrons and ions in plasmas through Coulomb collisions. Neutral particles are unaffected by the magnetic field, thus it is desirable that as much as power is deposited in the central region of plasmas. In Heliotron J, **figure 3.8** shows two types of hydrogen neutral beam lines (BL1 and BL2) with positive ion sources [15]. One is co-injection (BL2) and the other is counter-injection (BL1) for the normal direction of magnetic field. Here, co-direction is defined as the direction of plasma current, which increases the rotational transform. The maximum acceleration voltage and maximum port-through injection power of each beam are 30 kV and 0.8 MW, respectively. The pitch angle between beam lines and magnetic axis for BL1 and BL2 are 145° - 175° , 5° - 40° for the normal direction of magnetic field, respectively. The divergence angle of each beam is about 1.2° .

- **Electron Cyclotron Resonance Heating**

Electron cyclotron resonance heating is one of methods, which transfers energy to plasma by electromagnetic waves. When an electromagnetic wave propagates through plasma,

CHAPTER 3. HELIOTRON J

the electric field of wave accelerates the charged particles that heat plasma by collisions. Characteristic of ECH is as follow: electromagnetic waves in plasmas are subject to resonant absorption, thus we can carry out the localized plasma heating. In Heliotron J, plasma is generated and heated by 2nd harmonic X-mode ECH, whose frequency is 70 GHz and maximum injection power is 0.4 MW [4]. **Figure 3.9** shows a schematic view of ECH system in Heliotron J. The electromagnetic wave is injected at #9.5 port and to be parallel to the magnetic axis. We can change an injection angle by using mirrors.

- **Ion Cyclotron Resonance Heating**

Ion cyclotron resonance heating is a method, which transfers energy to ions in plasmas by electromagnetic waves. When an electromagnetic wave propagates through plasma, the electric field of wave accelerates the charged particles, which heat plasma by collisions. In Heliotron J, the minority heating for hydrogen ion is carried out by using two antennas installed at #14.5 port [16]. The frequency of injection wave can be changed as 19.0 and 23.2 MHz and that allows us to choose heating position, on the plasma core or periphery (see **figure 3.10** for the standard configuration), respectively. Total maximum injection power is about 1.5 MW.

3.4 Fueling Devices

The optimization of gas fueling scenarios has been studied to improve the plasma performance in Heliotron J. Three gas fueling methods have been applied in Heliotron J.

- **Normal Gas-Puffing (GP)**

For density control, usually used is a conventional gas-puffing system with four piezoelectric valves. These valves are installed at the inboard-side ports (low field side injection) at $\approx 90^\circ$ intervals around the torus (“Gas” in **Fig. 3.7**). These ports are located in the low field side nevertheless they are in inboard side since the field strength is usually higher near the helical coil. The amount of H (or D) atoms from the GP system with the plenum pressure of ~ 0.15 MPa is pre-programmed to control the line-averaged density. Since, due to the space limitation, the nozzles of these valves do not directly see the plasma, the induced gas from the valve diffuses to the discharge chamber after multiple reflections in an elbow-shaped pipe connecting the nozzles to the chamber. [17]

- **High Intensity Gas-Puffing (HIGP)**

- **SMBI**

An SMBI system of hydrogen is equipped on two horizontal outboard-side ports (the port number: #3.5-illustrated in **Fig. 3.11**, and #11.5). The system consists of a fast piezoelectric valve with a short conic (or Laval-type) nozzle with the orifice size of 0.2 mm^ϕ . The amount of H atoms injected with the SMBI is controlled by changing the pulse width of each SMBI valve under a fixed plenum pressure ($\sim 1\text{--}2$ MPa). [17]

3.5 Diagnostics

3.5.1 Edge turbulence diagnostics

- **Langmuir Probe (LP)**

CHAPTER 3. HELIOTRON J

As shown in **Fig. 3.12**, four Langmuir Probe arrays have been installed in Heliotron J. At #7.5 and #8.5 the probe arrays measure the fluctuation at X-point, while at #11.5 and #14.5 the measurements are at O-point. In this thesis we focus on the measurement at #14.5. Details of the probe features are described in CH. 4 and CH. 5.

- **Gas-Puff Imaging (GPI)**

Two high-speed video cameras (fast camera) have been installed at #11.5 and #14.5, respectively. At #11.5, plasma is naturally illuminated when SMBI is being fueled. At #14.5, a gas-puff nozzle is installed to illuminate the top plasma edge. The details are described in CH.3 and CH.5, respectively.

3.5.2 Other diagnostics

- **Microwave Interferometer**

A microwave interferometer is a technique to measure the phase shift of microwave, which travels in the plasma, by comparing with the phase of the reference wave. We can evaluate the electron density from the phase shift. However the phase shift has a line integral effect on a traveling path, strictly speaking, as that it is a line-averaged electron density. In Heliotron J, we installed the microwave interferometer of O-mode injection, whose frequency is 130 GHz at #8.5 port. The cut-off electron density for this system is about $2.1 \times 10^{20} \text{ m}^{-3}$.

- **Diamagnetic Loop**

A diamagnetic loop measures the change of magnetic flux in toroidal direction by poloidal loop around the plasma. The plasma acts to decrease the magnetic field due to the diamagnetism. The measurement of the diamagnetic effect is an important measurement of the plasma-stored energy (W_p), because the change of magnetic flux is proportional to the averaged pressure on the magnetic surface. Therefore we can evaluate W_p via the diamagnetic loop.

- **Charge-exchange Neutral Particle Analyzer (CX-NPA)**

A charge-exchange neutral particle analyzer has been used to measure ion temperature and fast ion distribution [19]. In general, it is difficult for ions, which are confined in magnetic field, to escape from plasma. However ions change to neutral particles via charge-exchange reaction with cold neutral particles, then those neutral particles can escape from the plasma without suffering collisions. An example of charge-exchange reaction is written by,



where H_{PL}^+ , H_{cold}^0 , H_{CX}^0 , and H_{cold}^+ is the hydrogen ion, cold neutral particle, charge-exchange neutral particle and ionized hydrogen ion, respectively. Since charge-exchange reaction does not make momentum transfer but does make electron capture, the charge-exchange neutral particle escapes the plasma with the momentum of H_{PL}^+ .

Therefore we can investigate the ion energy distribution by analyzing the energy of charge-exchange neutral particle.

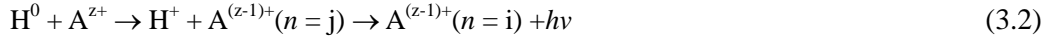
Figure 3.13 shows a schematic view of CX-NPA system, which is installed at #5.5 port, in Heliotron J. This system is the $E//B$ type and consists of charge stripping cell, defect

CHAPTER 3. HELIOTRON J

electromagnet, electrostatic deflection plate, and micro channel plate. We can control the magnetic field strength of defect electromagnet from 0.05 T to 0.4 T and the electric field strength of electrostatic deflection plate from 0.16 kV to 10 kV. This system has 20 channels: 10 for hydrogen ion and 10 for deuterium ion. The maximum measurable energy is 80 keV for hydrogen ion and 40 keV for deuterium ion. The energy resolution is 5-10 % [20].

- **Charge-eXchange Recombination Spectroscopy (CXRS)**

A charge-exchange recombination spectroscopy method is to measure an emission line from the hydrogen-like ion, which is generated by charge-exchange recombination reaction between neutral beam particle and fully ionized impurity [21]. The sort of reaction is described as follow:



where A denotes a species of impurity; usually we use light impurity, such as carbon and oxygen. In addition, n means an excited state of $\text{A}^{(z-1)+}$. The charge-exchange recombination spectroscopy allows diagnosis of essential plasma parameters as passive spectroscopy: impurity ion temperature and plasma flow velocity. The ion temperature and flow velocity are estimated from the Doppler broadening and the Doppler shift of the spectral line, respectively. This method has three major characteristics: (1) It allows otherwise fully stripped impurities to radiate, (2) it allows them to radiate locally where the beam intersects the plasma, giving crossed-sightline localization, and (3) it allows them to radiate at convenient wavelengths, such as visible light [20]. In Heliotron J, we installed the CXRS system to measure the radial profiles of parallel flow velocity and ion temperature at #3 port and #7 port. Details of CXRS system in Heliotron J are described in Chapter 3.

- **Beam Emission Spectroscopy(BES)**

The radial and the poloidal structure of the density fluctuation have been evaluated by the spectral measurement of the Doppler-shifted light emission followed by the collisional excitation process between the hydrogen or deuterium neutral beam atoms and plasmas. The BES measurements have greatly advanced our understanding of the physics of magnetohydrodynamic (MHD) activities and long-wavelength plasma turbulence.

- **Thomsen Scattering System**

Thomson scattering of laser light is a popular method of measuring electron temperature and density in plasma. This method measures the scattering emission due to electrons in the plasma. The electron density and temperature are estimated from the absolute intensity of scattering emission and the Doppler broadening, respectively. In Heliotron J, a TV Thomson scattering system is installed at #10.5 port. A ruby laser is installed as a diagnostic laser whose wavelength, maximum power, and pulse width are 694.3 nm, 10 J, and 25 ns, respectively.

- **Amplitude Modulation (AM) Reflectrometer**

The reflectometry is a technique to measure the phase of reflected microwave, which is injected into plasma, at a cutoff layer and to evaluate the phase shift compared with the phase of reference wave, which does not through plasma [22]. By sweeping of injected microwave frequency, it allows us to measure the electron density profile. In Heliotron J, an amplitude modulation (AM) reflectometer is installed at #15.5 port. An AM reflectometer detects the envelope phase of the amplitude-modulated microwave in order to reduce the effect of density fluctuations and fringe jumps in the profile measurement [23]. The carrier frequency ranges

CHAPTER 3. HELIOTRON J

from 33 to 56 GHz, and can be swept linearly with a sweeping frequency of up to 2 kHz. The modulation frequency is 200 MHz [24]. The X-mode is selected as the propagation mode in order to measure a hollow density profile. In the low-density plasma ($\bar{n}_e < 1.0 \times 10^{19} \text{ m}^{-3}$), this system can measure the electron density profile from the plasma core to the plasma edge [24].

References

- [1] T. Obiki *et al.*, *Plasma Physics and Controlled Fusion*, **42** (2000) 1151.
- [2] F. Sano *et al.*, *Journal of Plasma Fusion Research SERIES*, **3** (2000) 26.
- [3] T. Obiki *et al.*, *Nuclear Fusion*, **41** (2001) 833.
- [4] M. Wakatani, *Stellarator and Heliotron Devices* (Oxford, New York, 1998).
- [5] M. Wakatani and S. Sudo, *Plasma Physics and Controlled Fusion*, **38** (1996) 937.
- [6] M. Wakatani *et al.*, *Nuclear Fusion*, **40** (2000) 569.
- [7] M. Yokoyama *et al.*, *Nuclear Fusion*, **40** (2000) 261.
- [8] A.H. Boozer, *Physics of Fluids*, **23** (1980) 904.
- [9] Research Report in Institute of Advanced Energy, Kyoto University, IAE-RR-98
(in Japanese).
- [10] Research Report in Institute of Advanced Energy, Kyoto University, IAE-RR-2000
(in Japanese).
- [11] T. Mizuuchi *et al.*, *J. Plasma Fusion Res. SERIES* **3**, 192-196 (2000).
- [12] T. Mizuuchi *et al.*, *J. Nucl. Mater.* **290-293**, 678-682 (2001).
- [13] T. Mizuuchi *et al.*, *J. Nucl. Mater.* **313-316**, 947-951 (2003).
- [14] T. Mizuuchi *et al.*, *J. Nucl. Mater.* **162-164**, 105 (1989).
- [15] S. Kobayashi *et al.*, *20th IAEA Fusion Energy Conference 2004*,
IAEA-CN-116/EX/P4-41.
- [16] H. Okada *et al.*, *15th International Heliotron/Stellarator Workshop*, Madrid (2005).
- [17] T. Mizuuchi *et al.*, *J. Nucl. Mater.* **S453-S458**, 438 (2003).
- [18] S. Oshima, 合同研究会 2012.
- [19] V.V. Afrosimov *et al.*, *Soviet Physics - Technical Physics*, **5** (1961) 1378.
- [20] M. Kaneko *et al.*, *Journal of Plasma Fusion Research*, **7** (2006) 77.
- [21] R.C. Isler, *Plasma Physics and Controlled Fusion*, **36** (1994) 171.
- [22] C. Laveron *et al.*, *Plasma Physics and Controlled Fusion*, **38** (1996).
- [23] J. Sanchez *et al.*, *Review of Science Instruments*, **63** (1992) 4654.
- [24] K. Mukai *et al.*, *Contributions to Plasma Physics*, **50** (2010) 646.

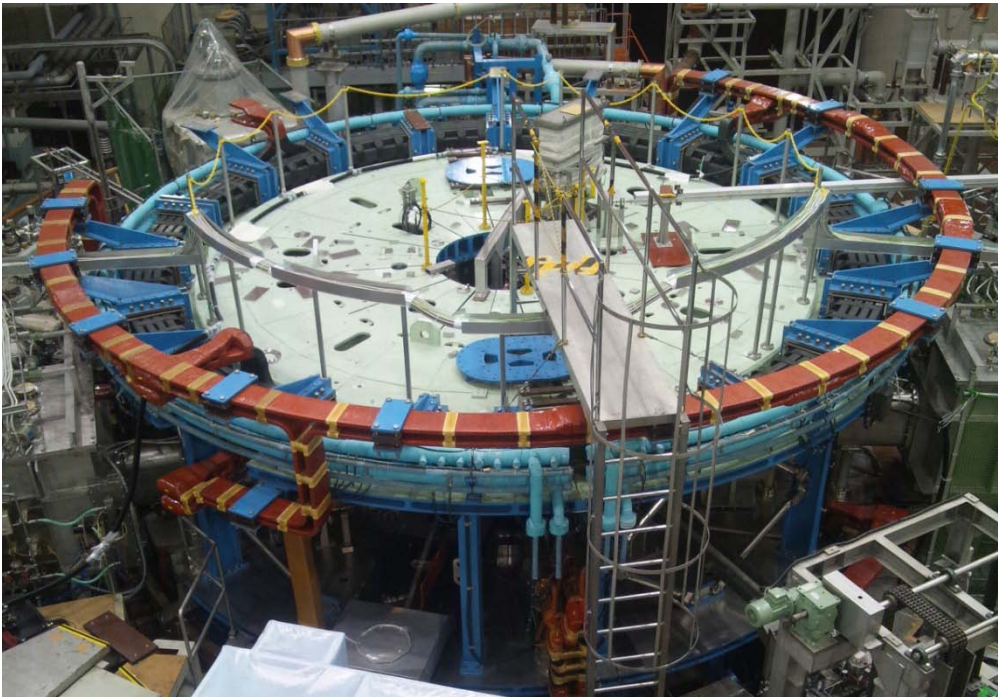


Figure 3.1 Heliotron J.

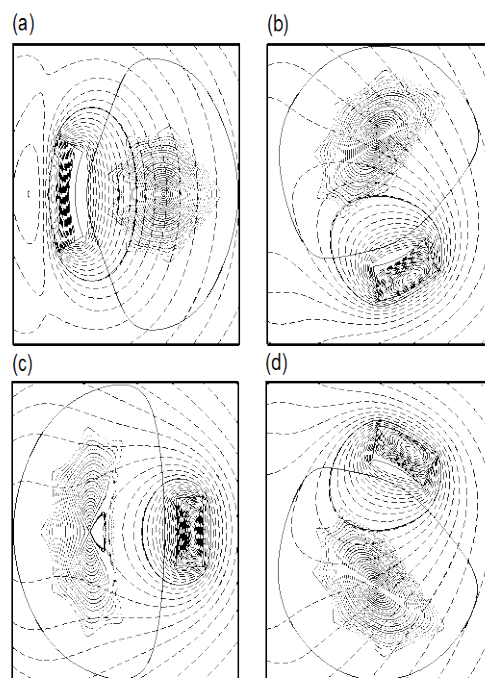


Figure 3.2 Magnetic surfaces in vacuum and magnetic field strength line with inner vacuum wall surface at four toroidal cross sections in the standard configuration of Heliotron J.

CHAPTER 3. HELIOTRON J

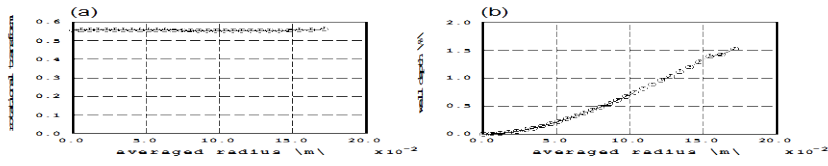


Figure 3.3 Radial profiles of (a) rotational transform and (b) well depth in the standard configuration of Heliotron J.

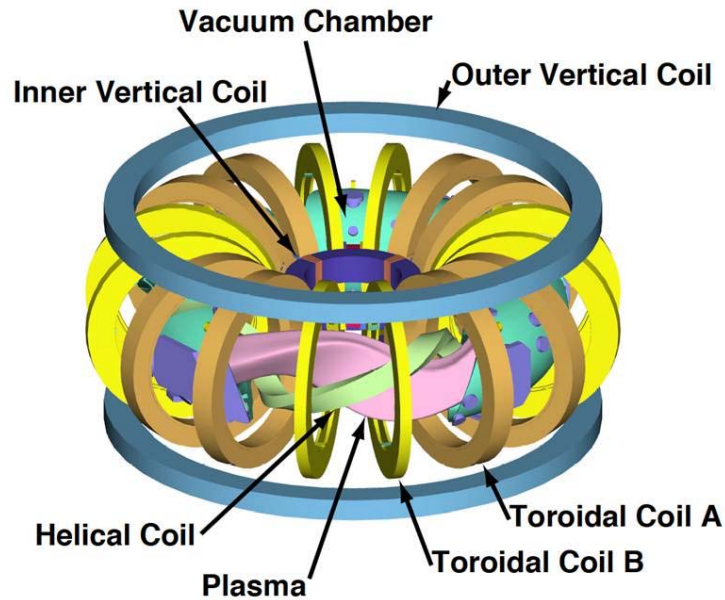


Figure 3.4 Schematic views of vacuum chamber and coils of Heliotron J.

| Coil | Maximum current (kA) | Current per one turn (kA) | Number of turn (T) |
|------|----------------------|---------------------------|--------------------|
| H | 960 | 120 | 8 |
| TA | 600 | 120 | 5 |
| TB | 218 | 10.9 | 20 |
| V | 840 | 120 | 7 |
| AV | 144 | 6 | 24 |
| IV | 480 | 6 | 80 |

Table 3.1 Maximum current, rating current and the number of turn for each coil.

CHAPTER 3. HELIOTRON J

| | |
|--|-------------|
| Major radius, R | 1.2 m |
| Averaged minor radius, $\langle a \rangle$ | 0.15-0.17 m |
| B_{ax} | 1.2-1.4 T |
| Rotational Transform ($t/2\pi$) | 0.56 |

Table 3.2 Typical plasma parameters in Heliotron J.

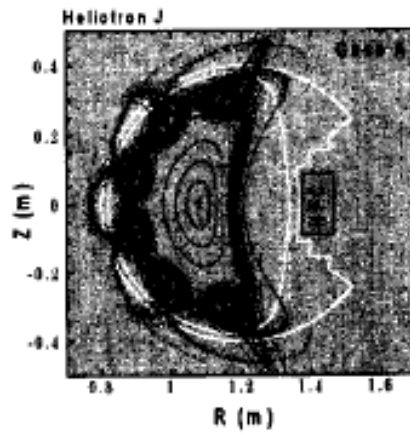


Fig. 3.5 Poincaré plots on a poloidal cross-section at a toroidal angle of $\varphi=45^\circ$. White lines indicate the vacuum vessel. [11]

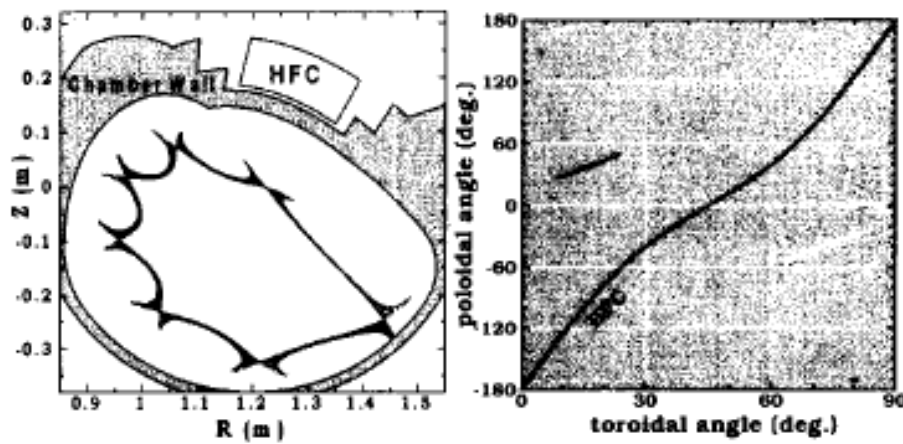


Fig. 3.6 (a) Poincaré plots of edge field lines within the vacuum chamber at $\varphi=67.5^\circ$; (b) Divertor footprint on the wall. (Note the toroidal angle of one period is 90°). [11]

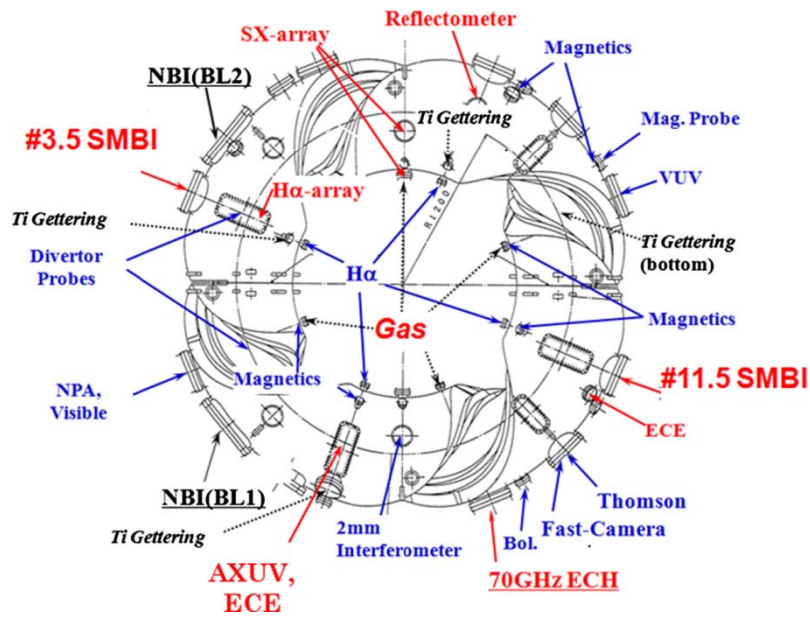


Figure 3.7 Schematic view of heating systems, fuelling systems and some diagnostics.

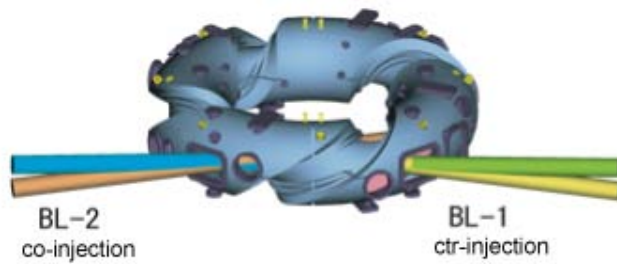


Figure 3.8 Schematic view of NBI system.

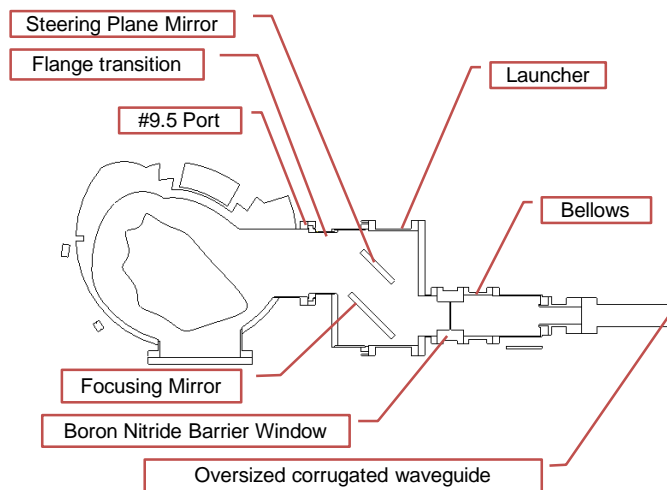


Figure 3.9 Schematic view of ECH system.

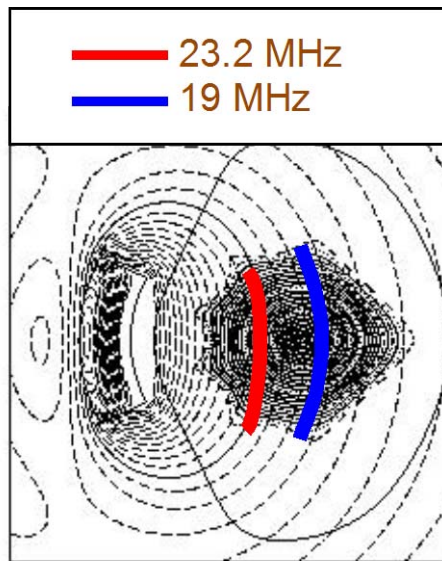
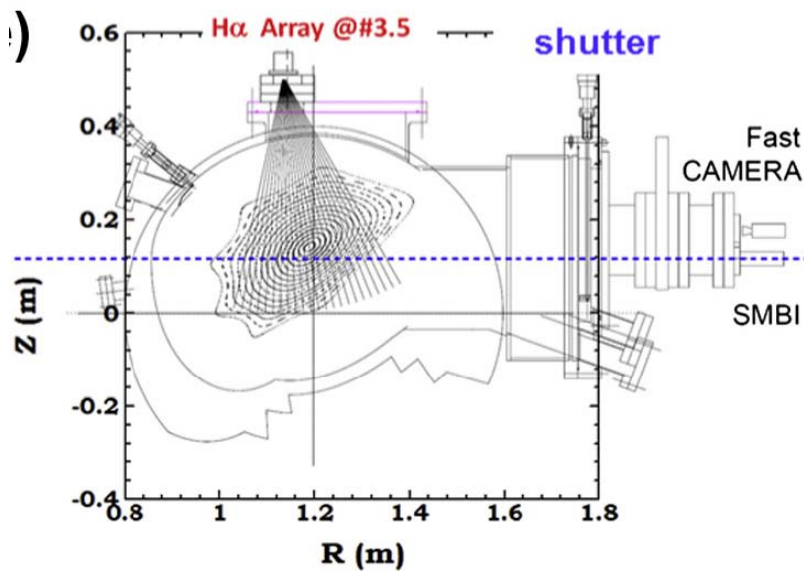


Figure 3.10 Resonance layers for ICRF in the standard configuration.



3.11 A schematics of #3.5-SMBI.

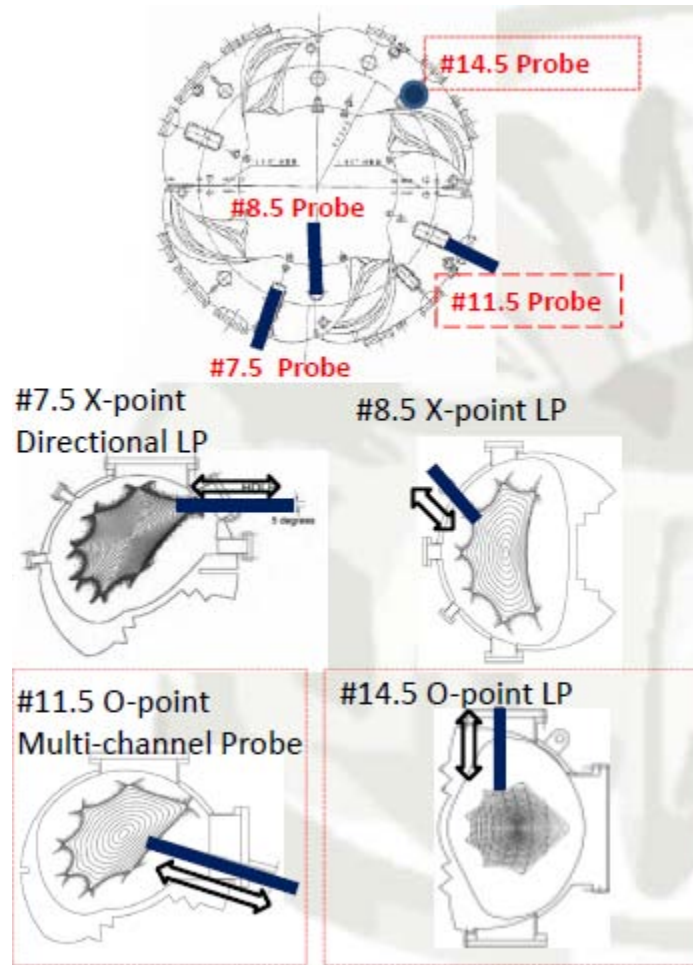


Fig. 3.12 A schematics of the four probe arrays in Heliotron J [18].

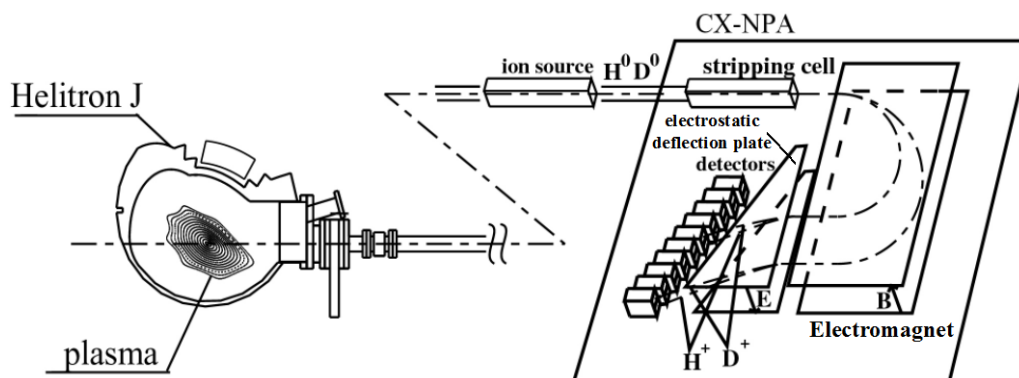


Figure 3.13 Schematic view of NPA system.

Chapter 4. Effect of SMBI on edge fluctuation and particle transport in Heliotron J

The fluctuation near the last closed flux surface (LCFS) in Heliotron J is studied in a supersonic molecular-beam injection (SMBI) fuelled NBI plasma. A Langmuir probe array is installed to measure the fluctuations of both ion saturation current (I_s) and poloidal electric field (E_θ). Two different fluctuation characteristics are observed after SMBI. First, just after SMBI for a short period, I_s fluctuation level is increased in the low frequency range, and the fluctuation state changed from a coherent-mode-dominated and nearly Gaussian to an intermittent and non-Gaussian one. The sharp increase of fluctuation induced particle flux is considered to be one of the reasons of degradation of plasma stored energy (W_p). Second, the fluctuation induced particle transport was reduced long after SMBI, suggesting better particle confinement in W_p climbing phase. We expect the short effect period of gas injection to the edge fluctuation might be an advantage of this novel fueling technique.

4.1 Introduction

Fueling control is one of the most important issues to obtain high-density and high-performance plasmas. The supersonic molecular-beam injection (SMBI) technique¹ is an effective fueling method for deeper penetration of neutral particles into the core plasma and higher fuelling efficiency compared to conventional gas-puff.^{2,3} An SMBI system has been applied to the Heliotron J device and successfully extended the operation region of line-averaged electron density () versus plasma stored energy (W_p).⁴⁻⁶

Edge region in magnetically confined plasmas plays an important role in the interaction between the plasma and the first-wall and/or divertor structure. The cross-field plasma transport through the edge is recognized to be dominated by turbulence.⁷⁻⁹ It is commonly believed that the cross field transport is mainly driven by $\mathbf{E} \times \mathbf{B}$ drift due to the fluctuation poloidal component of the electric field, and the turbulent transport due to the radial component of magnetic fluctuations is small compared with electrostatic transport.

In this paper, we report the change of density and potential fluctuations in the edge and the fluctuation induced particle transport after SMBI, to understand the effects of SMBI on

CHAPTER 4 Effect of SMBI on edge fluctuation and particle transport in Heliotron J

the confinement. Organization of this paper is as follows. Section 2 describes the hardware set-up of the experiment. Section 3 gives the data analysis method. In section 4, the detailed results and analysis is described. In Section 5 we have some discussions. Finally, a conclusion is presented in section 6.

4.2 Experimental set-up

Heliotron J is a medium sized helical-axis heliotron device ($\langle R_0 \rangle / \langle a \rangle = 1.2\text{m}/0.17\text{m}$, $\langle B_0 \rangle \leq 1.5\text{T}$) with an $L = 1M = 4$ helical coil. A top view of the torus vacuum chamber is illustrated in Fig. 1. Magnetic configuration characteristics of this device are reported in refs. 10 and 11. In the previous studies, edge plasma behavior outside the X-point and O-point (a position between two adjacent X-points) of the separatrix has been investigated in ECH plasmas using Langmuir probes.^{12,13}

In this study, we focus on the boundary fluctuation at an O-point at #14.5 toroidal section for NBI plasmas with a SMB injection from #11.5 toroidal section. The positions of #14.5 and #11.5 are labeled in Fig.1. A Hybrid probe was vertically inserted from the top of #14.5 section, and located at the LCFS, as shown in Fig. 2. The hybrid probe consists of a set of Langmuir probe array and a set of magnetic probes. The structure of the Langmuir probe array is illustrated in Fig. 3. The five pins of the array are aligned along poloidal direction. Signal names of the pins are also labeled in the figure, in which I_s stands for the ion saturation current and V_f for the floating potential. The SMBI nozzle is installed at #11.5 port as shown in Fig. 1, and a short pulse of supersonic molecular beam of Hydrogen was horizontally injected into the plasma.

4.3 Analysis Approach

When there is magnetic fluctuation, the total fluctuation induced particle flux is,

$$\Gamma_{tur} = \frac{\langle \tilde{n}_e \tilde{E}_\theta \rangle}{B_t} + v_{||} \frac{\langle \tilde{n}_e \tilde{B}_r \rangle}{B_t} \quad (4.1)$$

which means the radial component of magnetic fluctuation will also bring transport. However, in this paper we only considered the local electrostatic fluctuation, magnetic effect is neglected.

The fluctuation induced particle flux Γ for a small spectral band width $\delta\omega$ at the focused frequency is calculated using the following equation.¹⁴

$$\Gamma_{\delta\omega} = \langle \tilde{n} \tilde{v} \rangle_{\delta\omega} = \frac{2}{B} \text{Re}[P_{nE}(\omega)] \quad (4.2)$$

Here, $\text{Re}[]$ means the real part of a complex, P_{nE} is the cross-power spectrum between density and electric field fluctuations. By using the Langmuir probe data, we take I_{s1} as the proxy of n_e , and $(V_{f5} - V_{f2})/dl$ (dl : the distance between pin-2 and pin-4, 4 mm in this experiment) as the proxy of poloidal electric field E_θ neglecting the effects of temperature and its fluctuations. Equation (1) is then rewritten to be the following equation.

CHAPTER 4 Effect of SMBI on edge fluctuation and particle transport in Heliotron J

$$\Gamma_{\delta\omega} \sim \frac{2}{B} \text{Re}[P_{I_s-E_\theta}(\omega)] = \frac{2}{B} |\gamma_{I_s-E_\theta}(\omega)| \cos \alpha_{I_s-E_\theta}(\omega) P_{I_s}(\omega)^{1/2} P_{E_\theta}(\omega)^{1/2} \quad (4.3)$$

Here, $P_{I_s-E_\theta}(\omega)$ is the cross-power spectrum, $|\gamma_{I_s-E_\theta}(\omega)|$ is the coherence spectrum, and $\alpha_{I_s-E_\theta}(\omega)$ is the phase spectrum between I_s and E_θ ; $P_{I_s}(\omega)$ is the auto-power spectrum of I_s , and $P_{E_\theta}(\omega)$ is the auto-power spectrum of E_θ . The total flux in the interested frequency range is then written to be:

$$\Gamma_{total} \sim \frac{2}{B} \sum_{\omega} |\gamma_{I_s-E_\theta}(\omega)| \cos \alpha_{I_s-E_\theta}(\omega) P_{I_s}(\omega)^{1/2} P_{E_\theta}(\omega)^{1/2} \quad (4.4)$$

To understand what roles I_s and E_θ play separately, we calculate the fluctuation amplitude of I_s and E_θ in the interested frequency range, respectively, in the following way:

$$\tilde{I}_s = [\sum_{\omega} P_{I_s}(\omega)]^{1/2} \quad (4.5)$$

$$\tilde{E}_\theta = [\sum_{\omega} P_{E_\theta}(\omega)]^{1/2} \quad (4.6)$$

4.4 Experiment result and analysis

Core plasma parameters relating to this study for a discharge with SMBI are shown in Fig. 4. In this discharge, the magnetic configuration was the standard one of Heliotron J.¹⁵ Plasma is heated only by NBI. Open duration of the SMB nozzle is 1ms, and the injection timing is at 221.9ms. Sharp increase of the H α signal (#11.5H α), which is measured at the same toroidal position with SMBI, clearly shows the arrival timing of the molecular beam. The line-averaged electron density started to increase after SMBI. However just after SMBI (223-227ms, labeled by the purple shadow), W_p temporarily dropped, then from $t \sim 227$ ms W_p started to increase. In the following analysis, three phases are defined for convenience: I) before SMBI phase, which is the period before the injection timing at 221.9ms; II) W_p degradation phase, which is a short time window just after SMBI, during 223-227ms; III) W_p climbing phase, which follows the W_p degradation window, beginning from ~ 228 ms. The amplitude spectrum of I_s fluctuation level $\tilde{I}_s / \langle I_s \rangle$ ($\langle I_s \rangle$ is the time averaged value of I_s), the amplitude spectrum of E_θ and the spectrum of fluctuation induced particle flux Γ in these three phases are shown in Figs. 4(a), (b) and (c), respectively.

A. Before SMBI phase

In Fig. 5, green dash lines show the spectra before SMBI. There is one local peak at 20-30 kHz in the spectra of $\tilde{I}_s / \langle I_s \rangle$, \tilde{E}_θ and Γ . Figure 6 shows the coherence spectrogram between V_f and the magnetic signal B_t from a magnetic probe in the probe body.

CHAPTER 4 Effect of SMBI on edge fluctuation and particle transport in Heliotron J

Before SMBI, high coherence was observed in 20-30 kHz. This suggests the peak we observed on $\tilde{I}_s / \langle I_s \rangle$ and \tilde{E}_θ power spectra in Fig. 5 is related to some MHD mode. This 20-30 kHz fluctuation mode has a finite phase angle between the density and potential, thus introduces significant fluctuation induced particle flux. Although another local peak at 70-80 kHz was observed in \tilde{E}_θ , which had also high coherence with the magnetic fluctuation, it was not observed in $\tilde{I}_s / \langle I_s \rangle$ and Γ . Although the different effects of these two local peaks on $\tilde{I}_s / \langle I_s \rangle$ and \tilde{E}_θ are interesting, we need more detailed investigations. In this paper, however, we focus on the change of turbulence characteristics in rather low frequency range ($< 40\text{kHz}$) since no significant fluctuation induced flux was observed in higher frequency range after SMBI.

B. Just after SMBI during Wp degradation

In Fig. 5(c), red dot-dash line shows the spectra of Γ during the W_p degradation phase. Compared with that before SMBI, the local peak at 20-30 kHz, which was observed before SMBI, disappeared. The local spectra peaks of $\tilde{I}_s / \langle I_s \rangle$ and \tilde{E}_θ at 20-30 kHz also disappeared. This means the coherent mode, which contributes to the significant fluctuation-induced transport before SMBI, was suppressed by SMBI. Although the coherent mode of 20-30 kHz had been suppressed, Γ was greatly enhanced in the low frequency range (below 40 kHz), as shown in Fig. 5(c). Temporal traces of $\tilde{I}_s, \tilde{E}_\theta$ and Γ in the frequency range of 10-70 kHz are shown in Fig. 7. Here, the trace of $\tilde{I}_s, \tilde{E}_\theta$ and Γ are calculated using eqs. (3), (4) and (5) respectively. It is quite clear that Γ dramatically increased for 3-4 ms after SMBI. In this short time window, although \tilde{E}_θ is decreasing (Fig. 7(b)) possibly due to the suppression of 20-30 kHz mode, \tilde{I}_s is significantly enhanced (Fig. 7(a)), synchronized with the increase of Γ . The enhancement of \tilde{I}_s could also be recognized from the raw signal of I_s in Fig. 8(a).

Fig. 8(b) shows the wavelet power spectrogram of I_s . The wavelet analysis¹⁶ is a powerful tool to look into the non-stationary intermittent structures in fluctuation data. Before SMBI, spectra of most structures are at 20-30 kHz corresponding to the local peak, while in the W_p degradation window, the structures have wide spectra at 10-50kHz. Skewness is a measure of the PDF (Probability Density Function) asymmetry. Positive skewness of density means that the fluctuation has more high-density bursts than low-density bursts. As shown in Fig. 8(c), the skewness of I_s increased from ~ 0.3 to ~ 0.8 just after SMBI and the shape of the PDF changes from a nearly Gaussian one to positively skewed one (Fig. 9). Conditional Average^{17,18} results of $\tilde{I}_s / \langle I_s \rangle$ in Fig. 10 shows that both the height and the span of the

CHAPTER 4 Effect of SMBI on edge fluctuation and particle transport in Heliotron J

bursts just after SMBI are increased. All these information described above reflects that the fluctuation state transformed from a coherent-mode-featured and Gaussian one to an intermittent and non-Gaussian one in this phase.

C. Long after SMBI during W_p climbing

In Fig. 4, blue solid lines show the spectra during the W_p climbing phase. Compared with the W_p degrading phase, Γ in the low-frequency range is much reduced (Fig. 4(c)). By checking Fig. 5(a) and (b), we found the reduction of $\tilde{I}_s / \langle I_s \rangle$ is the main reason of the reduction of Γ . In Fig. 6(c), the skewness is gradually decreasing in W_p climbing phase. In Fig. 7, the shape of PDF is transforming back to a Gaussian one. And also in Fig. 8, both the height and the span of the bursts are decreased. These mean the fluctuation level and the intermittency is decreasing in W_p climbing phase.

4.5 Discussion

The effect of neutrals to the edge fluctuation and confinement has been reported in refs.19, 20. In these references, increase of I_s fluctuation and decrease of W_p during traditional gas puffing are observed. The response of edge fluctuation and W_p in Heliotron J just after SMBI seems to be very similar. It is expected that, just after the gas injection (whether traditional gas-puff or SMBI), the convective heat loss is enhanced due to the increased fluctuation, while the power input to the plasma is still constant, thus leading to the decrease of W_p in addition to the effects of temporal edge temperature drop due to SMBI. However, normal gas-puff is usually continuously injected, for a long period. SMB is injected only in a short pulse. The period of this negative effect to plasma might be much stronger, but very short in SMBI case. In this studied discharge, W_p degradation window is only ~4ms (223-227ms), which is much shorter than normal gas-puff, usually of several tens of milliseconds.

In Fig. 7 (c), it is interesting to notice that in W_p climbing phase Γ is almost the same or a little smaller than before SMBI. Considering the quickly increasing plasma density, which is about a factor of two, the particle transport is much reduced. This could be explained by the better particle confinement due to density profile peaking after SMBI [6]. The reduced particle flux also improves the energy confinement.

It has to be noticed that we have used the floating potential V_f instead of the plasma spatial potential V_s . That means if the electron temperature fluctuation is significant, the measurement will contain large error. This still needs further confirmation.

4.6 Summary

The electrostatic fluctuation at the last closed flux surface (LCFS) is studied to understand the effect of SMBI to the confinement in Heliotron J. After SMBI, W_p temporarily decreased then started to climb after SMBI. The degradation of W_p is partially caused by the dramatic increase of I_s fluctuation. The statistical characteristic of I_s fluctuation changed from a nearly Gaussian state before SMBI to a non-Gaussian and intermittent one just after SMBI, and the fluctuation level is increased in the low frequency range. However W_p degradation window is very short due to the short injection period of SMBI. Second, the fluctuation

CHAPTER 4 Effect of SMBI on edge fluctuation and particle transport in Heliotron J

induced particle transport was reduced long after SMBI, suggesting better particle confinement in W_p climbing phase. We expect the short effect period of gas injection to the edge fluctuation might be an advantage of this novel fueling technique.

CHAPTER 4 Effect of SMBI on edge fluctuation and particle transport in Heliotron J

References

- ¹ L. Yao, *New Developments in Nuclear Fusion Research* (Nova Science Publishers, 2006) pp 61-87.
- ² D. L. Yu, *et al*, *Nucl. Fusion*, **50**, 035009, (2010).
- ³ D. L. Yu, *et al*, *Nucl. Fusion*, **52**, 082001, (2012).
- ⁴ T. Mizuuchi *et al.*, *Contrib. Plasma Phys.* **50**, 639 (2010)
- ⁵ T. Mizuuchi *et al.*, *Journal of Nuclear Materials*, **415**, S443-S446 (2011).
- ⁶ K. Mukai *et al.*, *Plasma and Fusion Research*, **6**, 1402111 (2011).
- ⁷ C. M. Surko and R. E. Slusher, *Science*, **221**, 817–22 (1983).
- ⁸ Liewer P. C., *Nucl. Fusion*, **25**, 1281(1985).
- ⁹ Wootton A.J. *et al*, *Phys. Fluids B*, **2**, 2879 (1990).
- ¹⁰ T. Mizuuchi *et al.*, *Journal of Nuclear Materials*, **3**, 192-196 (2000).
- ¹¹ T. Obiki *et al.*, *Nucl. Fusion* **41**, 833 (2001).
- ¹² T. Mizuuchi, *et al.*, *Journal of Nuclear Materials*, **332-336**, 337-339 (2005).
- ¹³ T. Mizuuchi, *et al.*, *Journal of Nuclear Materials*, **428-431**, 390-391 (2009).
- ¹⁴ E.J. Powers, *Nucl. Fusion* **14**, 749 (1974).
- ¹⁵ T. Mizuuchi *et al.*, *J. Plasma Fusion Res. SERIES*, **3**, 192-196 (2000).
- ¹⁶ D. E. Newland, *An Introduction to Random Vibrations, Spectral and Wavelet Analysis* (Longman Scientific & Technical, New York, 1993).
- ¹⁷ Y. M. Yuan, *et al.*, *Phys. Fluids*, **6**, 2038 (1994).
- ¹⁸ A. V. Filippas, *et al.*, *Phys. Plasmas*, **2** 839. 1(1995).
- ¹⁹ C. Hidalgo, *et al*, *Phys. Rev. Lett*, **71**, 3127 (1993).
- ²⁰ C. Hidalgo, *et al*, *Phys. Plasmas* **2**, 1(1994).

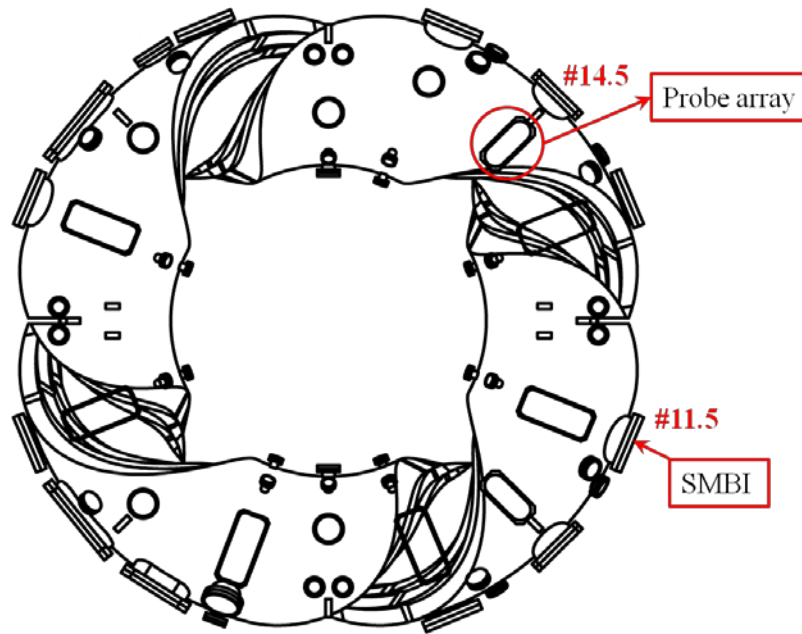


Fig.1 A schematic top-view of Heliotron J. The probe cluster is installed at the top port at #14.5 and SMBI nozzle is installed at #11.5.

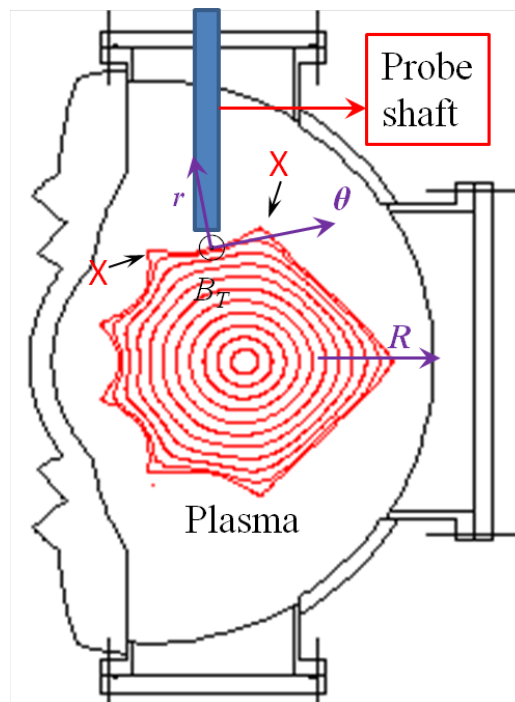


Fig. 2 #14.5 poloidal cross section: “X” is the X-point of this magnetic configuration in vacuum condition. “r” and “θ” are the radial and azimuthal direction of the plasma column, respectively. “R” is the radial direction of torus. B_T is the magnetic field direction;

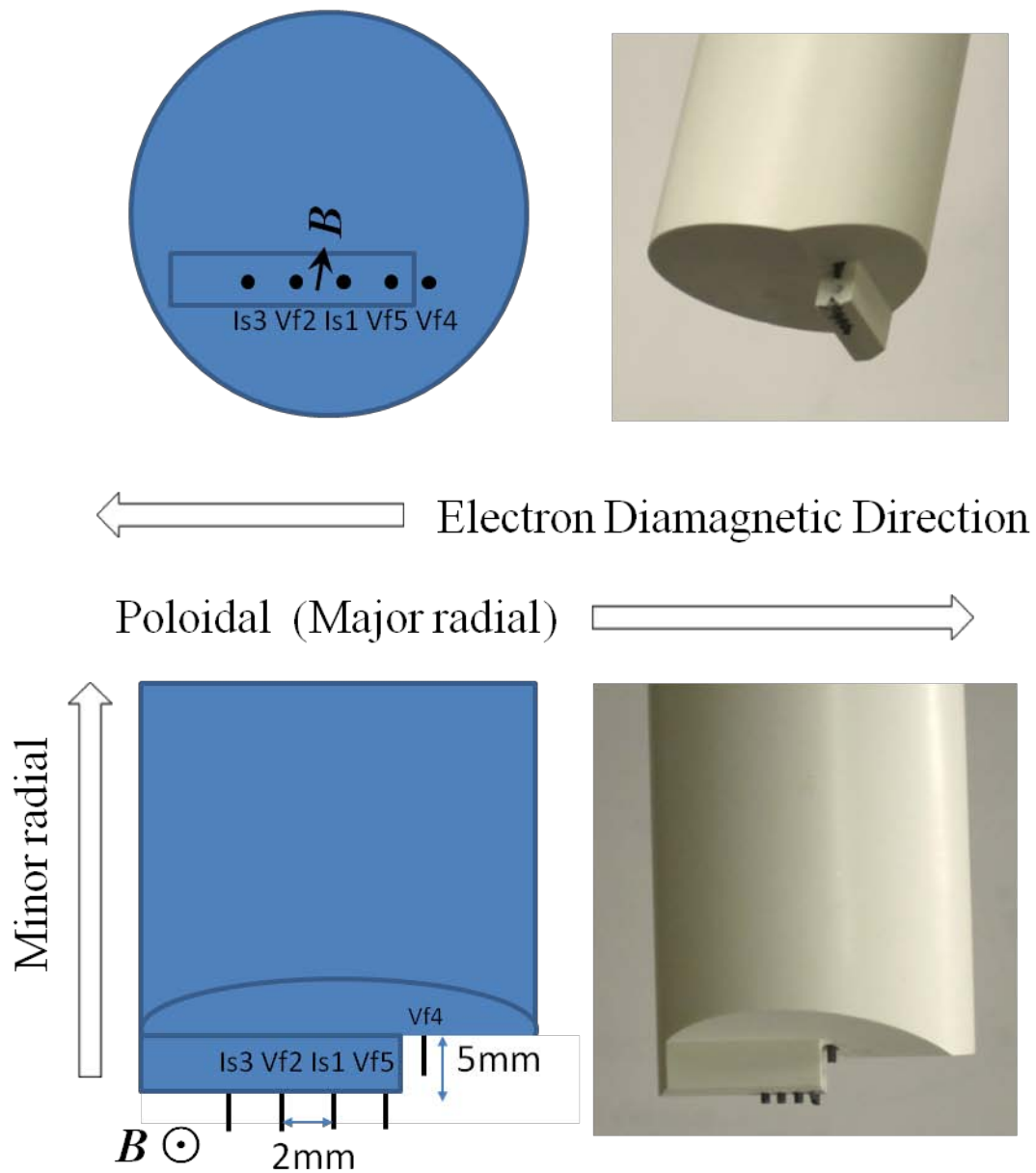


Fig. 3 Structure of the Langmuir probe array: I_s is the ion saturation current signal. V_f is the floating potential.

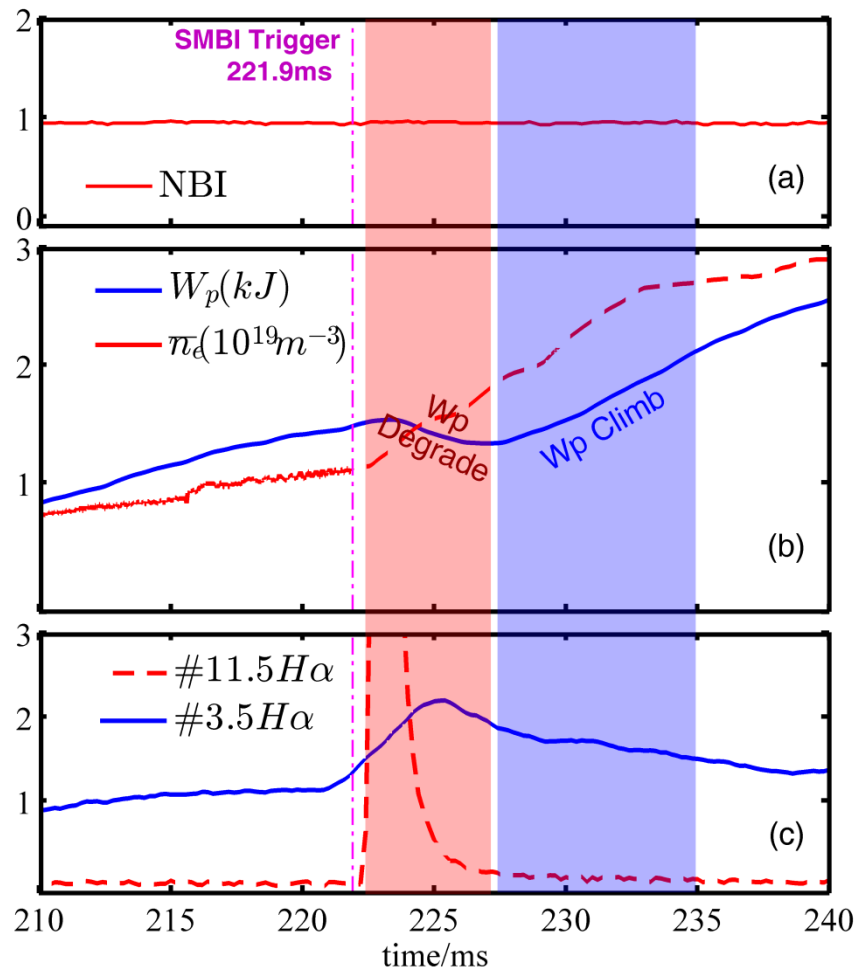


Fig.4 Main plasma parameters: (a) NBI is the timing signal of Neutral Beam heating. (b) \bar{n}_e \bar{n}_e is the line-averaged electron density; W_p is the plasma stored energy measured with a diamagnetic loop; (c) #11.5 H α and #3.5 H α are the signal of H α ray detector at #11.5 and #3.5 sections, respectively. A Purple line indicates the timing of SMB injection timing; A time span labeled by pink shadow is the period “just after SMBI” where W_p was degrading; The blue shadow labels the period long after SMBI when W_p was climbing.

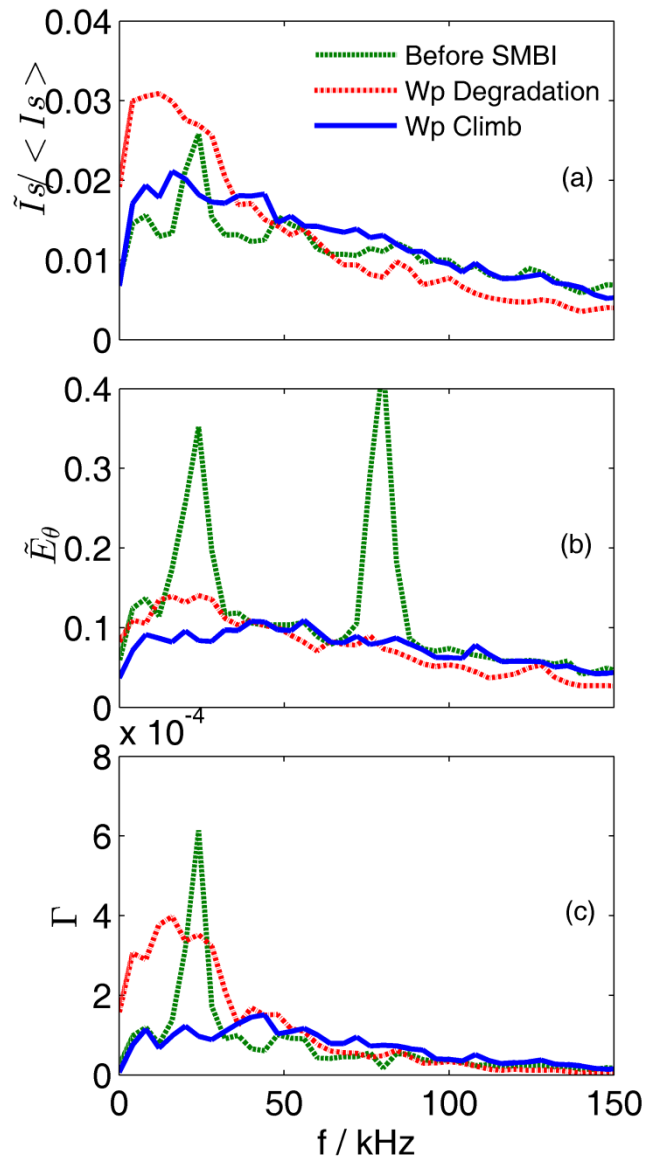


Fig.5 Spectra at LCFS: (a) Amplitude spectrum of $\tilde{I}_s / \langle I_s \rangle$ (b) Amplitude spectrum of \tilde{E}_θ (c) spectrum of particle flux. The three line types indicate different time phases: green dash line - before SMBI phase, 227-221ms; red dot-dash line - W_p degradation phase, 223-227ms; blue solid line - W_p climbing phase, 230-234ms.

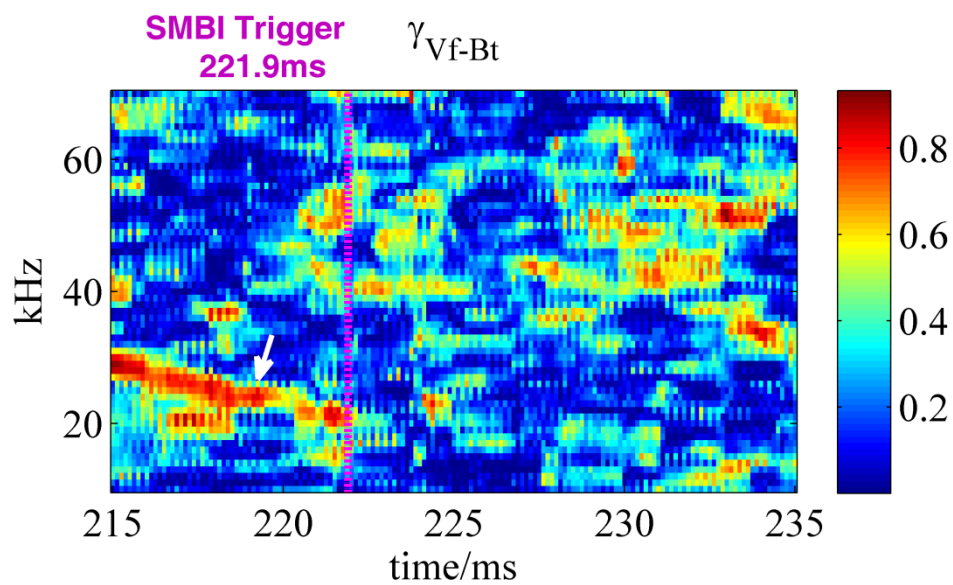


Fig.6 Coherence diagram between V_f and B_t . The white arrow labels the high coherence before SMBI at 20-30kHz.

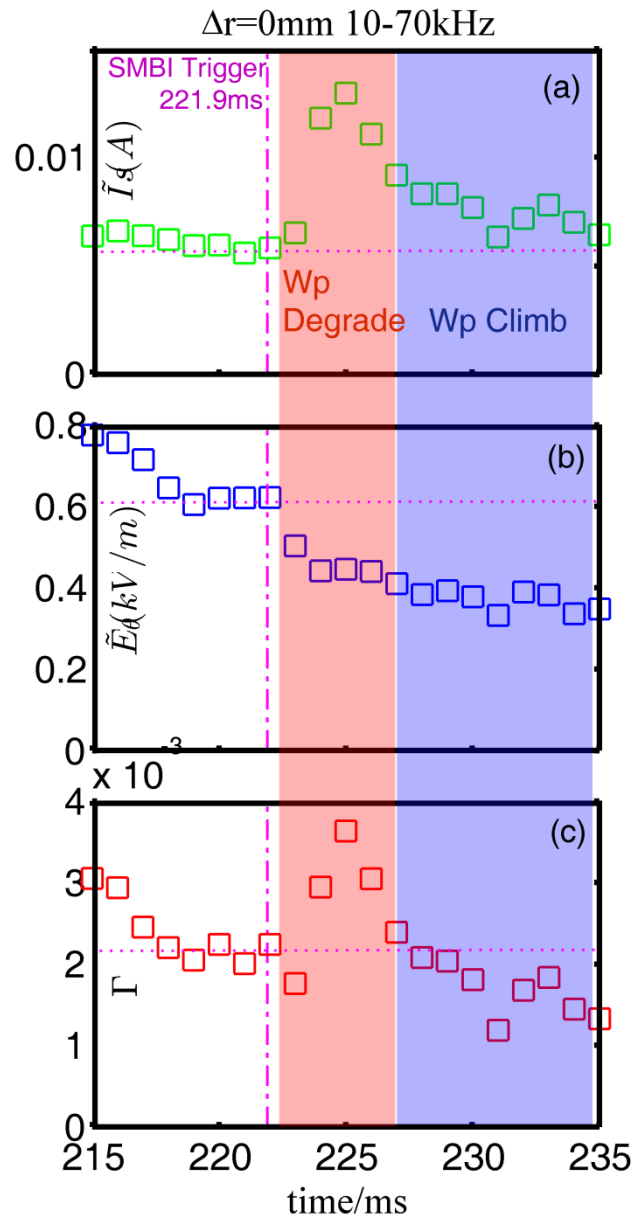


Fig.7 (a)Integrated I_s fluctuation, (b) integrated \tilde{E}_θ fluctuation, and (c)fluctuation induced particle flux in 10-70kHz at LCFS.

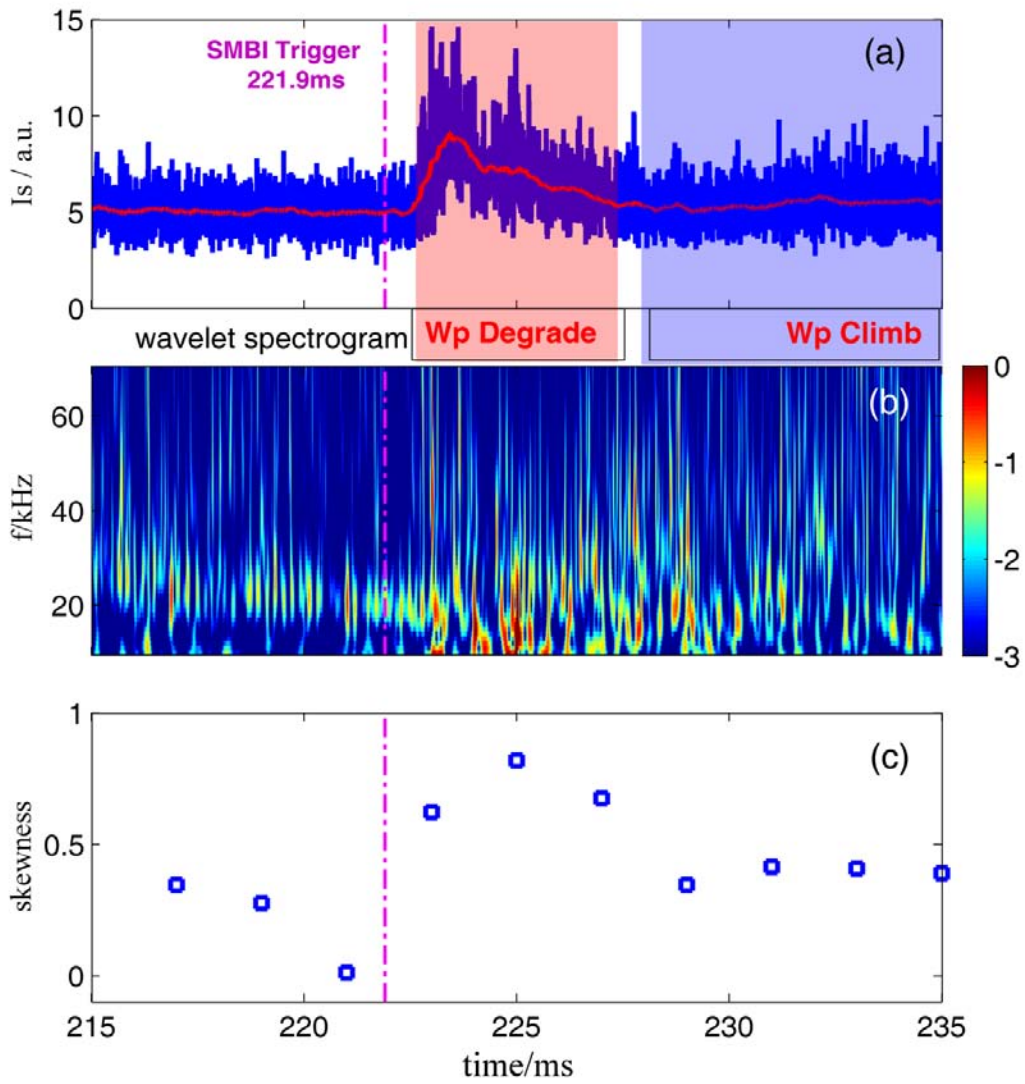


Fig.8 (a) raw signal (blue line) I_s and its time-averaged value (red line) $\langle I_s \rangle$; (b) wavelet power spectrogram of $\tilde{I}_s / \langle I_s \rangle$; (c) skewness of I_s .

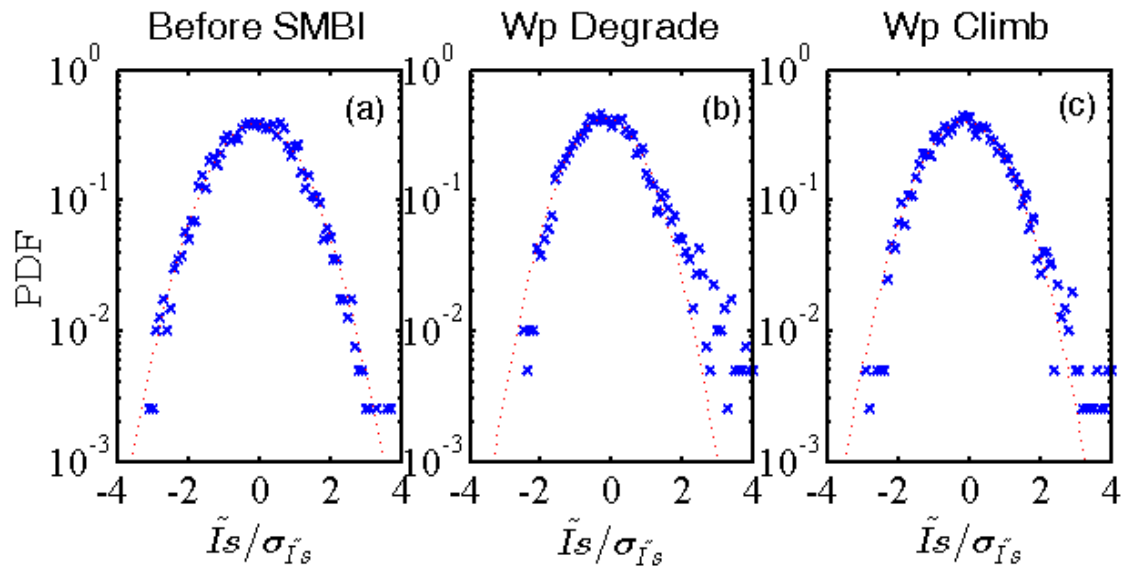


Fig. 9 Blue cross markers stand for the PDF (Probability Density Function) of $\tilde{I}_s/\sigma_{\tilde{I}_s}$ on LCFS in the three phases, from left to right: before SMBI phase; W_p Degradation phase; W_p climb phase. $\sigma_{\tilde{I}_s}$ is the standard deviation of \tilde{I}_s . The red dot lines are the best Gaussian fitting for the cross markers.

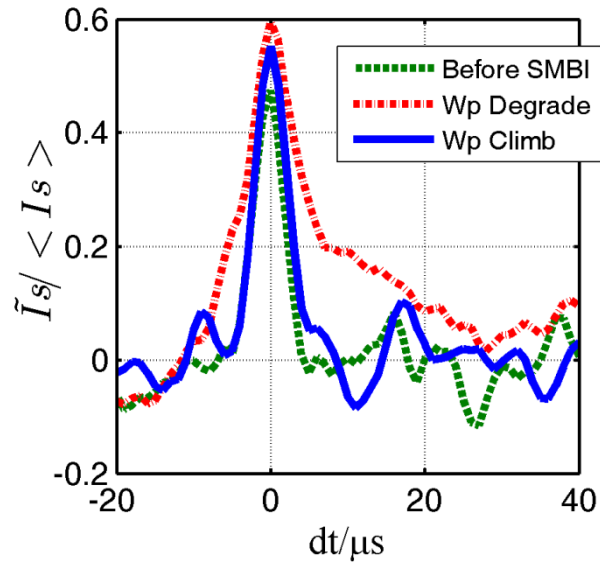


Fig. 10 Conditional Average results of $\tilde{I}_s / \langle I_s \rangle$ on LCFS in the three phases. Green dash line - before SMBI phase; red dash-dot line - W_p Degradation phase; blue solid line - W_p climb phase. The threshold of the condition is set to $2\sigma_{\tilde{I}_s}$.

Chapter 5. Observation of edge filamentary structure motion during supersonic molecular-beam injection using a fast camera in Heliotron J

A perpendicular-view fast video camera has been installed in Heliotron J to observe the behavior of filamentary structures of edge plasma turbulence across the last closed flux surface (LCFS). Supersonic molecular-beam injection (SMBI) can greatly increase the edge H_α emission; hence, we used the high imaging rate and shutter speed of the camera to capture the behavior of the fast propagating filamentary structures. A high-pass fast Fourier transform filter on the time dimension was adopted to extract the fluctuation component from the raw data for each pixel. The motion of the filamentary structures was clearly visible when we applied an amplitude threshold to identify the intense structures. In addition, a time-resolved 2D cross-correlation technique was adopted to estimate the poloidal phase velocity of turbulence. The motion direction was found to be reversed dramatically just after an SMBI pulse.

5.1 Introduction

A video camera can provide 2D images of turbulence structures by recording $H\alpha/D\alpha$ emissions. The intensity S_α of the $H\alpha/D\alpha$ line emission is proportional to the neutral gas density n_0 and also depends on the electron temperature T_e and electron density n_e [1, 2],

$$S_\alpha = n_0 f_3(n_e, T_e) A_{32} \quad (5.1)$$

where $f_3(n_e, T_e)$ is the ratio of the population density of $n = 3$ to the ground state, which is a nonlinear function of n_e and T_e . In the above equation, A_{32} is the radiative decay time rate of the $n = 3$ to $n = 2$ transition, where n is the principal quantum number. Using gas injection, S_α is greatly enhanced because of the increase of n_0 ; therefore, the signal-to-noise ratio of the camera image can be high enough to be useful even at a high imaging rate and shutter speed. This is the so-called “gas puff imaging (GPI)” technique [3]. The neutral density of the gas, n_0 , provided by the gas puff does not change significantly during the short fluctuation time scale ($\sim 10 \mu\text{s}$); hence, the fluctuations in S_α are due to the local evolution of the plasma or propagating plasmoids whose electrons can excite neutral atoms immediately. From the DEGAS2 simulation code and experimental results of Alcator C-Mod, in edge plasmas with $10^{13} \text{ cm}^{-3} < n_e < 10^{14} \text{ cm}^{-3}$, $D\alpha$ emission is mainly located in the region $10 \text{ eV} < T_e < 50 \text{ eV}$ [3]. In this temperature range, both n_e and T_e perturbation can cause S_α fluctuation [2]. This

CHAPTER 5. Observation of edge filamentary structure motion during SMBI using a fast camera in Heliotron J

interpretation can be somewhat simplified if the electron density and temperature fluctuations are in phase, as expected theoretically and approximately verified using Langmuir probes in DIII-D [4] and TEXT [5]. Although there is still no way to determine whether profile changes during GPI are due to density or temperature changes (or both), turbulence properties such as the coherent structure sizes and velocities are independent of the nonlinearities in $f_3(n_e, T_e)$ and can be evaluated directly from the GPI data [6].

Most of the GPI systems in use [2, 3] have a tangential view, using an inside-vacuum telescope, and observe the plasma structures in the radial–poloidal plane. The camera system used in this study has a perpendicular view. The main differences to the tangential view are that this system does not contain optical components inside vacuum, and the images are taken on the poloidal–toroidal plane.

SMBI is well known as a directional gas fueling method [7-10]. It is demonstrated to be not only an effective fueling method but also an effective edge modification technique for fusion devices [8]. Meanwhile, the high H_α emission during SMBI provides an advantage for using a fast camera. In this paper, we describe the application of a fast video camera to observe the filamentary structures near LCFS in an SMBI-fueled plasma.

5.2 Equipment Setup

Heliotron J is a medium-sized, helical-axis heliotron device ($\langle R_0 \rangle / \langle a \rangle = 1.2 \text{ m} / 0.17 \text{ m}$, $\langle B_0 \rangle \leq 1.5 \text{ T}$) with an $L = 1/M = 4$ helical coil [11, 12]. As shown in **Fig. 5. 1**, a NAC fx-k5 fast video camera has been setup at a horizontal perpendicular-view window at #11.5 port [13, 14]. The optical path of the camera system and the observation region of the plasma are illustrated in **Fig. 5. 2(a)**. The optical axis of the object lens is perpendicular to the torus. The object plane of the object lens was adjusted to be close to LCFS. An SMBI nozzle was also installed at the same port for fueling control, with the gas beam parallel to the optical axis of the object lens. Therefore, the camera signal is obtained mainly from near the outer LCFS where the gas beam is injected. A typical raw image during SMBI is shown in **Fig. 5. 2(b)**, which shows a bright spot around the beam-crossing area near LCFS. In this image, the horizontal direction indicates the toroidal direction of the torus (also the X direction in this paper) and the vertical direction indicates the poloidal direction (also the Y direction in this paper). The emission enhancement by SMBI allows the camera to be used at a frame rate of up to 168,000 fps with 32×48 pixels and a $5 \mu\text{s}$ shutter speed.

To estimate the actual pixel size, information about the radial position of the $H\alpha$ emission region was required. In this experiment, we used the approximate position of LCFS as the emission region, which is 41.66 cm from the object lens, as illustrated in **Fig. 5. 2(a)**. In other devices, such as the Alcator C-Mod, the GPI signal is mainly obtained from near the separatrix. The center of the GPI emission cloud is 5 mm outside the separatrix, where $T_e \sim 25 \text{ eV}$. The radial thickness of the emission cloud is 2–3 cm [1]. The error from the radial position estimation is small. For example, a 2 cm error in the radial position will only induce a $2/41.66 \sim 5\%$ error in pixel size. From the optical path in **Fig. 5. 2(a)**, we estimated the actual pixel size to be about 1.6 mm, which in turn yielded an image area of $51.8\text{mm} \times 77.8 \text{ mm}$.

5.3 Data Analysis and Results

Turbulence structures are observed as being “frozen” in a single image, with the shutter opening duration ($\sim 5 \mu\text{s}$) shorter than the typical fluctuation time scale ($\sim 10 \mu\text{s}$). Therefore, structure features such as size and stretch direction could be extracted from the images. If the framing rate of the camera is faster than the lifetime of the turbulent structures within the field of view, the turbulence motion can be followed and continuous images can be correlated to infer the motion velocity of turbulence. In this section, we will focus on the analysis techniques used to capture the behavior of the filamentary structures.

5.3.1 Extraction of filamentary structures

In this subsection, an example video taken of an SMBI discharge at 168,000 fps and a frame size of $51.8 \text{ mm} \times 77.8 \text{ mm}$ will be analyzed. For this discharge, the magnetic configuration was the standard one for Heliotron J and the opening duration of the SMB nozzle was $100 \mu\text{s}$. Some of the main plasma parameters in this discharge are given in **Fig. 5.3**. The sharp increase in the $\text{H}\alpha$ signal ($\#11.5\text{H}\alpha$), which is measured at the same toroidal section as SMBI, clearly shows the arrival timing ($\sim 243\text{ms}$) of the molecular beam. Both plasma density and stored energy increased after SMBI. A detailed discussion on the SMBI fueling control in Heliotron J is described in [10].

One of the raw images from this video is shown in **Fig. 5.4(a)**. From this perpendicular view, the pixel signal I_{raw} is mainly obtained from the line-integrated emission across the depth of field (DOF) around LCFS, where the $\text{H}\alpha$ emission is supposed to be intense. Moreover, I_{raw} contains both a long-time-scale component, “background” I_{bg} , from across DOF, mainly attributed to the increase and decrease in n_0 , and a short-time-scale fluctuation components, \tilde{I} , from the turbulent plasma structures [15]. Therefore, pre-processing was applied to make the filament structures more visible by removing the “background” and highlight the fluctuation components. A high-pass fast Fourier transform (FFT) filter was applied to obtain the fast component of fluctuation \tilde{I} . The cut-off frequency was set to 10 kHz in this study, which removed most of the slow components brought about by the variation in gas pressure. The “background” component is calculated as $I_{bg} = I_{raw} - \tilde{I}$. To relate the camera signal with the density fluctuation, the normalized fluctuation \tilde{I}/I_{bg} is used. If the fluctuation in T_e is smaller than and/or in phase with n_e , the image of \tilde{I}/I_{bg} is approximately proportional to the normalized density fluctuation \tilde{n}_e . (It has to be noted that \tilde{I}/I_{bg} is neither equal nor exactly proportional to \tilde{n}_e , since \tilde{I} is the line integration of the emission across the relatively small-sized turbulence structure, while I_{bg} is the line integration of the emission across the whole $\text{H}\alpha$ emission region.) The curves of I_{raw} , \tilde{I} , I_{bg} , and \tilde{I}/I_{bg} are shown in **Fig. 5.5**. **Fig. 5.4(b)** and (c) show the images of \tilde{I} and I_{bg} , respectively. In **Fig. 5.4(b)**, we can clearly recognize both positive (white) and negative (black) filamentary patterns of fluctuation. In **Fig. 4(c)**, the upper part of the background image is much brighter than the lower part because the former is around the gas injection spot, closer to the nozzle and lens.

The fluctuation data in **Fig. 5.4(b)** is filtered with an amplitude threshold to extract the more intense density fluctuation structures [16]. In this paper, the amplitude threshold for each point is set to 1σ , where $\sigma(X,Y)$ is the normalized standard deviation (STD) of \tilde{I}/I_{bg} at a pixel point (X,Y) during the sliding time window of $100 \mu\text{s}$. The blue line in **Fig. 4(e)** shows \tilde{I}

CHAPTER 5. Observation of edge filamentary structure motion during SMBI using a fast camera in Heliotron J

I_{bg} along a poloidal line at $X = 16$ illustrated in **Fig. 5. 4** (a). The positive threshold (red line) indicates the density-peaking structures, such as a “blob” or the crest of an intense wave. The negative threshold (black line) indicates the density-hollow structures like a “hole” or the trough of an intense wave. We can identify a density-hollow structure, as illustrated in region (1), and a peaking structure, as illustrated in (2). If we define the width of the shadowed region in the figure as that of the structure, the hollow structure is ~ 12 mm wide and the peaking structure is ~ 17 mm wide. **Fig. 5. 4** (d) is updated from **Fig. 5. 4**(b) using the amplitude threshold, where the white color indicates a fluctuation larger than σ , black indicates a fluctuation less than $-\sigma$, and red indicates a fluctuation between $-\sigma$ and σ .

5.3.2 Poloidal velocity estimation

Some continuous images of filamentary structures recorded during SMBI in shot No. 44946 are shown in **Fig. 5. 6** (a)–(d). In these figures, upward is in the electron diamagnetic direction (De). From these images, the velocity can be readily estimated. Taking **Fig. 5. 6** (a) as an example, five continuous frames (243.089–243.119 ms) recorded just after the SMB’s arrival are shown. The filament indicated by the arrow travelled approximately 48 pixels in the poloidal direction during this time span. Considering the real size per pixel, ~ 1.6 mm, we calculated the poloidal velocity, $v_{\theta f} = 48 \times 1.6 / (243.119 - 243.089) = 2.5 \times 10^3$ m/s. The propagating direction is downward, which is the ion diamagnetic direction (Di). In these images, it is interesting to note that, during the time span in which I_{raw} is still enhanced by SMBI, the filamentary structure’s velocity changes to the De direction, as shown in **Fig. 5. 6** (b). After SMBI, in **Fig. 5. 6** (c) and (d), the structure’s motion returns to the Di direction, and the velocity slows down to about 1 km/s.

To get the overview of the filament motions, **Fig. 5. 7** shows the Y-time contour of \tilde{I}_{bg} along the $x = 25.9$ mm mid-line. In this figure a continuous contour usually stands for the same filament, e.g., the contours labeled by the arrows in the phases of a, b, c, d, corresponding to a, b, c, d in **Fig. 5. 6**. The tilt angle of the contour structures reversed from Di to De about 243.2ms, and reversed back to Di about 243.6ms. E.g., the propagation of filaments is clearly in Di direction in b, d, e phases, and in De direction in c phases. Compared to phase b, the smaller tilt angle in d and e means the propagation velocity is slowing down, which is inconsistent with the above results.

The method of direct observation is reliable when there is a clear structure crossing the window. However, because the field of view is very narrow, it is not always easy to entirely catch the motion of a structure. Another method is to use a cross-correlation technique to estimate the phase velocity of turbulence. The details of a time-resolved 2D cross-correlation technique for GPI data are described in ref. [17]. In shot No. 44946, we used a time window of ± 5 frames, which is $10 \times 6\mu s = 60 \mu s$, to examine the cross -correlation between the pixel data of one frame and the following frame. The lag of the cross-correlation is set from -11 to $+11$ pixels, corresponding to an actual velocity of $4.1 - 4.1$ km/s. The calculated region is limited to $19.4\text{mm} < Y < 58.3\text{mm}$ along the poloidal line at $X = 25.9\text{mm}$ in **Fig. 5. 4**(a). **Fig. 5. 8** is the estimated poloidal velocity, where the error bars indicate standard deviation and the positive direction indicates De direction. During the period 243.0–243.2 ms, the velocity is in the Di direction. Then, from 243.2 to 243.6 ms, the velocity reversed to the De direction and dropped from about 2 km/s to zero. Just after 243.6 ms, the motion direction reversed again to

CHAPTER 5. Observation of edge filamentary structure motion during SMBI using a fast camera in Heliotron J

the D_i direction, and the velocity value varied from 2 km/s to about 1 km/s. All velocity values estimated from Fig. 6 show quite good coincidence with the results shown in **Fig. 5. 7**.

5.4 Discussion

The $E \times B$ velocity shear layer (VSL) near the edge has been found in many magnetically confined fusion devices. The Langmuir probe measurement at #14.5 section of Heliotron J reveals a clear VSL, as illustrated in **Fig. 5. 9**. VSL is located between $\Delta r = 10$ and 15 mm, and does not move before or after SMBI. The turbulence motion inside VSL is in the D_e direction, and that outside VSL is in the D_i direction.

Although the reason for the direction reversal mentioned in section 3.2 is unknown at present, one speculation is that the main $H\alpha$ emission region shifts inward across VSL because of the strong cooling effect and/or the gas penetration by SMBI. The DOF of the object lens has a certain thickness; therefore, even if the emission region is shifting, it can still be in the DOF and provide a clear image on the camera sensor. This means we must be very careful with the perpendicular-view data, and try to get some radial position information of the main emission region. For this reason, combining these data with Langmuir probe data is a possible solution to this problem, which will be investigated in the future.

Note that at the SMBI arrival-timing window of 243.0–243.2 ms, the velocity estimated in both **Fig. 5. 6** (a) and **Fig. 5. 8** might be affected by the fast expansion of the gas cloud. The background emission I_{bg} in **Fig. 5. 5**, which is proportional to the fluctuation in the neutral gas density \tilde{n}_0 , increased quickly during this period. If \tilde{n}_0 varied quickly enough compared to the filter, the \tilde{I} signal we extracted may also be affected. However, after 243.2 ms, I_{bg} varies slowly, which means the component of \tilde{n}_0 will be removed from \tilde{I} by the high-pass filter.

5.5 Summary

In this paper, we reported on the edge filamentary structures observed by a perpendicular-view camera and the analysis methods used to make the results more visible. The spatial filamentary structure was extracted using a high-pass FFT filter in the time dimension. A threshold amplitude was then employed to extract intense filamentary structures. Using these images, we could directly estimate the poloidal velocity of these structures. A time-resolved 2D cross-correlation technique was also applied to estimate the structure's velocity. The results from the two methods roughly agreed. During an SMBI discharge, it was observed that the poloidal velocity of the filamentary structures reversed during the SMB injection. One possible reason for this is that the intense emission region shifted inward because of the injected gas. Therefore, further work is needed to identify the main emission region.

CHAPTER 5. Observation of edge filamentary structure motion during SMBI using a fast camera in Heliotron J

References

- [1] S. J. Zweben and D. P. Stotler *et al.*, Phys. Plasmas **9**, 1981 (2002).
- [2] D. P. Stotler *et al.*, Journal of Nuclear Materials **313-316**, 1066-1070 (2003).
- [3] S. J. Zweben *et al.*, Nucl Fusion **44**, 134 (2004).
- [4] D. L. Rudakov *et al.*, Plasma Phys. Control. Fusion **44**, 717 (2002).
- [5] M. A. Meier *et al.*, Phys. Rev. Lett. **87**, 500 (2001).
- [6] S. J. Zweben *et al.*, Phys. Plasmas **17**, 102502 (2010).
- [7] L. Yao, *New Developments in Nuclear Fusion Research* (Nova Science Publishers, 2006) pp 61-87.
- [8] L. Yao and J. Baldzuhn, Plasma Sci. Tech. **5**, 1933 (2003).
- [9] T. Mizuuchi *et al.*, Contrib. Plasma Phys. **50**, 639-645 (2010).
- [10] T. Mizuuchi *et al.*, Journal of Nuclear Materials **415**, S443-S446 (2011).
- [11] F. Sano *et al.*, J. Plasma Fusion Res. Ser. **3**, 26 (2000).
- [12] T. Obiki *et al.*, Nucl. Fusion **41**, 833 (2011).
- [13] N. Nishino *et al.*, Journal of Nuclear Materials **363-365**, 628-632 (2007).
- [14] L. Zang *et al.*, Plasma Science and Technology **15**, 213-216 (2013).
- [15] B. D.udson *et al.*, Plasma Phys. Control. Fusion **50**, 124012 (2008).
- [16] T. Windisch *et al.*, PPPL Reports 4371 (2008).
- [17] S. J. Zweben *et al.*, Plasma Phys. Control. Fusion **54**, 025008 (2012).

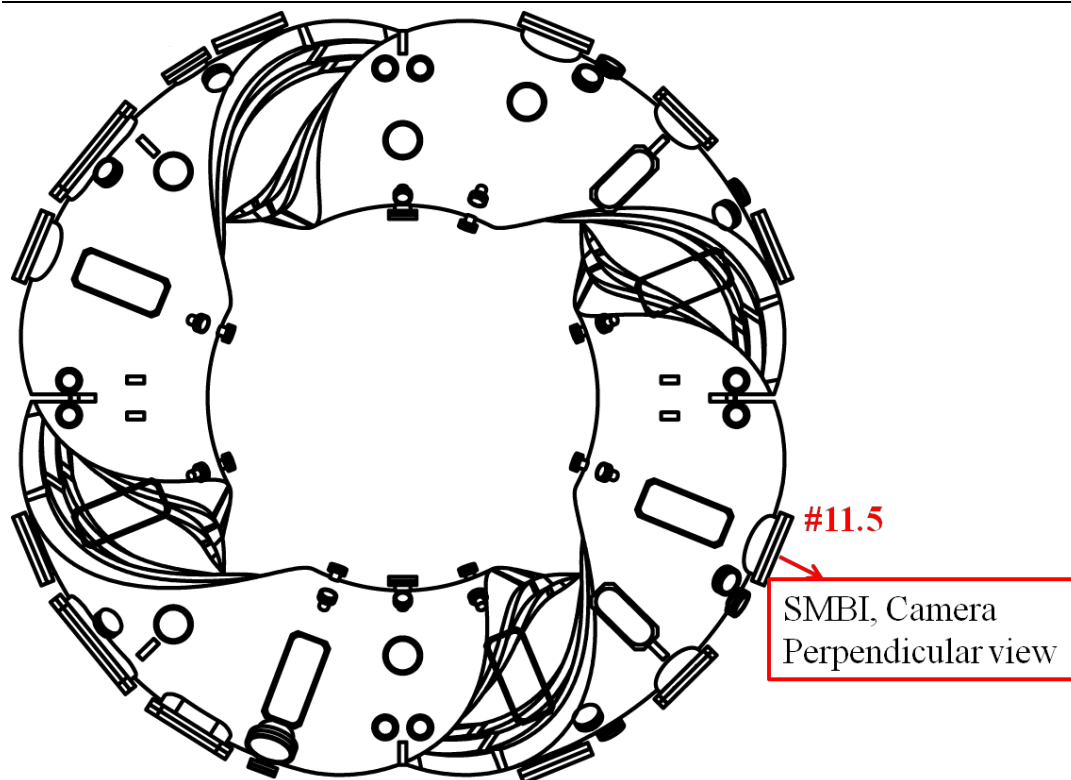


Fig. 5. 1 Top view of Heliotron J showing the toroidal positions of #11.5 SMBI and the fast camera.

CHAPTER 5. Observation of edge filamentary structure motion during SMBI using a fast camera in Heliotron J

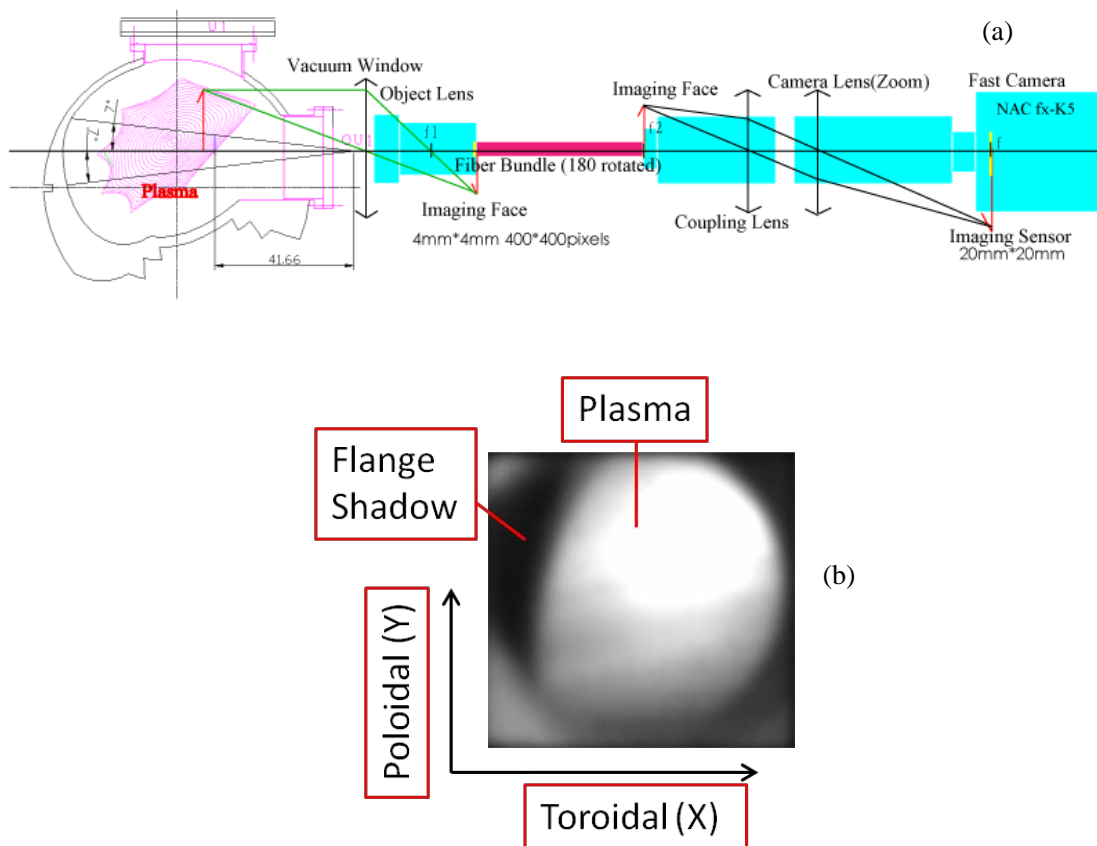


Fig. 5. 2 (a) Optical path of the fast camera at #11.5; (b) raw image from the #11.5 during SMBI (at 80,000 fps).

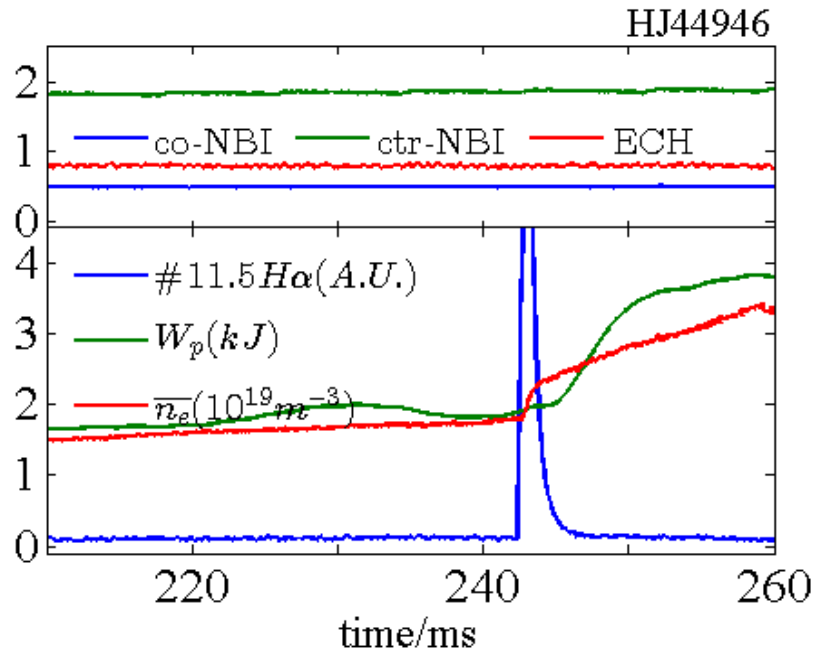


Fig. 5. 3 Plasma parameters for Shot No. 44946, where n_e is the linear-average electron density, W_p is the diamagnetic energy, #11.5 $H\alpha$ is the signal from the $H\alpha$ ray detector at the #11.5 section.

CHAPTER 5. Observation of edge filamentary structure motion during SMBI using a fast camera in Heliotron J

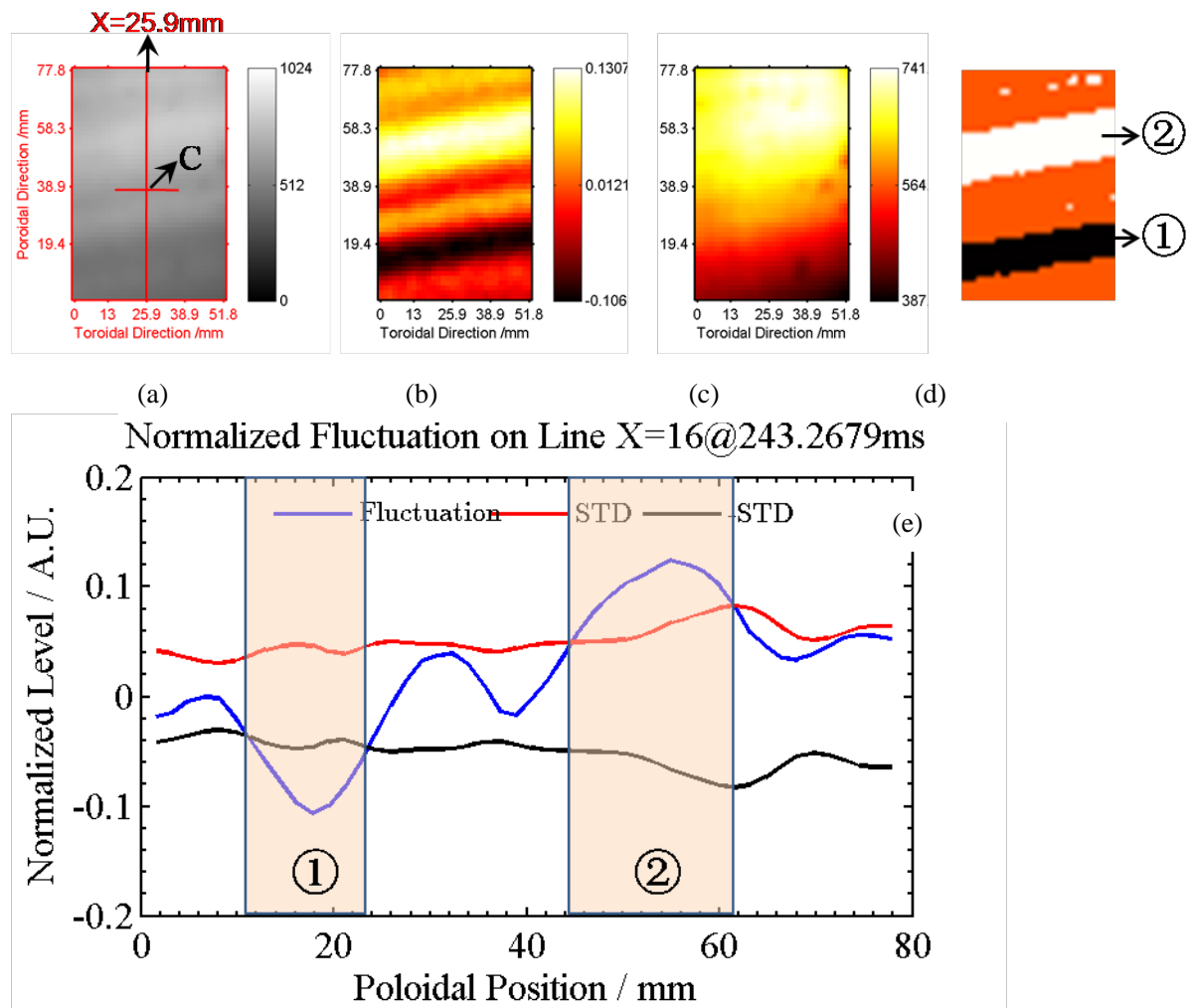


Fig. 5. 4 Images from shot No. 44946. The imaging speed is 168,000 fps.

- (a) A raw image. Positions of mid-line $x = 25.9$ mm and center point C (25.9 mm, 38.9 mm) are labeled. The directions of the X-axis and Y-axis are the same as shown in Fig. 2(b).
- (b) A normalized fluctuation (\tilde{I}/I_{bg}) image.
- (c) A background image.
- (d) An updated image with amplitude threshold.
- (e) The normalized fluctuation signal along the mid-line (blue), positive (red), and negative (black) standard deviation during the time window. Negative and positive fluctuation regions (1) and (2) correspond to the density peak structure and hollow structure in (d), respectively.

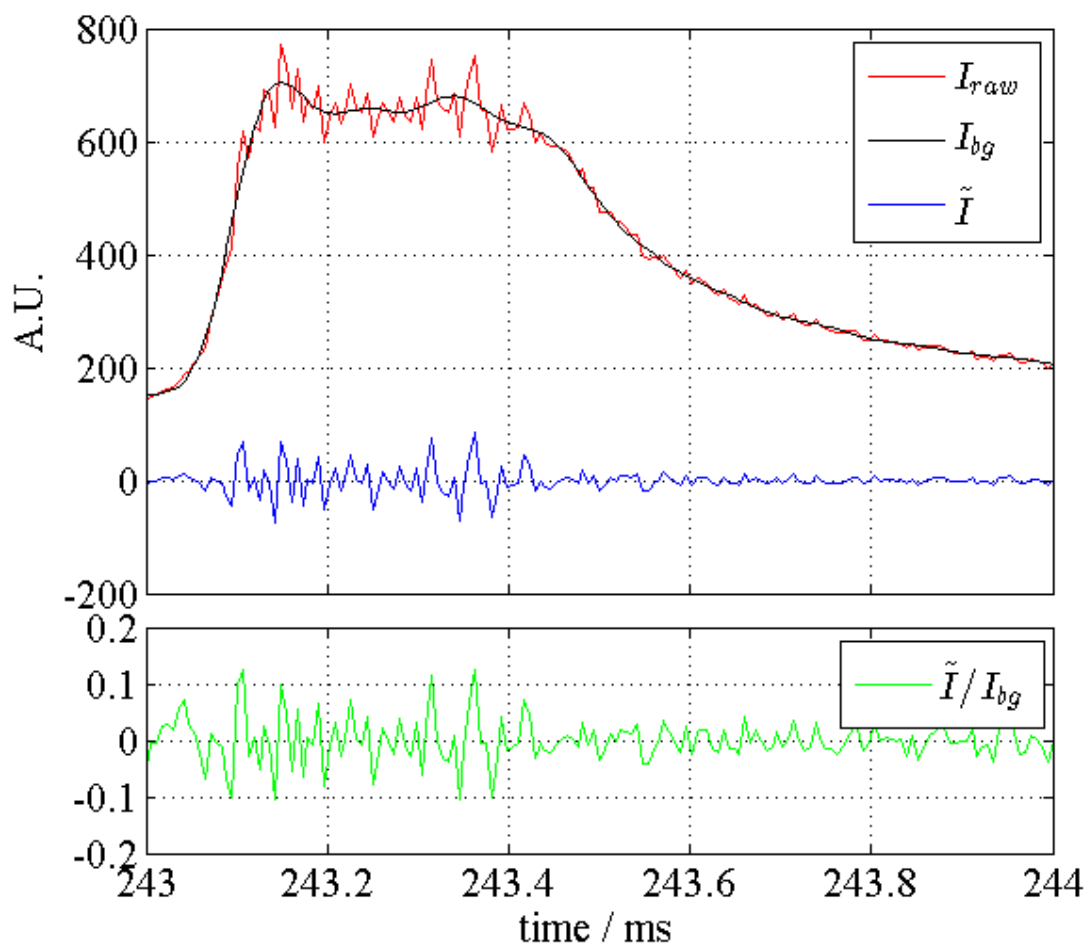


Fig. 5. 5 Data at point C. Red line indicates the camera's raw signal. Blue line indicates the filtered-out fluctuation signal. Black line indicates the background signal. Green line indicates the normalized fluctuation signal of the background.

CHAPTER 5. Observation of edge filamentary structure motion during SMBI using a fast camera in Heliotron J

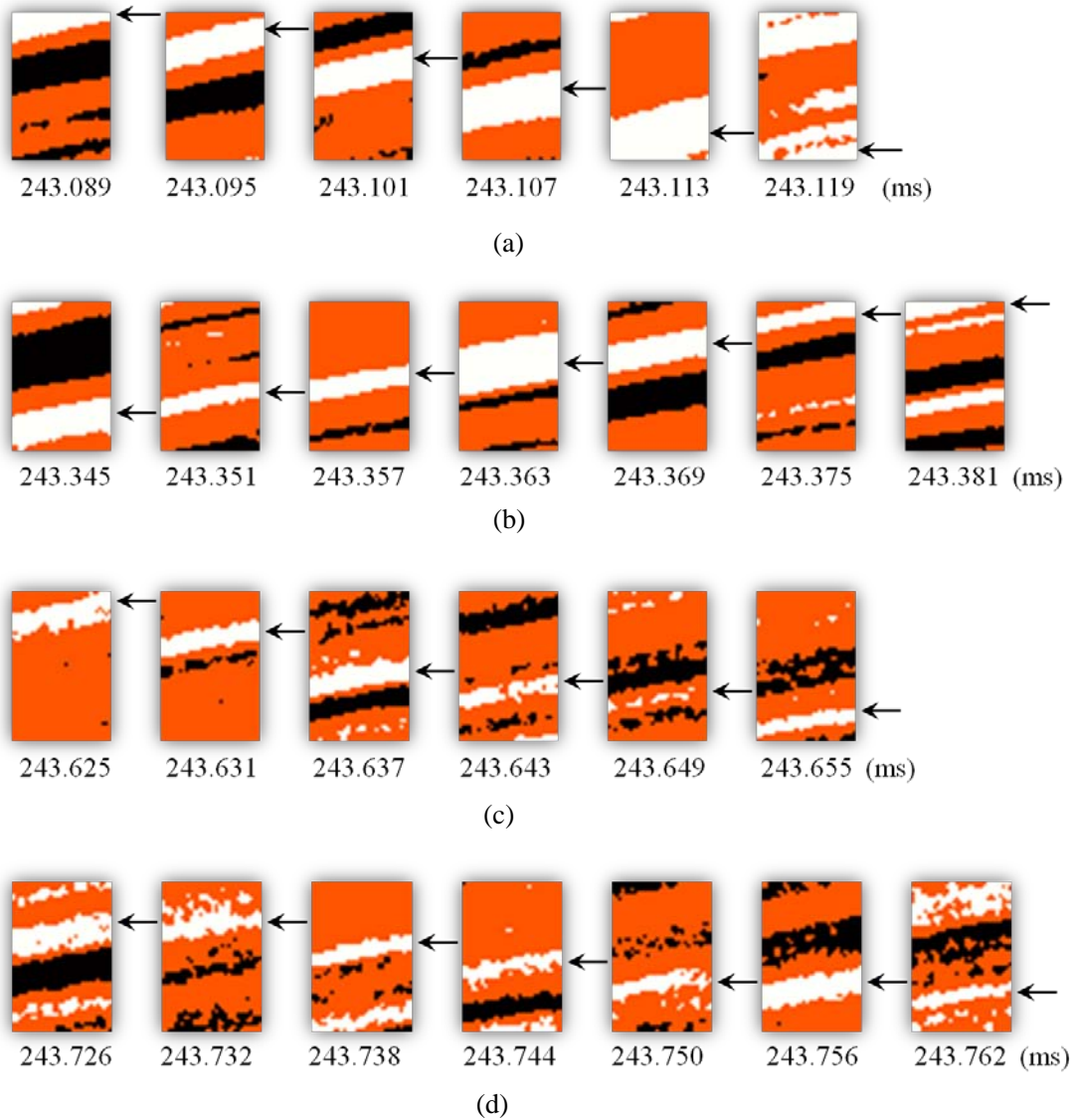


Fig. 5. 6 Updated images from shot No. 44946. (a) 243.089–243.119 ms, ~ 2.5 km/s to Di; (b) 243.345–243.381 ms, ~ 2 km/s to De; (c) 243.625–243.655 ms, ~ 2 km/s to Di; (d) 243.726–243.762 ms, ~ 1 km/s to Di; Upward is the De direction.

CHAPTER 5. Observation of edge filamentary structure motion during SMBI using a fast camera in Heliotron J

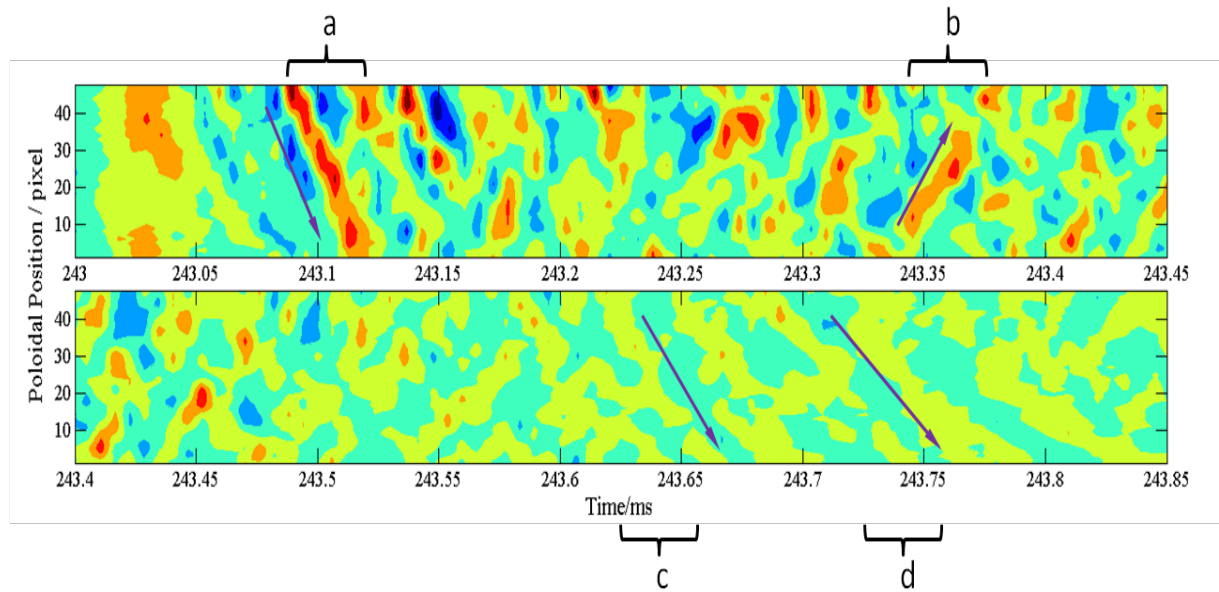


Fig. 5. 7 Y-time contour of \tilde{I}/I_{bg} along the $x = 25.9$ mm mid-line. The propagation of filaments is clearly in Di direction in b, d, e phases, and in De direction in c phases.

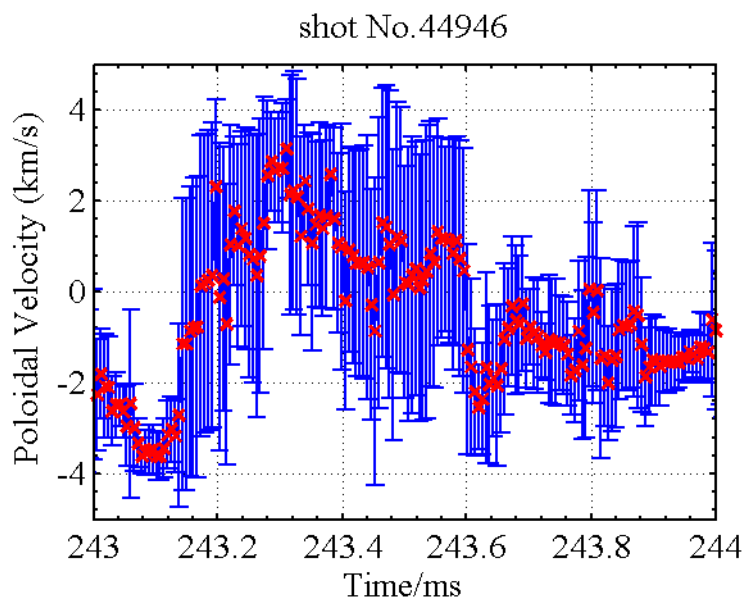


Fig. 5. 8 Poloidal velocity during SMBI. The error bar is from the standard deviation of the results along the specified poloidal line, and the positive direction indicates the De direction.

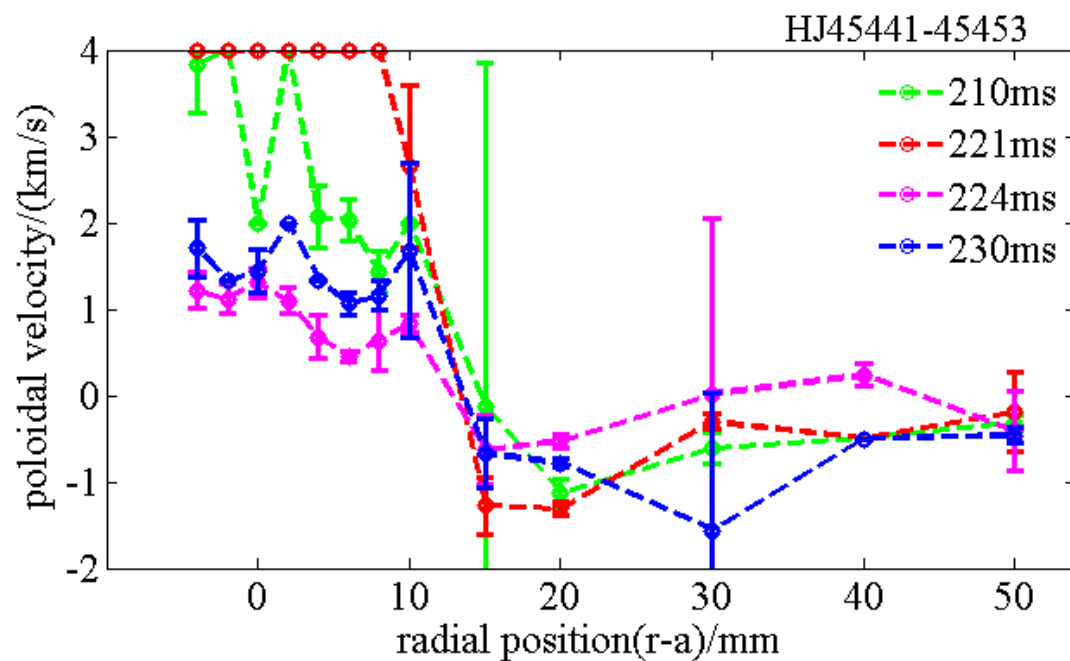


Fig. 5. 9 Turbulence phase velocity in the poloidal direction at #14.5 in Heliotron J, measured by Langmuir probe array. Green line indicates 3 ms before SMBI, and red line indicates 3 ms after SMBI. The positive direction indicates the De direction.

Chapter 6. Investigation of the edge fluctuation structures with the combination of a camera and a Langmuir probe cluster in Heliotron J

A method is proposed to estimate the radial span of a density fluctuation mode at the edge plasma observed with a vertical-view high-speed video camera, by comparing ion-saturation current from a Langmuir probe (at the same toroidal position as the camera) and the local enhanced brightness in the camera image due to the probe-plasma interaction. Large-sized (~14cm) poloidally propagating density fluctuation structures were observed for a 20-30 kHz mode using fast camera in Heliotron J. When probe was inserted to the plasma, plasma-surface interaction (PSI) was clearly observed using camera. According to the interaction intensity between the probe and the edge plasma, the radial span of the 20-30 kHz mode, which was observed by the camera, has been identified to be within 10mm outside from the last closed flux surface (LCFS). This application shows the combination of camera and probe is a powerful tool for edge fluctuation study.

6.1 Introduction

A high-speed video camera (fast camera for short) can provide 2D images of a wide area with the sampling speed of 200-300 kHz or more. Analyzing a series of plasma image data from the fast camera, fast propagating plasma turbulence structures could be resolved. The camera usually captures visible light emission from a working gas of the discharge, H α (or D α) emission in many fusion plasma experiments. The local intensity S_α of the H α (or D α) line emission is proportional to the neutral gas density n_0 and also depends on the electron density n_e and the electron temperature T_e [1, 2],

$$S_\alpha = n_0 f_3(n_e, T_e) A_{32} \quad (6.1)$$

where $f_3(n_e, T_e)$ is the ratio of the population density of $n = 3$ to that of the ground state, which is a nonlinear function of n_e and T_e , and A_{32} is the radiative decay time rate of the $n=3$ to $n=2$ transition. Here, n is the principal quantum number. With help of gas injection, S_α can be greatly enhanced due to the increase of n_0 . Therefore, so called “gas puff imaging (GPI)”

CHAPTER 6 Investigation of the edge turbulence combining a camera and a Langmuir probe cluster in Heliotron J

technique [3] can increase the signal to noise ratio of the camera image, and one can use much higher frame rate of camera.

A Langmuir probe is a traditional tool for turbulence diagnostic [4], and it can measure local plasma parameters. By biasing the probe tip to the ion saturation current region, the probe current is,

$$I_s = 0.61n_e C_s A_p e \quad (6.2)$$

where C_s is the sound speed, and A_p is the effective area of the probe tip. If the fluctuation of T_e is much smaller than the fluctuation of n_e , I_s mainly reflects the local density fluctuation.

This paper proposes a new combination analysis technique for edge plasma turbulence studies with a fast camera and a Langmuir probe set, and demonstrates the effectiveness of this technique discussing a result of such measurements in Heliotron J. Density fluctuation is measured with one ion saturation current signal from a probe cluster. Enhanced light emission due to the interaction between the plasma and the Langmuir probe cluster are measured with a fast camera. In Section 2 the hardware setup are described. Section 3 shows the experimental result and analysis. Finally, a conclusion is presented in section 4.

6.2 Experimental set-up

The Heliotron J device is a medium sized helical-axis heliotron device ($R_0 = 1.2/0.17\text{m}$, $\langle B_0 \rangle \leq 1.5\text{T}$) with an $L = 1/M = 4$ helical coil [5]. A top view of the torus vacuum chamber is illustrated in Fig. 1. The details of magnetic configuration of Heliotron J are reported in refs. [6, 7].

In the previous studies in Heliotron J, edge plasma behavior has been investigated using Langmuir probes [8, 9] or fast camera [10, 11, 12, 13, 14], separately. Recently, setting a Langmuir cluster and a fast camera at the same toroidal position, simultaneous measurements of these two methods have been started to investigate the edge fluctuation. The first experiment revealed basic consistency of fluctuation information in power spectra between the ion saturation current signal and pixel data from the camera images [15].

In this study, we focus on the boundary fluctuation at an O-point (a position between two adjacent X-points) at #14.5 toroidal section (Fig. 1). A Langmuir probe cluster was vertically inserted from the top of this section as shown in Fig. 2(a), and the vertical position of the probe can be scanned by shot-by-shot basis. Structure of the probe cluster is shown in Fig. 2(b). The five Langmuir probe tips are aligned along poloidal direction of the plasma. Signal names of the tips are also labeled in the figure, in which I_s and V_f stand for the ion saturation current and the floating potential, respectively.

A fast camera is set at the bottom port (Fig. 2(a)). The camera image is focused near the upper LCFS, as marked by a yellow rectangle in Fig. 2(a). The GPI system also installed near the Langmuir probe set from the upper port. The information of the video is mainly from the yellow rectangle region, because of the focusing point and significantly enhanced $H\alpha$ emission due to the gas-injection from the GPI system. A typical raw image of the video is shown in Fig. 3. The shape of the probe shaft and a bright point of one of the probe tips are

CHAPTER 6 Investigation of the edge turbulence combining a camera and a Langmuir probe cluster in Heliotron J

clearly observed. The green “+” point near the tips is selected for the following analysis. This point is chosen so that it is on the same magnetic field line with I_{s1} .

The experiment was performed in a discharge set with a fixed discharge condition. For this discharge set, the probe position was scanned from $\Delta r = -4\text{mm}$ to $\Delta r = 30\text{mm}$, where Δr is the distance between the probe tips to the LCFS, and $\Delta r < 0$ means the probe is positioned inside the LCFS. Typical plasma parameters of this discharge set are shown in Fig. 4. The plasma was sustained only by NBI heating.

6.3 Result analysis and discussion

6.3.1 Dynamics of the fluctuation structures in camera image

The power spectrogram and the power spectrum density during 215-220ms for the intensity of pixel “+” in Fig.3 are illustrated in Fig.5 (a) and (b), respectively. A density fluctuation mode was clearly observed at 20-30kHz.

A frame sequence of 20-30 kHz band-pass fluctuation images was shown in Fig.6. These images have been normalized with the time-averaged background signal. In this image sequence, a filamentary structure with the density peaking at the black arrows, was propagating poloidally across the camera view in the ion diamagnetic direction (from left to right). From the propagation of the black arrows, phase velocity of this density mode is estimated to be $V_{ph} \approx 3.6\text{ km/s}$. Then the wave number is estimated to (assuming the frequency is 25 kHz),

$$\frac{k}{2\pi} = \frac{f}{V_{ph}} = \frac{25\text{kHz}}{3.6\text{km/s}} = 6.9/m \quad (6.3)$$

6.3.2 Identification of the radial span of the turbulence structure in camera image

In Fig.6, the probe tips are located at $\Delta r = 20\text{mm}$. In this case, the observed structures are basically unperturbed from PSI effect, which means there still some distance between the mode structures and the probe tips.

To locate the edge of the density mode described in 6.3.1, in Fig. 7, we have picked the typical frames of the 20-30kHz band-pass fluctuation image, with the probe at three different locations $\Delta r = 20\text{ mm}$, 10 mm and 0 mm . At $\Delta r = 20\text{ mm}$, the filamentary fluctuation structure is like “safely” passing the probe tips without any PSI perturbation. At $\Delta r = 10\text{ mm}$, the structure is “emphasized” nearby the probe tips when it is passing by, because the PSI intensity is reflecting the local density fluctuation (see the appendix). At $\Delta r = 0\text{ mm}$, the “emphasis” effect is much stronger than $\Delta r = 10\text{ mm}$ case, suggesting greater PSI effect when the probe is inserted deeper. This means the probe tips start “touching” with the mode structures from about $\Delta r = 10\text{mm}$. Therefore, the outmost edge of the observed mode structure is located at $\Delta r \sim 10\text{ mm}$.

To verify our analysis, we compared the power spectrogram of ion saturation current signal I_{s1} at these three positions, as shown in Fig. 8. The peak of 20-30 kHz is observed from $\Delta r = 10\text{mm}$, which means the observable $\text{H}\alpha$ emission region is not less than $\Delta r = 10\text{mm}$, and the measurements of camera and probe are verified by each other. The technique

CHAPTER 6 Investigation of the edge turbulence combining a camera and a Langmuir probe cluster in Heliotron J

proposed in this paper can be, however, used in the intermittent fluctuation, where a clear peak of power spectrum is not present. This will be test for post-SMBI case.

Fig. 9 is the $\langle I_s \rangle$ (time averaged I_s) profile, which is a proxy of density profile. Slope foot of this profile is at $\Delta r = 15\sim 20\text{mm}$. This means the density mode is limited at the high density region.

6.4 Summary

A method is proposed to estimate the radial span of a density fluctuation mode at the edge plasma observed with a vertical-view high-speed video camera, by comparing ion-saturation current from a Langmuir probe (at the same toroidal position as the camera) and the local enhanced brightness in the camera image due to the probe-plasma interaction. According to the interaction intensity between the probe and the edge plasma, the radial span of the 20-30 kHz mode, which was observed by the camera, has been identified to be within 10mm outside from the last closed flux surface (LCFS). This application shows the combination of camera and probe is a powerful tool for edge fluctuation study.

Appendix. Plasma-surface interaction effect on camera image

It is well known that a camera image includes so-called line-integration effect. Assuming a laminar radial structure of constant density and temperature along the view line of the camera near the LCFS such as Fig.10, a pixel signal can be describe as Eq. 6.4.,

$$S_{pixel}(t) = \sum_{r \in dr} n_0(r,t) f(n_e(r,t), T_e(r,t)) A_{32} \quad (6.4)$$

where r is the radial position, n_0 is the density of neutrals, n_e is the electron density, T_e is the electron temperature. Assuming $n_0(r)$ is a constant in a short fluctuation time scale, and the fluctuation of T_e is much smaller than that of n_e , the fluctuation part of pixel signal is,

$$\tilde{S}_{pixel}(t) \approx \left(\sum_{r \in dr} \alpha(r) \tilde{n}_e(r,t) \right) \quad (6.5)$$

where the top symbol “ \sim ” means the fluctuation part of the variable or function, and α_0 is constant for the same ρ . This result is basically consistent with our intuition; that the fluctuation information of camera signal is the weighted summation of the density fluctuation on the line integration path.

When the probe is inserted to the camera viewing area, the interaction between plasma and the probe (probe tips and/or probe shaft) will significantly enhance the local emission (PSI-effect). In this case, Eq. 6.5 is rewritten into,

$$\tilde{S}_{pixel}(t) = \tilde{S}_{PSI}(t) + \sum_{r \in dr} \alpha(r) \tilde{n}_e(r,t) \quad (6.6)$$

where the $\tilde{S}_{PSI}(t)$ is the emission come from the PSI-effect. Note that in Eq. 6.6 the integration line path is reduced to dr' . In the case of intense interaction,

CHAPTER 6 Investigation of the edge turbulence combining a camera and a Langmuir probe cluster in Heliotron J

$$\tilde{S}_{PSI}(t) \gg \sum_{r \in dr} \alpha(r) \tilde{n}_e(r, t) \quad (6.7)$$

we get,

$$\tilde{S}_{pixel}(t) \approx \tilde{S}_{PSI}(t) \quad (6.8)$$

Supposing the probe tips / body will only interact with the nearby local plasma, when the local density fluctuates, the interaction emission will change as well,

$$\tilde{S}_{PSI}(t) \propto \tilde{n}_{e-local}(t) \quad (6.9)$$

where $\tilde{n}_{e-local}(t)$ is the local density fluctuation. Combining 6.8 and 6.9, we then get,

$$\tilde{S}_{pixel}(t) \propto \tilde{n}_{e-local}(t) \quad (6.10)$$

It is easy to check this since the local density fluctuation is measured by the ion saturation current signal,

$$\tilde{I}_s(t) \propto \tilde{n}_{e-local}(t) \quad (6.11)$$

If Eq. 6.10 is consistent with the reality, there will be high cross-correlation between $\tilde{S}_{pixel}(t)$ and $\tilde{I}_s(t)$.

Figure 11 shows the interaction level between plasma and the probe. Figures 10(a) and (b) show the time-averaged “background” image in the time span of 225-230ms at $\Delta r = 20$ mm and $\Delta r = 0$ mm, respectively. In Fig. 11(a), at the probe position of $\Delta r = 20$ mm (20 mm outside of the LCFS), the brightness around probe has little difference with that in far from the probe position, which means the interaction is not significant. In Fig. 11 (b), at the position of $\Delta r = 0$ mm (on the LCFS) the brightness around probe was much enhanced compared to that in the case of $\Delta r = 20$ mm. This suggests that as probe was inserted into deeper position, there was more significant interaction. This is consistent with the edge plasma profile. Figure 6 shows the profiles of time averaged ion saturation current $\langle I_s \rangle$ at 218ms and 227ms. At both of the two timings, the slopes of $\langle I_s \rangle$ are sharp inside $\Delta r = 15$ mm and become flat from $\Delta r = 20$ mm outward.

Figures 11 (c) and (d) show the “fluctuation level” image in the same time span of 225-230ms. Each pixel data of the image are the standard deviation of 10 kHz high-passed raw data normalized by the “background” in the time span. In Fig. 11 (c), at the probe position of $\Delta r = 20$ mm, the fluctuation level around the probe show little difference with that in far from the probe position. In Fig. 11 (d), at the position of $\Delta r = 0$ mm, the fluctuation level around the probe is significantly higher than that in the case of $\Delta r = 20$ mm and that in far from the probe position. Based on our physics model, the higher fluctuation level is because the local fluctuation near the probe head was “emphasized” by the interaction.

Before the combination analysis, we have to check the difference of the start trigger timing of the data acquisition system for the camera and the probe. This time difference is because that we are using different trigger system for camera and probe. Analysis approach of

CHAPTER 6 Investigation of the edge turbulence combining a camera and a Langmuir probe cluster in Heliotron J

the cross-correlation between $\tilde{S}_{pixel}(t)$ and $\tilde{I}_s(t)$ is illustrated in Fig. 12. Figure 12(a) is an example of the cross-correlation in the time domain between the 5 kHz high-pass-filtered camera data and I_{s1} in a time span of 2ms. Here, the camera data are come from the pixel denoted by “+” in Fig. 3. The time delay Δt at the maximum cross-correlation shown in Fig. 8(a) suggests there is difference of $\square t$ between the start timing of camera and probe data. Although the value of this time difference Δt is scattered among discharges due to time jitter in each trigger system, it keeps the same value during one discharge, as shown in Fig. 12 (d), where the time trace of maximum value of the cross-correlation is also shown.

Figures 12(b) and (c) show the high-passed data of camera and I_s , respectively. The purple dash line labeled the timing of SMBI. Although the details of fluctuation characteristics during SMBI plasma will be discussed elsewhere, high cross-correlation of 0.6-0.8 is observed between these two signals in this discharge, indicating that the fluctuation information of the camera signal is mainly from the local density fluctuation. Figure 13 shows the maximum cross-correlation in the space of Δr and time. The cross-correlation is high (up to 0.6-0.8) for $\Delta r \leq 15$ mm, and low outside of $\Delta r \geq 20$ mm, suggesting the interaction became intense from $\Delta r=15$ mm thus the local density fluctuation emphasized in camera data.

In this section, we found that the camera data around the probe head is dominated by the PSI-effect. High cross-correlation was found between the fluctuation components of ion saturation current and the camera pixel signal nearby the probe tips. This demonstrates the fluctuation information from the intensity of plasma-surface interaction mainly reflects the local density fluctuation.

CHAPTER 6 Investigation of the edge turbulence combining a camera and a Langmuir probe cluster in Heliotron J

References

- [1] S. J. Zweben and D. P. Stotler *et al.*, *Phys. Plasmas*, **9**, 1981 (2002).
- [2] D. P. Stotler *et al.*, *Journal of Nuclear Materials*, **313-316**, 1066-1070 (2003).
- [3] S. J. Zweben *et al.*, *Nucl. Fusion*, **44**, 134 (2004).
- [4] Lipschultz *et al.*, *J. Vac. Sci. Technol. A*, **4** (3), 1810, (1986).
- [5] F. Sano *et al.*, *J. Plasma Fusion Res. Ser.*, **3** (2000) 26.
- [6] T. Obiki *et al.*, *Nucl. Fusion* **41**, 833 (2001).
- [7] T. Mizuuchi *et al.*, *J. Plasma Fusion Res. Ser.*, **3**, 192-196 (2000)
- [8] T. Mizuuchi *et al.*, *Journal of Nuclear Materials*, **337-339** (2005) 332-336.
- [9] T. Mizuuchi *et al.*, *Journal of Nuclear Materials*, **390-391** (2009) 428-431.
- [10] N. Nishino *et al.*, *Journal of Nuclear Materials*, **337-339** (2005) 1073.
- [11] N. Nishino *et al.*, *Journal of Nuclear Materials*, **363-365** (2007) 628.
- [12] N. Nishino *et al.*, *Journal of Nuclear Materials*, **390-391** (2009) 432.
- [13] N. Nishino *et al.*, *Journal of Nuclear Materials*, **415** (2011) S447.
- [14] L. ZANG *et al.*, *Plasma and Fusion Research*, **8**, 1402066 (2013).
- [15] N. Nishino *et al.*, *Journal of Nuclear Materials*, **438** (2013) S540-S544.
- [16] L. ZANG *et al.*, submitted to *Phys. Plasmas*.
- [17] D. E. Newland, *An Introduction to Random Vibrations, Spectral and Wavelet Analysis* (Longman Scientific & Technical, New York, 1993).

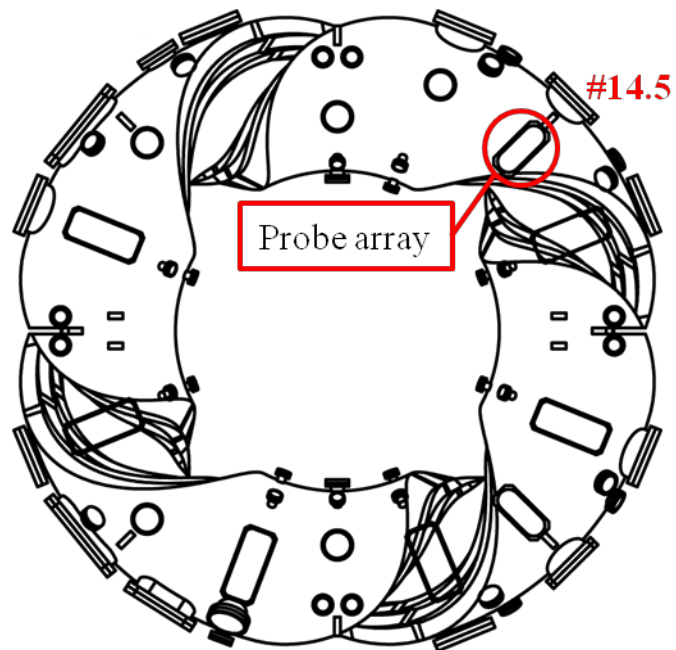
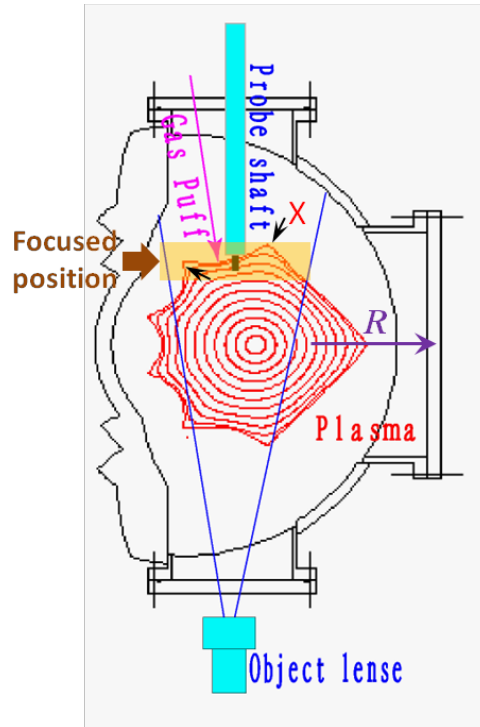
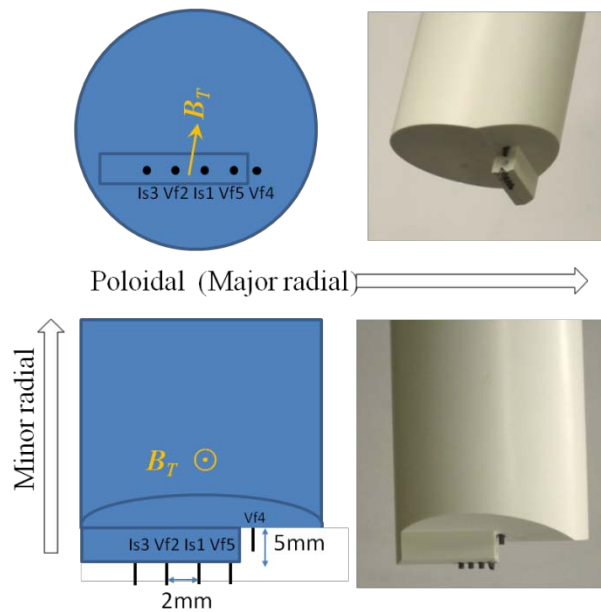


Fig.1 A schematic top-view of Heliotron J. The probe cluster is installed at the top port at #14.5.



(a)



(b)

Fig.2 (a) #14.5 poloidal cross section: “X” is the X-point of this magnetic configuration in vacuum condition. “R” is the major radial direction of torus. B_T is the magnetic field direction; (b) Structure of the Langmuir probe array: I_s is the ion saturation current signal. V_f is the floating potential. At the top of the cross section, the major radial direction also is the poloidal (azimuthal) direction.

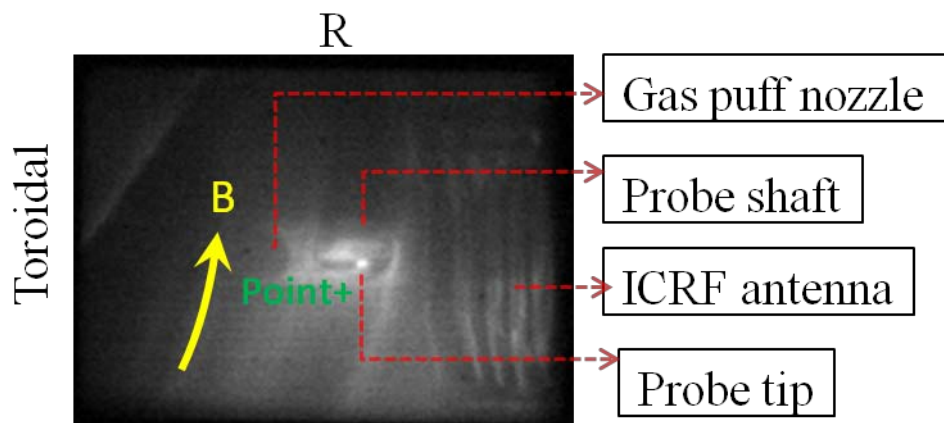


Fig. 3 A typical raw image of the camera video. The circle shape of the probe shaft and the bright point of one of the probe tips are clear observed. The green “+” point near the tips was selected for the following analysis.

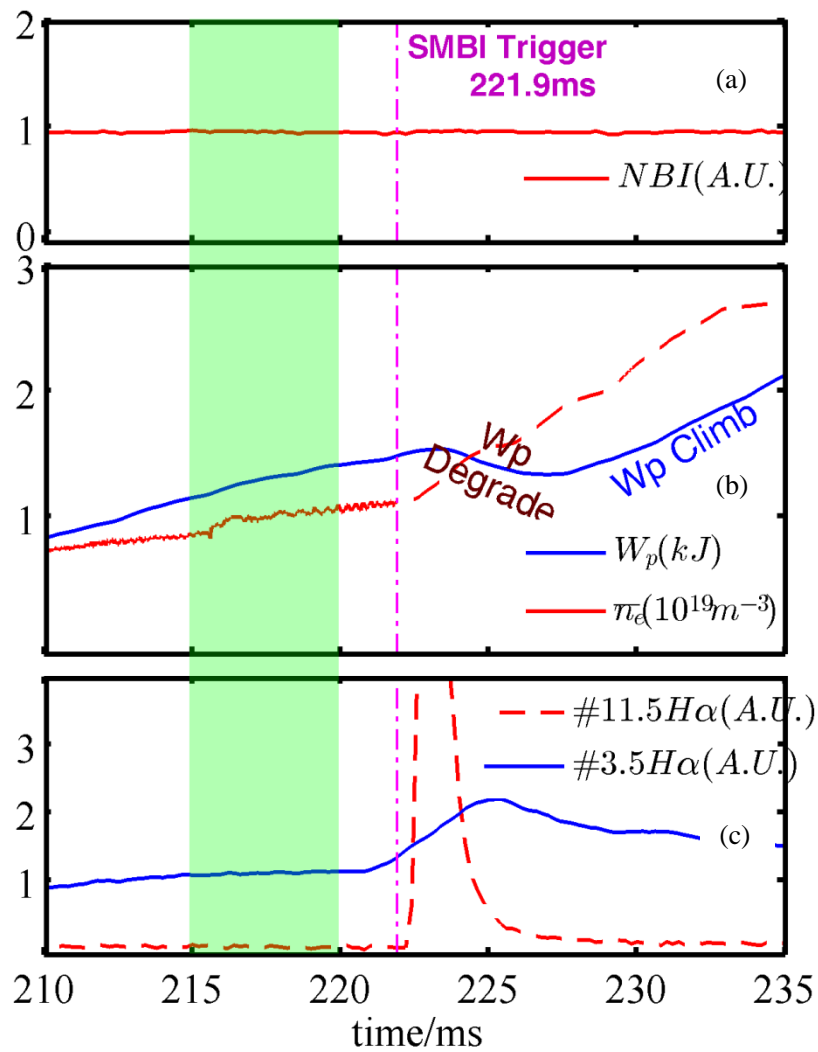


Fig. 4 Main plasma parameters: (a) NBI is the timing signal of Neutral Beam heating. (b) \bar{n}_e is the line-averaged electron density; W_p is the plasma stored energy measured with a diamagnetic loop; (c) #11.5 H α and #3.5 H α are the signal of H α ray detector at #11.5 and #3.5 sections, respectively. A Purple line indicates the timing of SMBI injection timing; A time span labeled by pink shadow is the period “just after SMBI” where W_p was degrading; The blue shadow labels the period long after SMBI when W_p was climbing.

CHAPTER 6 Investigation of the edge turbulence combining a camera and a Langmuir probe cluster in Heliotron J

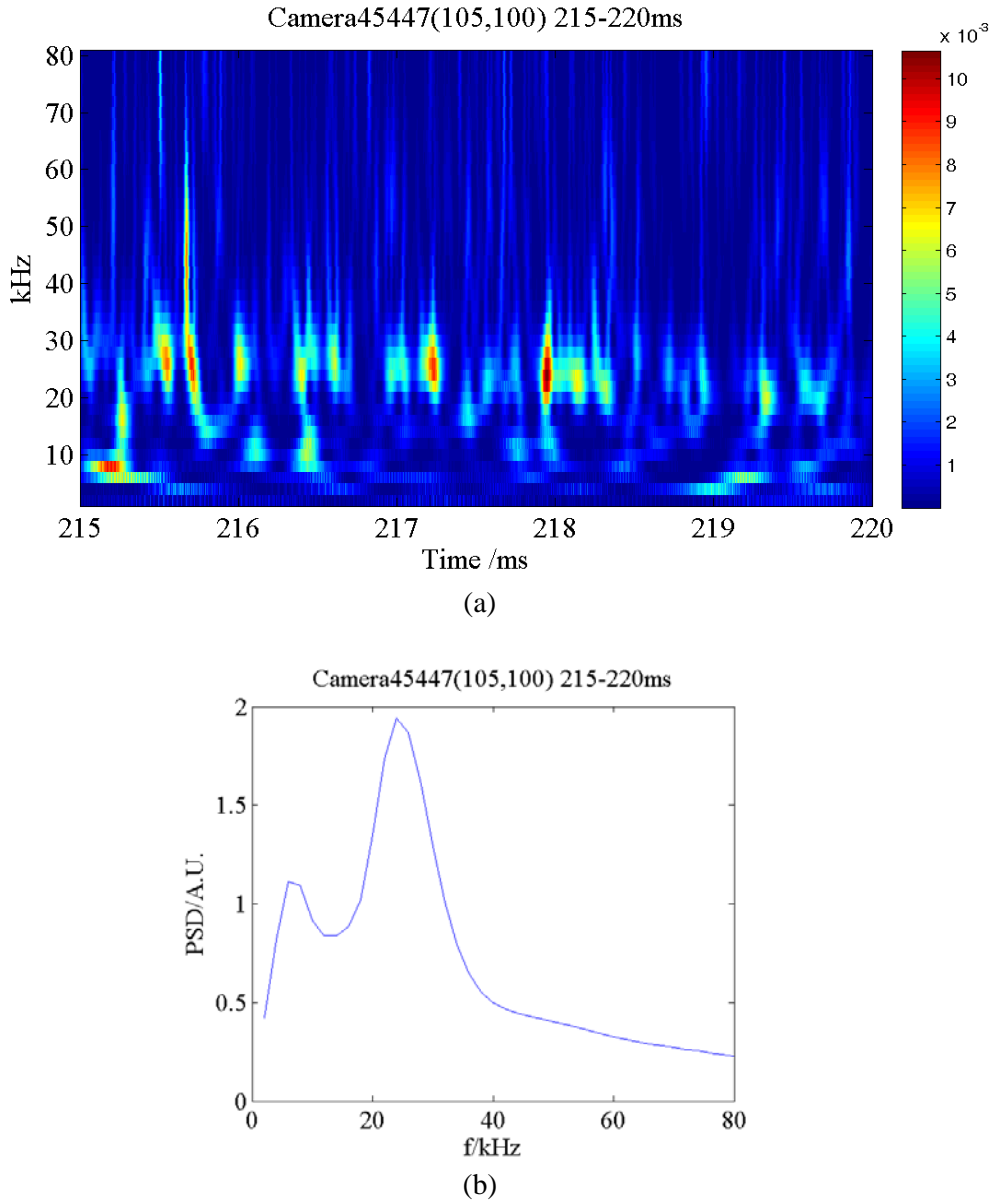


Fig. 5 (a) Wavelet power spectrogram of camera pixel data. (b) Wavelet power spectra density of camera pixel data. In this discharge, the probe tips is located at $\Delta r=20\text{mm}$.

CHAPTER 6 Investigation of the edge turbulence combining a camera and a Langmuir probe cluster in Heliotron J

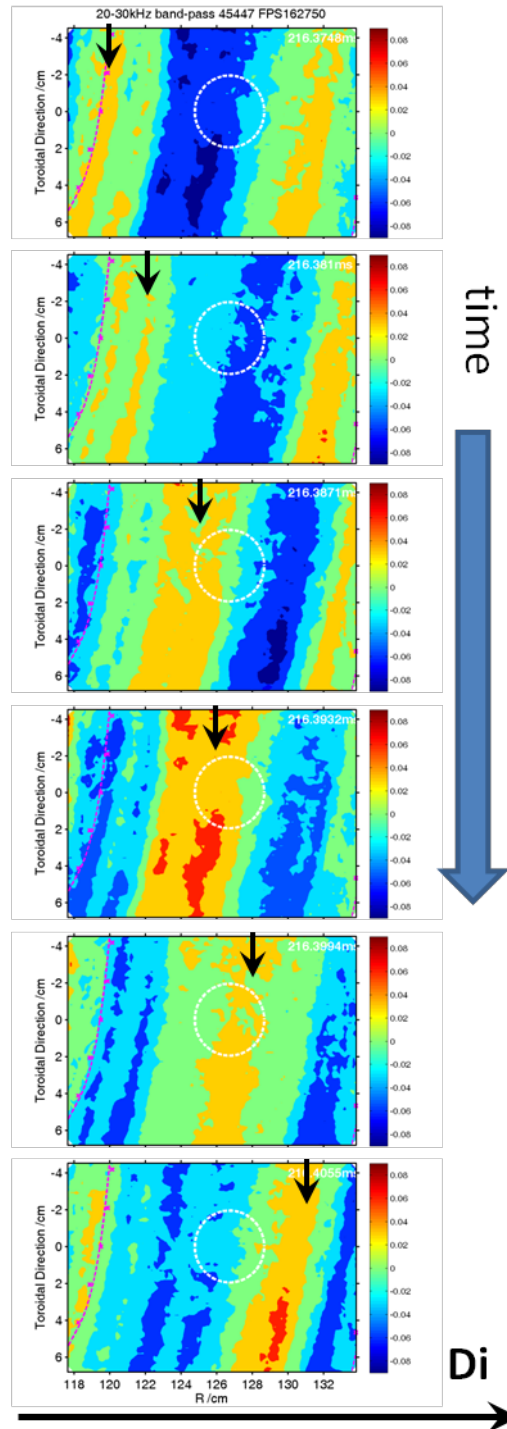


Fig. 6 Continuous frames of normalized 20-30 kHz band-passed fluctuation image with the probe located at $\Delta r=20\text{mm}$.

CHAPTER 6 Investigation of the edge turbulence combining a camera and a Langmuir probe cluster in Heliotron J

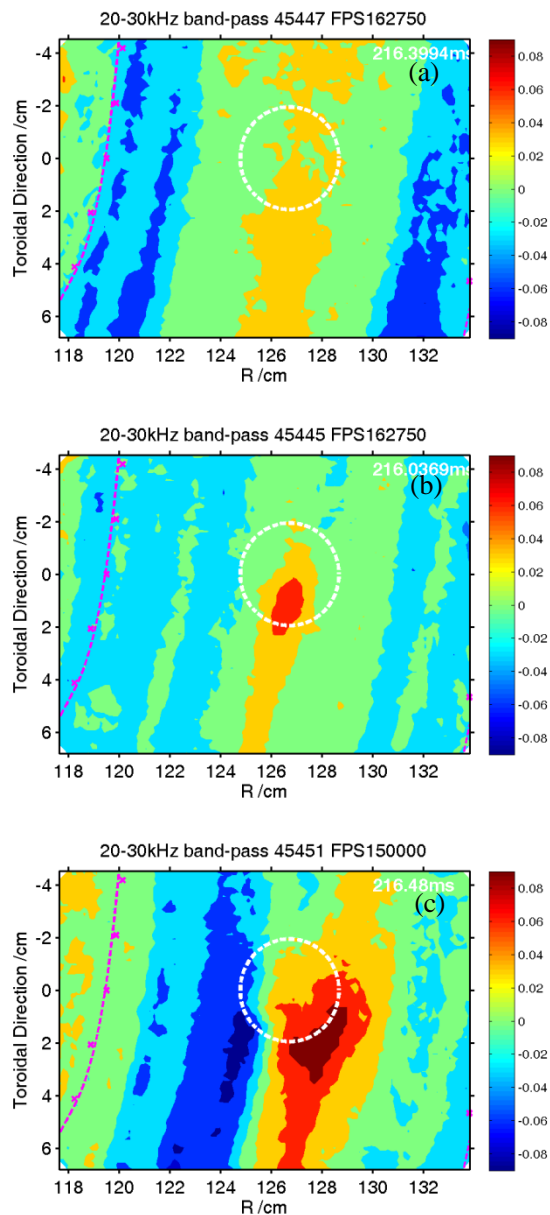


Fig. 7 Typical frames of normalized 20-30 kHz band-passed fluctuation image with the probe located at (a) $\Delta r=20\text{mm}$, (a) $\Delta r=10\text{mm}$, (a) $\Delta r=0\text{mm}$.

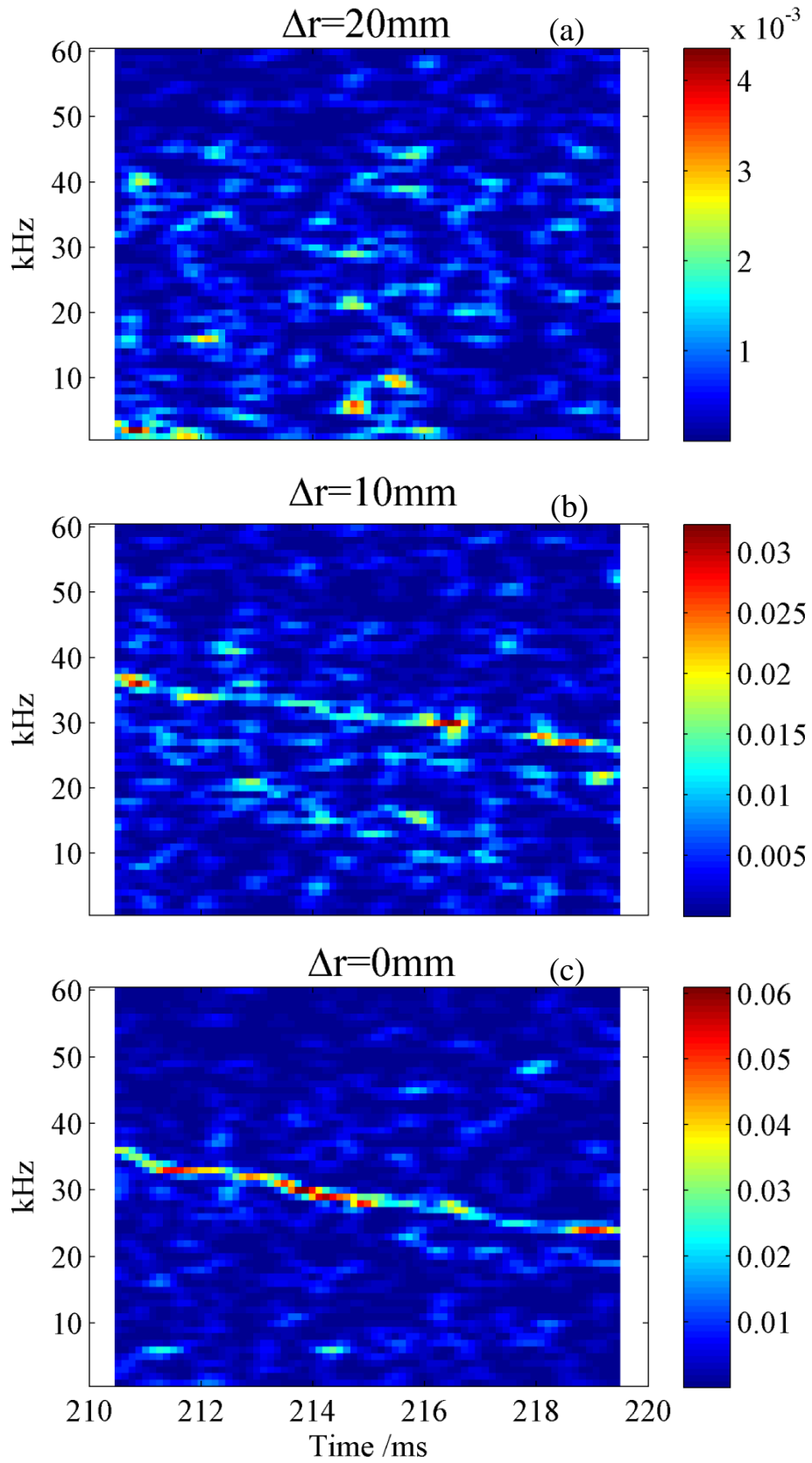


Fig. 8 Power spectrogram of Is1 at (a) $\Delta r = 20\text{mm}$, (b) $\Delta r = 10\text{mm}$, (c) $\Delta r = 0\text{mm}$.

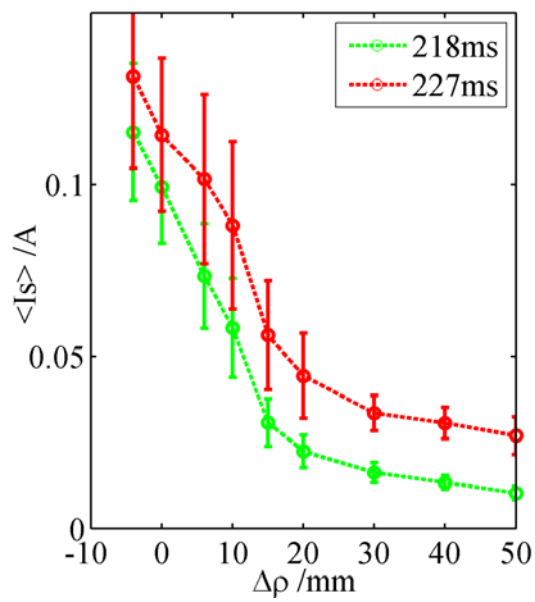


Fig. 9 Profile of time averaged ion saturation current $\langle I_s \rangle$ at 218ms and 227ms. The error bars show the standard deviation in 2ms window.

CHAPTER 6 Investigation of the edge turbulence combining a camera and a Langmuir probe cluster in Heliotron J

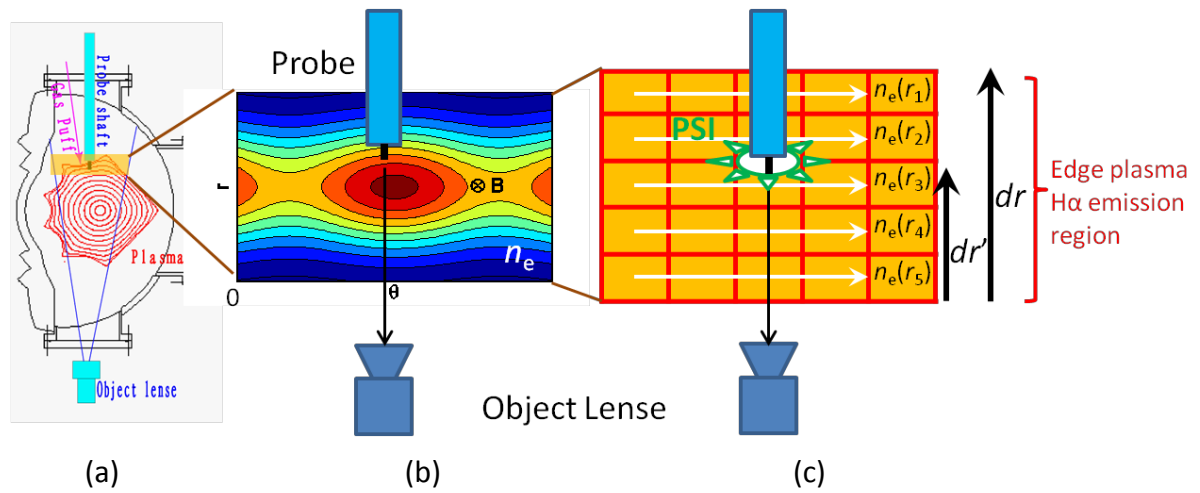


Fig. 10 (a) #14.5 cross section and the camera view. Yellow rectangle is the expected imaging region. (b) Zoomed-out picture of the imaged region. The contour shows assumed density structure of plasma turbulence. The arrow line is an imagined integration line of the camera signal. (c) The discretized picture of (b). Imagined PSI region is labeled with the green mark. Plasma parameters are assumed uniform along the same radial layer. Before probe inserted, the line-integration span is dr ; after probe inserted, the line-integration span is dr' .

CHAPTER 6 Investigation of the edge turbulence combining a camera and a Langmuir probe cluster in Heliotron J

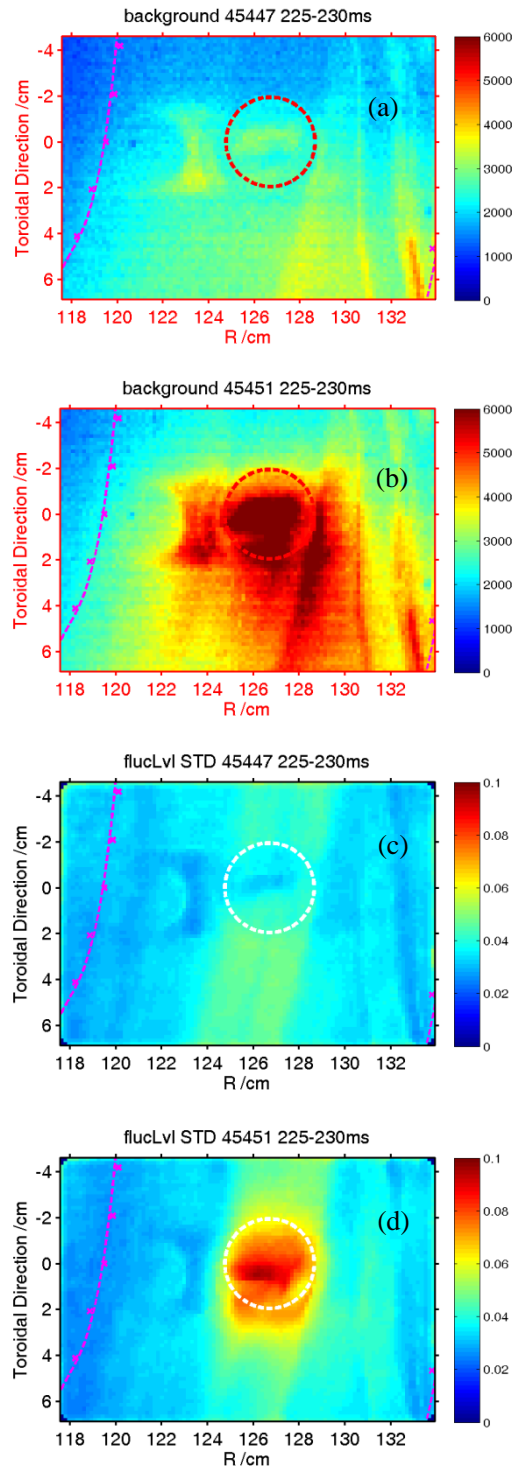


Fig. 11 Time averaged “background” for probe position (a) $\Delta r=20\text{mm}$ (b) $\Delta r=0\text{mm}$ during 225-230ms;

Standard deviation of 10 kHz high-passed raw data normalized by the “background” for probe position (c) $\Delta r=20\text{mm}$ (d) $\Delta r=0\text{mm}$ during 225-230ms. The purple dash line is the X-point. The dash circle in the center is the probe body. The vertical and horizontal axis are the toroidal and major radial (or poloidal) direction, respectively.

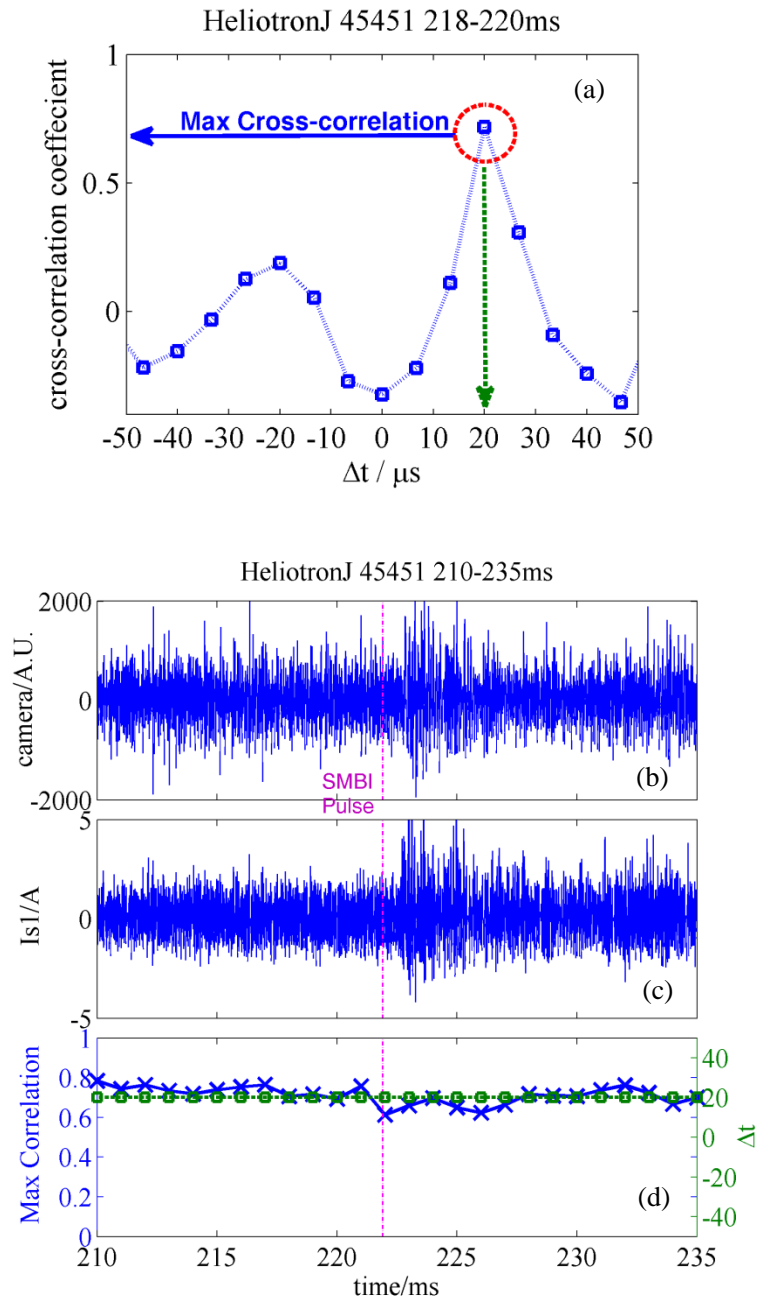


Fig. 12 The cross-correlation between the 5k Hz high-passed data of camera and Is data in a time span of 2ms. (a) The time delay Δt at the peak of cross-correlation suggests there is difference between the start timing of camera and probe data. (b) 5k Hz high-passed data of camera pixel data; (c) 5k Hz high-passed data of Is; (d) The trace of maximum cross-correlation. The purple dash line labeled the injection timing of SMB.

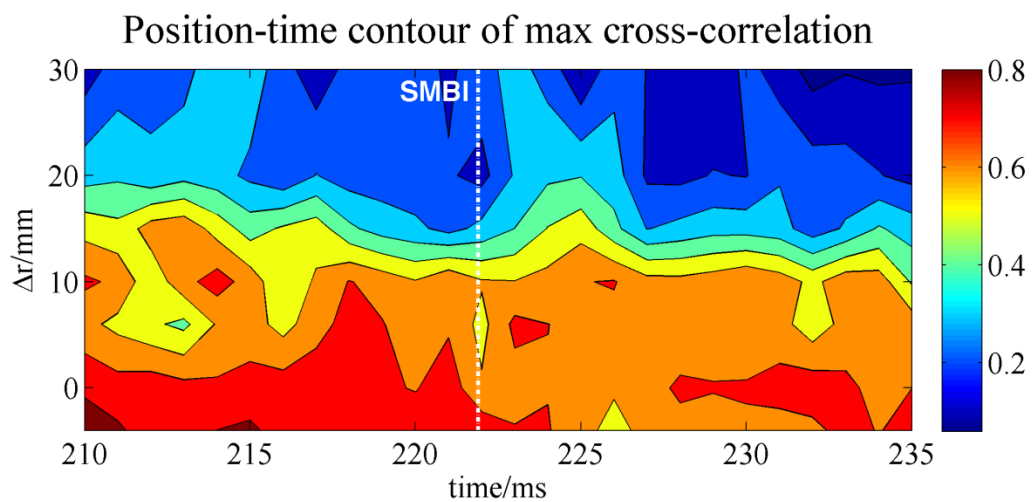


Fig.13 Δr versus time contour of the maximum cross-correlation.

Chapter 7. Summary

Summary of the main stories in this thesis are as follows:

- (1) Edge fluctuation in an SMBI fueled plasma has been measured using an electrostatic probe array. The local plasma fluctuation and fluctuation induced particle transport before and after SMBI have been analyzed. It is found, ① In a short duration (~4ms) just after SMBI, the low frequency broad-band density fluctuation increased, and the PDF changed from a nearly Gaussian to a positively skewed non-Gaussian one. This suggests intermittent structures were produced due to SMBI. Also the fluctuation induced particle transport was greatly enhanced during this short duration. ② After the duration in ①, the low frequency broad-band density fluctuation decreased, and the PDF returned to a nearly Gaussian shape. Also the fluctuation induced particle transport was reduced. On the other hand, the $E_r \times B$ flow shear was dramatically decreased just after SMBI, and increased after a short duration. This is possibly responsible for the change in the low frequency density fluctuation and fluctuation induced transport. Compared with normal gas puff, W_p degradation window is very short due to the short injection period of SMBI. After this short window, fluctuation induced particle transport was reduced and W_p started the climbing phase. This means the short effect period of gas injection to the edge fluctuation might be an advantage of this novel fueling technique.
- (2) In Heliotron J, the data processing technique has been developed to extract the filamentary structures of edge plasma density fluctuation using a perpendicularly-viewed high-speed video camera. In SMBI experiment, filamentary structures along the magnetic field line were observed just after SMBI, and their dynamics were revealed in consecutive images. Reverse of the filament motion is considered due to the line integration effect of imaging and the gas penetration over the flow shear layer.
- (3) To overcome the line-integration effect of camera, an electrostatic probe has been combined to get the radial span of the density fluctuation structures observed in camera video. With this technique, we have inferred that the outmost edge of a 20-30kHz density mode is at about 10mm outside of LCFS. This suggests the combination of camera and Langmuir probe is a powerful tool for edge fluctuation study.

Acknowledgements

Professor Tohru MIZUUCHI (水内亨) is my supervisor during the PhD course. I appreciate him for the encouragement and insightful guide.

I am grateful to Associate Professor Nobuhiro NISHINO (西野信博) (Hiroshima University). He has supported me for the development of fast camera system and the data analysis technique.

I am obliged to Assistant Professor Shinsuke OHSHIMA (大島慎介). He has designed and installed the Hybrid probe cluster and supported me for the installation of fast camera system. In particular, he has given a lot of helpful advices on the data analysis approach and physics discussion. Without his great supports, I could not finish the thesis.

I wish to thank Professor Fumimichi Sano (佐野史道). He gave me a chance to carry out this study and a lot of advices and supports for this study.

I appreciate Professor Kazunobu NAGASAKI (長崎百伸) for introducing me to Heliotron J group and the useful discussions on my research.

I wish to acknowledge Professor Yong LIU (刘永) (Southwestern Institute of Physics - SWIP), Professor Xuru DUAN (段旭如) (SWIP), Professor Qingwei YANG (杨青巍) (SWIP), Professor Longwen YAN (严龙文) (SWIP), and Professor Yi LIU (刘仪) (SWIP) for the information and recommendation of my oversea study.

I express my special appreciation to four of the students in the Graduate School of Energy Science, Kyoto University: Dr. Kiyofumi MUKAI (向井清史), Dr. Hyunyong LEE (李炫庸), Mr. Naoki KENMOCHI (剣持尚輝), Mr. Keijun KASAJIMA (笠嶋慶純). They have provided me great help in my life in Japan and I have greatly enjoyed the campus life in Kyoto University with them.

I am grateful to the fast camera and Langmuir probe group in Heliotron J for their great supports: Masaki TAKEUCHI (竹内正樹), Kohei HASHIMOTO (橋本紘平), Mengyu SHA (沙梦雨).

I wish to acknowledge the other scientists in Heliotron J group: Shinichiro KADO (門信一郎), Satoshi YAMAMOTO (山本聡), Hiroyuki OKADA (岡田浩之), Takashi MINAMI (南貴司), Shinji KOBAYASHI (小林進二), Nan SHI (史楠), Shigeru KONOSHIMA (木島滋), for plenty of supports and discussions on my research.

I would like to thank Professor Longwen YAN (□□文) (SWIP), Associate Professor Jiquan LI (李□全) (Kyoto University), Professor Yasuaki KISHIMOTO (岸本泰明) (Kyoto University), Dr. Deliang YU (余德良) (SWIP), and Dr. Jun CHENG (程均) (SWIP) for the great help in physics discussion and data analysis.

I am grateful to the Heliotron J technical and official staffs for their supports: Y. Ijiri, T. Senju, K. Yaguchi, K. Tohshi, K. Sakamoto, M. Shibano, K. Kumabe, H. Inui, S. Watanabe, H. Yokota.

I am grateful to the other students of the Graduate School of Energy Science, Kyoto University: K. Minami, T. Kagawa, S. Arai, H. Watada, Y. Wada, Y. Nagae, H. Fukushima, Y. Ohtani. I have enjoyed the campus life in Kyoto University with them.

My research work is partially supported by NIFS collaborative research program (NIF10KUHLLL030) and the Global Centers Of Excellence (GCOE) program in Kyoto University. The MEXT scholarship has supported me financially during PhD course.

Finally, I am very grateful to my parents Jianxiang LI (李建香) and Tingwu ZANG (臧廷武).

Lists of Publications and Presentations

• Publications

As the first author:

1. **ZANG Linge**, M. TAKEUCHI, N. NISHINO, T. MIZUUCHI, S. OHSHIMA, K. KASAJIMA, M. SHA, K. MUKAI, H. Y. LEE, K. NAGASAKI, H. OKADA, T. MINAMI, S. KOBAYASHI, S. YAMAMOTO, K. HANATANI, Y. NAKAMURA, S. KONOSHIMA, F. SANO. Observation of Edge Plasma Fluctuations with a Fast Camera in Heliotron J. Plasma Science and Technology, Vol.15, No.3, 213, Mar. 2013. (with review)
2. **Linge ZANG**, Nobuhiro NISHINO, Tohru MIZUUCHI, Shinsuke OHSHIMA, Masaki TAKEUCHI, Keijun KASAJIMA, Mengyu SHA, Kiyofumi MUKAI, Hyunyong LEE, Kazunobu NAGASAKI, Hiroyuki OKADA, Takashi MINAMI, Shinji KOBAYASHI, Satoshi YAMAMOTO, Shigeru KONOSHIMA, Yuji NAKAMURA and Fumimichi SANO. Observation of Edge Filamentary Structure Motion during Supersonic Molecular-Beam Injection Using a Fast Camera in Heliotron J. Plasma and Fusion Research. Vol.8, 1402066, 2013. (with review)
3. **Linge ZANG**, Shinsuke OHSHIMA, Tohru MIZUUCHI, Nobuhiro NISHINO, Keijun KASAJIMA, K. HASHIMOTO, Mengyu SHA, Masaki TAKEUCHI, Kiyofumi MUKAI, Hyunyong LEE, Naoki KENMOCHI, Kazunobu NAGASAKI, Shinichiro KADO, Hiroyuki OKADA, Takashi MINAMI, Shinji KOBAYASHI, Satoshi YAMAMOTO, Nan SHI, Shigeru KONOSHIMA, Yuji NAKAMURA, and Fumimichi SANO. Effect of SMBI on edge fluctuation and particle transport in Heliotron J. Submitted to Physics of Plasmas. (under review)
4. **Linge ZANG**, Tohru MIZUUCHI, Nobuhiro NISHINO, Shinsuke OHSHIMA, Keijun KASAJIMA, K. HASHIMOTO, Mengyu SHA, Masaki TAKEUCHI, Kiyofumi MUKAI, Hyunyong LEE, Naoki KENMOCHI, Kazunobu NAGASAKI, Shinichiro KADO, Hiroyuki OKADA, Takashi MINAMI, Shinji KOBAYASHI, Satoshi YAMAMOTO, Nan SHI, Shigeru KONOSHIMA, Yuji NAKAMURA, and Fumimichi SANO Investigation of the edge turbulence combining a camera and a Langmuir probe cluster in Heliotron J. Under revise in Helitron J group.

As one of the cooperated authors:

5. N. Nishino, **L. Zang**, M. Takeuchi, T. Mizuuchi, S. Ohshima, K. Kasajima, M. Sha, K. Mukai, H.Y. Lee, K. Nagasaki, H. Okada, T. Minami, S. Kobayashi, S. Yamamoto, S. Konoshima, Y. Nakamura, F. Sano. Edge turbulence measurement in Heliotron J using a combination of hybrid probe system and fast cameras. Journal of Nuclear Materials. Vol.

438, S540–S544, 2013.

6. T. Mizuuchi, H.Y. Lee, K. Mukai, K. Yamamoto, S. Kobayashi, H. Okada, S. Yamamoto, S. Ohshima, **L. Zang**, K. Nagasaki, T. Minami, T. Kagawa, T.Y. Minami, K. Mizuno, Y. Wada, S. Arai, H. Yashiro, H. Watada, K. Hashimoto, N. Kenmochi, Y. Nagae, M. Sha, Y.I. Nakamura, K. Kasajima, N. Nishino, K. Hosoi, Y. Nakashima, Y. Nakamura, S. Konoshima, F. Sano. A Gas fueling effect on plasma profile in Heliotron J. Journal of Nuclear Materials 438 (2013) S453–S458.
7. S. Ohshima, K. Hashimoto, S. Kobayashi, S. Yamamoto, K. Nagasaki, T. Mizuuchi, H. Okada, T. Minami, S. Konoshima, H.Y. Lee, **L. Zang**, K. Kasajima, Y. Nagae, K. Mukai, H. Matsuura, M. Takeuchi and F. Sano. Edge Plasma Response to Beam-driven MHD Instability in Heliotron J. EX/P4-17, 24th IAEA Fusion Energy Conference, 2012.
8. N. Shi, S. Ohshima, K. Tanaka, T. Minami, K. Nagasaki, S. Yamamoto, Y. Ohtani, **L. Zang**, T. Mizuuchi, H. Okada, S. Kado, S. Kobayashi, S. Konoshima, N. Kenmochi, and F. Sano. A novel electron density reconstruction method for asymmetrical toroidal plasmas. To be submitted to Review of Scientific Instruments.

• Presentations

1. L. Zang, M. Takeuchi, N. Nishino, T. Mizuuchi, S. Ohshima, K. Kasajima, M. Sha, K. Mukai, H.Y. Lee, K. Nagasaki, H. Okada, T. Minami, S. Kobayashi, S. Yamamoto, K. Hanatani, Y. Nakamura, S. Konoshima, F. Sano. Observation of edge plasma fluctuations with a fast camera in Heliotron J. *8th General Scientific Assembly of the Asia Plasma and Fusion Association, Guilin, China*. 2011/11.
2. L. Zang, M. Takeuchi, N. Nishino, T. Mizuuchi, S. Ohshima, K. Kasajima, M. Sha, K. Mukai, H.Y. Lee, K. Nagasaki, H. Okada, T. Minami, S. Kobayashi, S. Yamamoto, S. Konoshima, K. Hanatani, Y. Nakamura, F. Sano. Study of filament features of edge plasma fluctuations using fast video cameras with a combination of Langmuir probe measurements in Heliotron J (I). *Plasma Conference 2011, Kanazawa, Japan, 2011/11/23*, 23P038-P
3. L. Zang, N. Nishino, T. Mizuuchi, S. Ohshima, K. Kasajima, M. Sha, K. Mukai, H. Lee, K. Nagasaki, H. Okada, T. Minami, S. Kobayashi, S. Yamamoto, S. Konoshima, K. Hanatani, Y. Nakamura, F. Sano. Study of filament features of edge plasma fluctuations in Heliotron J. *18th International Stellarator/Heliotron Workshop 2012, Canberra, Australia, 2012/2/2*,
4. ZANG Linge, S. Ohshima, N. Nishino, T. Mizuuchi, M. Takeuchi, K. Kasajima, M. Sha, K. Mukai, H. Y. Lee, K. Nagasaki, H. Okada, T. Minami, S. Kobayashi, S. Yamamoto, S. Konoshima, K. Hanatani, Y. Nakamura, F. Sano. Statistical properties of intermittent

transport across LCFS in Heliotron J. *9th joint workshop of fusion energy*, 2012.6.28-29, 29A-32p

5. Linge ZANG, Nobuhiro NISHINO, Tohru MIZUUCHI, Shinsuke OHSHIMA, Masaki TAKEUCHI, Keijun KASAJIMA, Mengyu SHA, Kiyofumi MUKAI, Hyunyong LEE, Kazunobu NAGASAKI, Hiroyuki OKADA, Takashi MINAMI, Shinji KOBAYASHI, Satoshi YAMAMOTO, Shigeru KONOSHIMA, Yuji NAKAMURA, Fumimichi SANO. Synchronous observation of filament properties using a fast camera and a hybrid probe in Heliotron J. *54th Annual Meeting of the APS Division of Plasma Physics* Rhode Island Convention Center, Providence, Rhode Island, USA October 29 - November 2, 2012 TP8. 00041.
 6. Linge ZANG, Nobuhiro NISHINO, Tohru MIZUUCHI, Shinsuke OHSHIMA, Masaki TAKEUCHI, Keijun KASAJIMA, Mengyu SHA, Kiyofumi MUKAI, Hyunyong LEE, Kazunobu NAGASAKI, Hiroyuki OKADA, Takashi MINAMI, Shinji KOBAYASHI, Satoshi YAMAMOTO, Shigeru KONOSHIMA, Yuji NAKAMURA, Fumimichi SANO. Study of Filament Features of Edge Plasma Fluctuations using Fast Camera and Langmuir Probe Measurements in Heliotron J. *22nd International Toki Conference* Ceratopia Toki, Toki-city, Gifu, JAPAN November 19-22, 2012 P3-44.
-